High harmonic driven attosecond and femtosecond molecular dynamics

by

Craig Hogle

B.A., Carleton College, 2007

M.S., University of Colorado, 2011

A thesis submitted to the

Faculty of the Graduate School of the

University of Colorado in partial fulfillment

of the requirements for the degree of

Doctor of Philosophy

Department of Physics

2014

This thesis entitled:
High harmonic driven attosecond and femtosecond molecular dynamics
written by Craig Hogle
has been approved for the Department of Physics

Margaret M. Murnane

Henry C. Kapteyn

Date _____

The final copy of this thesis has been examined by the signatories, and we find that both the content and the form meet acceptable presentation standards of scholarly work in the above mentioned discipline.

Hogle, Craig (Ph.D., Physics)

High harmonic driven attosecond and femtosecond molecular dynamics

Thesis directed by Prof. Margaret M. Murnane

To fully understand atomic and molecular dynamics scientists must be able to probe and study dynamics on their fundamental time scales. The motion, structure, and arrangement of molecules play a fundamental role in chemical reactions. Analyzing these reactions is not only important for their immediate insights, but the understanding is essential for the progress of many areas of science and technology including biology, material science, and medicine.

These dynamics require a light source with the time resolution to capture attosecond and femtosecond dynamics and access a large energy range of interesting processes. High harmonic generation (HHG) provides a tunable coherent light source of high energy photons while remaining table-top in size. These highly excited states can be investigated using coincidence electron and ion spectroscopy with short time scale resolution.

The combination of high harmonic generation with coincidence spectroscopy allows for the study of a variety of atomic and molecular systems. We were able to observe a new ionization pathway enabled by intense laser fields in argon and xenon. With helium, we demonstrate the ability to optically induce full electromagnetic transparency. The time resolved dissociation of bromine allowed for the understanding of how molecular orbital structure changes to become atomic in nature. In hydrogen we considered the interaction of electronic and nuclear wavepackets in a non-Born-Oppenheimer regime in a new level of detail. We explore the coherent control in dissociating a triatomic molecule with N_2O allowing for the ability to optically control the dissociation pathway of the molecule. Additional molecules including the argon dimer, ethylene and ozone have also been studied and analysis points to very interesting dynamics.

Dedication

To Ethan Townsend and Jing Yin.

Acknowledgements

I would like to thank my advisors Margaret Murnane and Henry Kapteyn for the many opportunities they presented me.

I would like to thank my parents and family for being an incredible support for me. This would not have been possible with you and your never-ending encouragement.

Thanks to William Peters, Predrag Ranitovic, Wen Li, and Vandana Sharma for the help running experiments and analysis. This would not have been possible without their guidance and teaching. Thanks to Xiao-Min Tong, Agnieszka Jaroń-Becker, and Fernando Martín and many others for their incredible theoretical support.

I would have been completely lost without Philip Makotyn. He was there when I needed him the most. Many thanks to Will, Jen, Ben, Tory, Ariel, and Betsy and many others for helpful conversations, and reminding me what is important.

Thanks to Vincent Crowder who traveled most of this journey with me.

Many thanks to my coworkers for help along the way especially to all within the K-M group. Many thanks also to the JILA machining, electronic, and computing support and to the all the staff helping with no expectation of recognition. To Daisy Raymondson for her friendship and sharing her expertise with the amplifier. And thanks to the many at KM Labs for their continued technical support.

To Melina, Ross, Kassie and John, thanks for getting me past Olin and continuing to be in my life.

For everyone that I have danced with over the last seven years, you provided many incredible

experiences and support when you didn't know I needed it.

I would like to thank Ken for being such a good friend and for helping me keep my sanity and most of all keeping me responsible. Thank you to Ross for his support and always encouraging me to stay focused.

Contents

Chapter

Figures

Figure

Chapter 1

Introduction

To fully understand atomic and molecular dynamics scientists must be able to probe and study those dynamics on their fundamental time scales. In molecules, these dynamics span from attosecond time scales characteristic of electronic dynamics, to femtosecond time scales characteristic of vibrations and dissociations, to picosecond time scales characteristic of rotations. The motion, structure, and arrangement of molecules play a fundamental role in chemical reactions. Analyzing these reactions is not only important for their immediate insights but the understanding is essential for the progress of many areas of science and technology including biology, material science, and medicine.

With the development of the laser over 50 years ago, scientists gained a crucial tool for studying atomic and molecular processes. Shortly thereafter, the use of nonlinear processes provided a coherent source of high energy photons. With the advent of femtosecond lasers, observing the transition states in a chemical reaction [1], and controlling the reaction itself, became feasible. Recent advances allow the production of coherent photons spanning well past the ultraviolet portion of the spectrum into the soft x-rays with the tremendous potential for pushing towards even higher energies.

Molecular dynamics call for a light source with not only the time resolution to capture attosecond and femtosecond dynamics but also can select between dissociating pathways, single and double ionization, and other highly excited electronic states. This energy range includes super-excited shake-up and shake-off states that involve electron-electron correlations and complex electron-nuclei

interactions that are not well understood. Even the lowest driven dynamics call for photons of several eV and the most exotic states require higher energies of tens of eV. Visible spectrum photons are suited for studying valence electron dynamics, but will ionize outer electrons before probing the states of inner valence or core level excitations. Only with shorter wavelength photons can one probe these dynamics directly. Involving the inner electrons allows for the study of multi-electron processes. The coherent manipulation of chemical systems on their natural time scales, as a means to control the evolution of a reaction, is a pivotal goal.

The combination of ultrashort pulsed lasers and high harmonic generation (HHG) provides for a coherent photon source that spans from the deep ultra-violet all the way to soft x-rays [2]. Here, we will focus on the extreme ultraviolet (XUV) portion of the spectrum as a probe of these dynamics. The emission of harmonics as a pulse train maintains the ability to keep the time resolution necessary to capture these dynamics due to time-bandwidth limits set by the uncertainty principle. High harmonic generation is also a tunable light source allowing the control to probe specific electronic states while being table-top in size. This allows real time experiments to be performed on a dedicated detector with a variety of targets that can be limited on large scale sources like synchrotrons and free electron lasers.

A sensitive detection technique is required to properly analyze the complex processes that are induced or probed with high harmonic generation. Often multiple reactions are caused by the range of frequencies used, so accurate filtering and statistical analysis is required. This not only requires the reliable generation of interesting dynamics but the ability to detect both the electronic as well as nuclear dynamics. One effective way to achieve this is to detect ions and electrons in coincidence. Cold target recoil ion momentum spectroscopy (COLTRIMS) is a powerful technique for coincidence detection and provides full momentum resolution [3–5]. This apparatus allows for 3D momentum to be captured in a geometry that allows for the collection of all trajectories. Both electrons and ions from each event can be slowed and redirected to sensitive detectors without loss of information. With the full momentum of each particle available, the nuclear and electronic states can be fully analyzed.

Chapter 2 provides a brief explanation of the experimental apparatus including the processes of the laser amplification, high harmonic generation, and ion and electron detection. Chapters 3 through 8 discuss specific experimental results. Chapters 3 and 4 deal with atomic systems, focusing on argon and helium, respectively. With argon, a new ionization pathway enabled by intense laser fields is explored, and with helium, the ability to induce full electromagnetic transparency is shown to be experimentally possible. Chapter 5 deals with the time resolved dissociation of bromine and the understanding of how molecular orbital structure changes as the dissociation process occurs. Chapter 6 examines the simplest molecule, hydrogen, in a new level of detail. It considers the interaction of electronic and nuclear wavepackets in a non-Born-Oppenheimer regime. Chapter 7 extends the analysis to coherent control in dissociating a triatomic molecule showing the ability to optically control the dissociation pathway of the molecule. Chapter 8 discusses brief results of the argon dimer, ethylene and ozone.

Chapter 2

Experimental Apparatus

This Chapter discusses the important concepts of the experimental apparatus including the Ti:sapphire amplifier system, high harmonic generation (HHG) and the experimental detector. HHG provides an important tool relevant to studies of atomic and molecular dynamics and presents a means of creating an extreme ultraviolet (XUV) pulse that allows for both attosecond scale resolution while maintaining the necessary control over the spectral resolution. There are more detailed explanations of the technical considerations [6] and scientific aspects [7–9] of HHG available in the literature. The behavior of molecules when irradiated by laser light has been a subject of interest in the scientific community for many years. Atomic and molecular spectroscopy allows for deeper fundamental understanding as well as the ability to coherently control molecular dynamics [10–15]. It is the combination of this light source with a detection scheme able to resolve these dynamics occurring at the characteristic time scales, from attoseconds and femtoseconds, which allows for acquisition of useful and worthwhile information about atomic and molecular dynamics. Cold target recoil ion mass spectrometry (COLTRIMS) allows for this resolution while providing both nuclear dynamics and electronic excited state information in coincidence.

This chapter covers the broad technical aspects of the molecular dynamics experimental setup. Specific changes to the apparatus will be discussed within each experimental chapter, however many of the fundamental concepts and techniques remain similar for each result.

2.1 Ti:sapphire Amplifier System

The large gain bandwidth of a Ti:sapphire crystal, spanning over 200 nm and centered around 800 nm, makes it useful for many ultrafast laser systems [16]. The first self mode-locked laser demonstrated the ability to use this large bandwidth to create pulses with femtosecond duration [17]. Many improvements have been made since the first Ti:sapphire amplifier systems were developed. To achieve the high pulse energies necessary to drive the nonlinear high harmonic generation process as well as probe using strong-field techniques, the ultrashort pulses from the oscillator pass through a three stage multipass chirped pulse amplifier. The additional stages are required in order to achieve a higher repetition rate than would be possible on a single stage system. Increasing repetition rate with coincidence detection allows for an increase in the number of events detected in real time. While many experiments benefit directly from increased photon flux, for coincidence detection only one event can be recorded per laser shot. Therefore, the signal-to-noise is primarily limited by the number of total events that can be recorded.

2.1.1 Amplfication

Chirped pulse amplification (CPA) allows for amplification to high intensity without the risk of damaging the gain medium or other amplification optics [18–21]. Stretching the pulse duration by several orders of magnitude the intensity of the pulse can be safely increased while remaining below damage threshold. The pulse is then recompressed, undoing the added chirp.

Gain inside the amplifier is given by:

$$ln\, G + \frac{\bar{g}(\nu) I_1}{I_s}(G-1) = \gamma_0(\nu) l_g \tag{2.1}$$

where G is the gain factor given by the ratio of the amplified intensity to the output intensity, $G = I_2/I_1$, I_s is the saturation intensity, $\bar{g}(\nu)$ is the normalized line shape factor, γ_0 is the small gain factor per unit length, and l_g is the length of the gain medium.

For a final output, I_2, much smaller than the saturation intensity, equation 2.1 behaves as

the simple amplification law:

$$\frac{I_2}{I_1} = G_0(\nu) = e^{\gamma_0(\nu) l_g} \tag{2.2}$$

where l_g is the length of the gain medium. For $I_1 \gg I_2$ the gain equation becomes

$$I_2 = I_1 + \left[\frac{\gamma_0(\nu) I_s}{\bar{g}(\nu)}\right] l_g \tag{2.3}$$

This region of linear gain that occurs when saturation is reached, minimizes the power fluctuations of the amplifier and must be reached in the first amplifier stage. When saturation is not achieved the power fluctuations make the amplifier too unstable to use. The latter stages allow for increasing the power that allows for high harmonic generation and strong-field ionization but these stages will only intensify power fluctuations from the first stage.

2.1.2 Laser Amplifier Geometry

The amplifier design is shown in Figure 2.1. It employs a multipass ring geometry and includes two additional double-pass amplifier stages, each with its own Ti:sapphire crystal and pump laser.

The oscillator shown in Figure 2.1 is a stable cavity aligned for mode-locked performance and for generation of the short pulses. A continuous-wave (CW) laser at 532 nm is focused into the Ti:sapphire crystal, where energy is stored through population inversion. The ultrashort pulses are generated by the oscillator through Kerr-lens mode-locking at approximately 80 MHz. The pulses then pass through a Pockels cell which selects the output repetition rate of 10 kHz. Each pulse is amplified with every additional pass through the following crystals. The filtering conditions allowed through COLTRIMS (as discussed in Section 2.3) make a higher repetition rate desirable to improve the statistics of the experiment. To achieve these conditions the laser must be aligned to its maximum efficiency while keeping a short pulse duration and good mode quality.

For the experiments discussed in Chapter 5, the amplifier was a simpler, single stage multipass

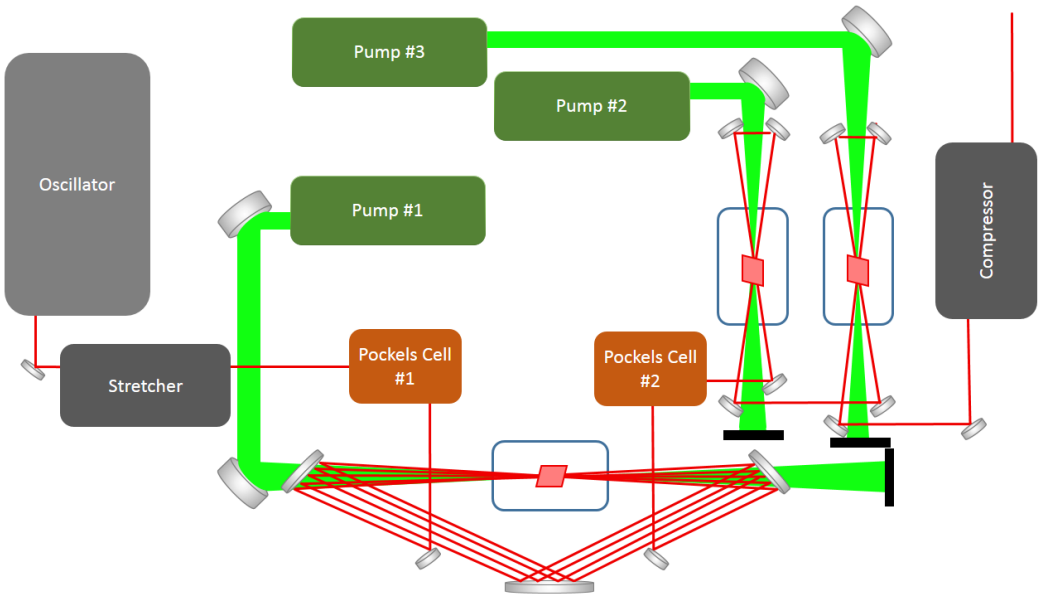

Figure 2.1: Schematic of the laser amplifier system. Short pulses (<30 fs) generated from an oscillator are stretched by several orders of magnitude after passing through a stretcher. A repetition rate of 10 kHz is selected by the first Pockels cell and then amplified by 14 passes through the first stage crystal. A second Pockels cell preserves the pulse contrast by suppressing any amplified spontaneous emission (ASE) from the first stage that would later be amplified in the latter stages. The pulse is additionally amplified by two passes each through the 2nd and 3rd stages. The pulse in then shortened to close to the original duration by passing through the compressor.

system with an output of ∼1.8 mJ, 30 fs pulse duration, with a repetition rate of 2 kHz and a beam profile M^2 measurement of 1.5. An entire new oscillator and amplifier were built to replace this, and were used for all remaining experiments. Additional details of the newer design can be found in [22]. Adding two additional amplifier stages and pump lasers allowed for an output of ∼3 mJ, 30 fs pulse duration, with a repetition rate of 10 kHz and a beam profile M^2 consistently below 1.3. The new amplifier design included the addition of a compressed helium cryorefrigerator (from Cryomech, Inc.). The additional cooling allowed for the use of necessary pumping powers for the higher repetition rate while maintaining a temperature range with increased thermal conductivity and avoiding the introduction of thermal lensing effects. Improvements were added periodically, allowing for additional power and pointing stability and thermal control due to changes in the crystal mounting geometry as well as two oscillator redesigns. To maintain a consistent output

energy, the original DM-100 532 nm pump lasers (from Photonics Industries) were replaced by a 100W Patara-HP (from Northrop Grumman Cutting Edge Optronics) and later by a 150W LDP-300MPQ (from Lee Laser).

Included in the change from one to the three stage amplifier were designs to make the system more compatible for carrier envelope phase stabilization. Included in these designs were copper 'foils' designed to decouple vibrations from the cryogenic cooling to the Ti:sapphire crystal mounts. These foils were designed with a large surface area that eventually proved to be too costly due to outgassing issues generated with the vacuum chambers for each amplifier crystal. These were replaced with solid copper mounts mounted directly to the cryogenic cooling, and proved to be an overall improvement.

2.2 High harmonic generation

High harmonic generation spanning from vacuum ultraviolet (VUV) spanning into the soft x-ray (SXR) region and approaching the hard x-ray portion of the electromagnetic spectrum [2] has become an important tool for various spectroscopic techniques [23–26]. Much of this has been made possible with the advancement of femtosecond duration lasers [27–29] as well as development in phase matching techniques [30,31]. When intense femtosecond laser pulses are focused into a gas, the nonlinear interaction between the strong electric field of the light pulse and the electrons of the atoms cause high harmonics of the driving laser frequency to be radiated. The high-energy photons generated from this process have been experimentally observed up to 1.6 keV and theoretically predicted to be able to extend to higher energies [2]. Each atom experiences the same coherent electric field resulting in the emission of high harmonic photons which are also coherent. This results in a coherent laser-like high harmonic beam to be emitted collinear with the fundamental light.

Additionally, high harmonic generation produces short bursts of photons with attosecond scale durations on each half cycle of the driving frequency due to each maximum intensity of the electric field. This time structure makes for a particularly useful tool for the study of atomic and

molecular dynamics in the time domain. To properly study many molecular dynamics, experiments require both spectral and temporal resolution, within the limitations of the uncertainty principle. An attosecond pulse train (APT) balances time and energy resolution while still spanning a broad spectrum, with each pulse having a relatively narrow bandwidth. This form of radiation is thus suited for initiating or probing atomic and molecular dynamics in real time, while also retaining spectroscopic selectivity [23, 32–34].

While it may seem preferential to excite dynamics with a single, short VUV or XUV attosecond pulse from a time domain perspective, a short pulse will have a broad bandwidth which will excite many ionization/dissociation channels with limited control or state selectivity. Probing for certain coherent electronic and nuclear quantum dynamics cannot be done with such a pulse. An isolated 200-attosecond pulse around 15 eV requires a bandwidth of ∼5 eV [23]. A pulse train from high harmonic generation produces a comb of odd harmonics in the frequency domain, with each harmonic having a full-width at half-maximum (FWHM) bandwidth typically a fraction of an eV. Additionally, such pulse trains can be tuned in the frequency domain (as discussed specifically in Chapters 3, 4 and 6) to coherently and selectively excite multiple electronic states. The mechanism responsible for this control is discussed in Section 2.2.2.

2.2.1 3-step model

High harmonic generation is the nonlinear interaction between an intense laser pulse and a medium that results in the generation of harmonics of the driving laser field. Whereas the generation of low-order harmonics can be solved theoretically, high harmonic generation cannot be described completely by perturbation theory. The characteristics of high harmonic generation often used to distinguish it are a sharp cutoff where the high-harmonics signal drops rapidly, a long plateau of harmonics with similar intensities and intense low-order harmonics, whose intensities do follow perturbation theory.

It is common to describe the regime in which ionization processes occurs by the Keldysh parameter, γ, which is defined as the ratio of the laser frequency to the tunneling frequency [35]:

$$\gamma = \sqrt{\frac{I_p}{2U_p}} \tag{2.4}$$

where I_p is the ionization potential of the atom, and U_p is the ponderomotive potential given by:

$$U_p = \frac{e^2 E_0^2}{(4m_e\omega_0^2)} \tag{2.5}$$

where e is the fundamental charge, E_0 is the electric field strength of the driving laser, m_e is the mass of the electron, and ω_0 is the laser angular frequency. The ponderomotive energy is the time-averaged kinetic energy gained by an electron in an electric field.

Figure 2.2 shows a typical plot of the dependence of the Keldysh parameter on the laser intensity and frequency for a given atomic Coulomb potential. When $\gamma \ll 1$, the ionization process and the laser frequency are fast, such that ionization occurs in the multiphoton regime. The laser intensity is small compared to the Coulomb potential, so that qualitatively the electronic wave packet remains trapped and localized by the potential until it can absorb enough photons for ionization. When $\gamma \leq 1$, ionization occurs in the tunneling regime and the laser frequency is slow such that the ionization can be approximated as quasistatic ionization occuring in the tunneling regime. The electric field significantly distorts the effective potential, allowing the electron wavepacket to tunnel through the potential barrier. When $\gamma \gg 1$, ionization occurs in the above-barrier regime. The effective Coulomb potential is lowered by the field such that it is below the ground state.

For the typical situation of neutral argon ($I_p = 15.76$ eV) interacting with an 800 nm laser pulse, tunnel ionization becomes the dominant mechanism for intensities greater than 10^{14} W/cm^2 [36]. A formalism for the tunnel ionization probability of an atom in an oscillating field, known as ADK ionization rate, was developed by Ammosov, Delone, and Krainov [37]. Using ADK rates, the ionized population as a function of time due to a laser field exhibits a stepwise increase at each half cycle of the fundamental laser pulse cycle. Typical intensities in HHG experiments are greater

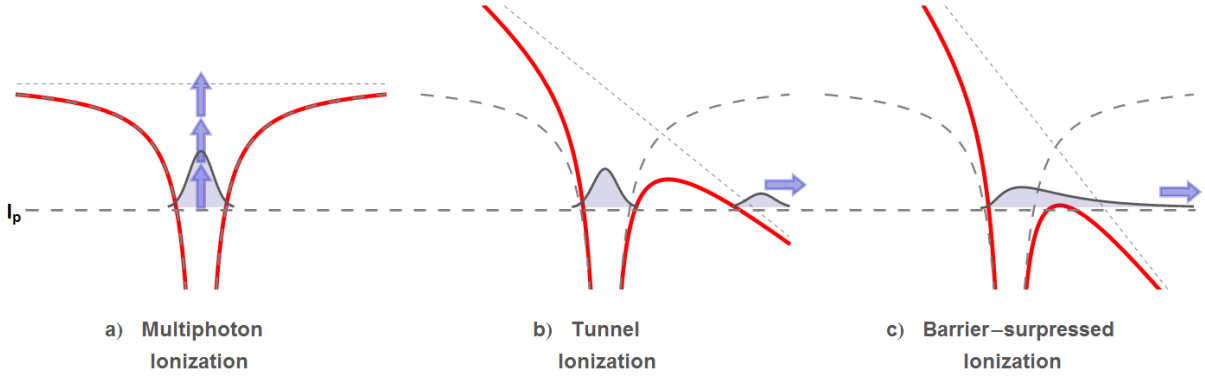

Figure 2.2: Schematic for photoionization processes for different laser intensities: a) multiphoton absorption ($\gamma \ll 1$), b) tunneling ($\gamma \leq 1$), and c) above barrier ionization ($\gamma \gg 1$). The gray dashed line corresponds to the Coulomb potential, while the red line corresponds to the Coulomb potential modified by the laser field.

than 10^{14}-10^{16} W/cm^2, making tunnel ionization the dominant ionization mechanism.

A semiclassical and therefore more intuitive description of HHG has been developed by Ken Kulander, Paul Corkum, as well as others, that explains HHG as a three-step process [7,9,38] where the parent atom is initially ionized, the electron is accelerated in a classical electric field due to the driving laser, and the accelerated electron recombines with the parent ion. This process is shown schematically in Figure 2.3.

The driving laser pulse electric field deforms the atom potential well, allowing part of the electron wavepacket to tunnel out of the well. After ionization, the electron wavepacket is then accelerated by the electric field of the laser and gains energy. When the electron recombines with the parent ion, it releases that energy in the form of a high energy photon. Solving the equations of motion for the electron classically (Equation 2.6) reveals that the maximum energy an electron can gain in the laser field and still recombine with the parent atom is given in terms of the ponderomotive energy and is $\approx 3.17U_p$.

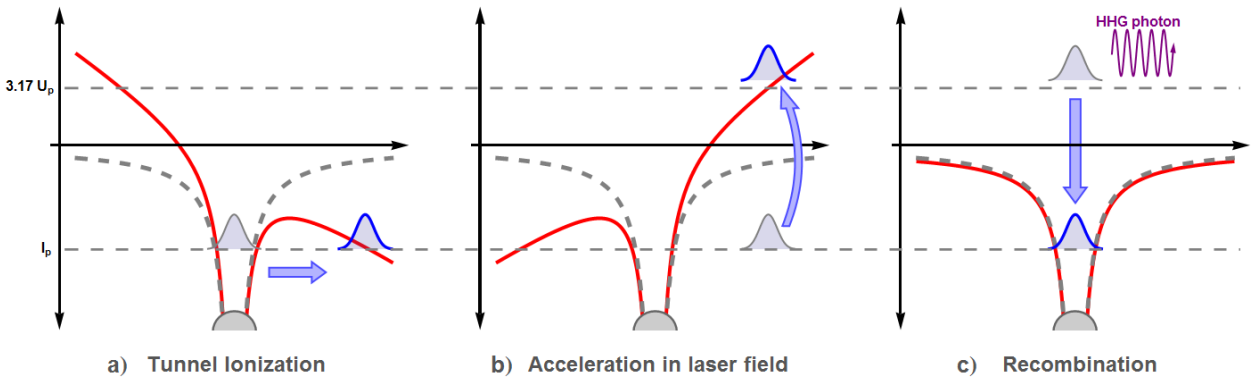

Figure 2.3: Schematic of the intuitive three-step model. The atom potential bends due to the driving laser pulse electric field, allowing part of the electron wavepacket to tunnel out of the well. The laser electric field accelerates the electron wavepacket causing it to gain energy. The electron then recombines with the parent ion releasing a high energy photon.

$$\begin{aligned} x(t) &= -\frac{eE_0}{\omega^2 m} cos(\omega t) + v_0 t + x_0 \\ v(t) &= \frac{eE_0}{\omega m} sin(\omega t) + v_0 \end{aligned} \tag{2.6}$$

The classically calculated value agrees with the cut-off of the harmonic plateau that was first observed experimentally [38]:

$$h\nu_{max} = I_p + 3.17U_p \tag{2.7}$$

The energy cut-off applies to the high harmonics generated from a single atom.

2.2.2 Phase matching/gas-filled waveguide

The three step model considers the high harmonic generation process in terms of a single atom. For high harmonic generation in bulk, one must consider the phase difference of the harmonics generated at different points in the medium. This difference can be described in terms of the coherence length:

$$L_{coh} = \frac{\pi}{\Delta k} \tag{2.8}$$

The coherence length is defined as the length necessary for a phase shift of π to develop between the signal that propagates over that length and the signal that is immediately generated. For high harmonic generation, it is the length over which the harmonic signal increases before interfering deconstructively due to the phase velocity mismatch of the high harmonics and the fundamental frequency. Without consideration to phase matching, the high harmonic flux that builds over a coherence length will then periodically interfere with out-of-phase light generated in the next section of the medium. Overall signal will not increase but will oscillate over each coherence length. Early attempts at high harmonic generation were typically done using a gas jet of noble gas [39], where the interaction length is limited by the size of the jet, so efficient generation of high-harmonics was not achieved. Later, phase matching in a hollow, gas-filled waveguide through pressure tuning was demonstrated [40,41]. The hollow waveguide results in a dispersion term ($\Delta \mathrm{k}_w$) in addition to the neutral gas ($\Delta \mathrm{k}_n$) and free electron ($\Delta \mathrm{k}_p$) terms. This waveguide term can be used to correct for the phase mismatch of the other terms. Assuming the neutral gas has an index of refraction ~ 1, and that the HHG signal is generated with a small spatial profile such that it does not interact with the waveguide, the phase mismatch in a hollow waveguide is given by:

$$\begin{aligned} \Delta k &= \Delta k_n + \Delta k_p + \Delta k_w \\ &= \frac{2\pi q P \delta_n (1-\eta)}{\lambda P_{atm}} - \frac{\eta P N_{atm} r_e}{P_{atm}}(q\lambda - \frac{\lambda}{q}) - \frac{q u_{nm}^2 \lambda}{4\pi a^2} \end{aligned} \tag{2.9}$$

where λ is the fundamental wavelength, q is the harmonic order, r_e is the classical electron radius, u_{nm} is a constant corresponding to the propagation mode in the waveguide, a is the waveguide radius, η is the fractional level of ionization, P is the gas pressure, P_{atm} is the atmospheric pressure, $\delta_n = n_{gas} - 1$ is the deviation of the neutral gas index of refraction from that of a vacuum, and N_{atm} is the gas density at atmospheric pressure. Phase matching thus requires a balance of the neutral gas term with the resultant plasma dispersion against the dispersion of the waveguide. This is primarily done by adjusting the gas pressure inside of the waveguide.

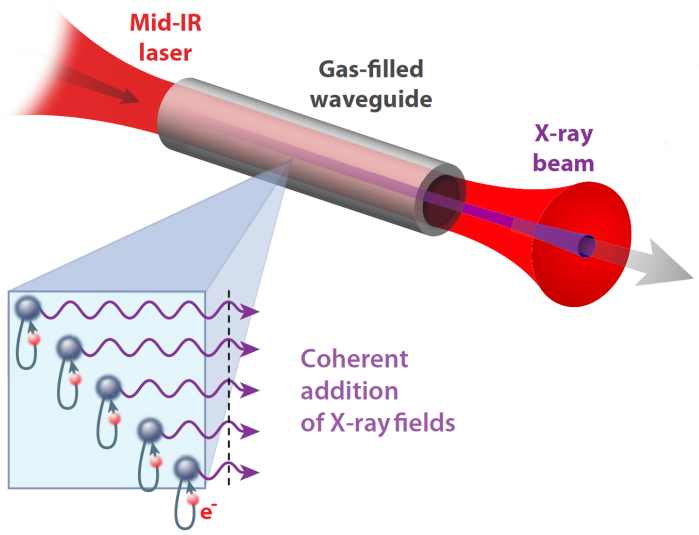

Figure 2.4: Coherent phase matching of high harmonic photons in a gas filled waveguide. High harmonic XUV light copropogates with the driving beam. From [6].

Figure 2.5 illustrates the concept of phase matching with a gas-filled waveguide. The gas pressure inside the waveguide, P in Equation 2.9, acts as a tunable knob that can be controlled. This allows for experimental control over the term Δk_p so that Δk is close to 0 causing L_{coh} to be maximized. For appropriate pressures, tuning the pressure will change the frequencies that are best phase matched, as well as provide a bright harmonic source with enough flux for efficient detection.

Figure 2.5(a) shows the photoelectron energies for an argon target in the gas jet and xenon gas in the high harmonic waveguide. As discussed in Section 2.3, the harmonics above the ionization potential of argon, 15.76 eV, are the signal that is visible. The 11th and 13th harmonic of the driving laser are always above that potential. As the pressure is increased the phase matched high harmonics blueshift. Also shown is how the high harmonic energies affect the ionization yield as they are tuned in part (b). When the 9th harmonic is below the ionization threshold the presence of an additional IR photon allows for ionization, giving a strong enhancement of ionization counts, shown in the positive delays. Once the 9th harmonic is tuned above the ionization threshold the enhancement disappears. This demonstrates the importance of controlling pressure in the

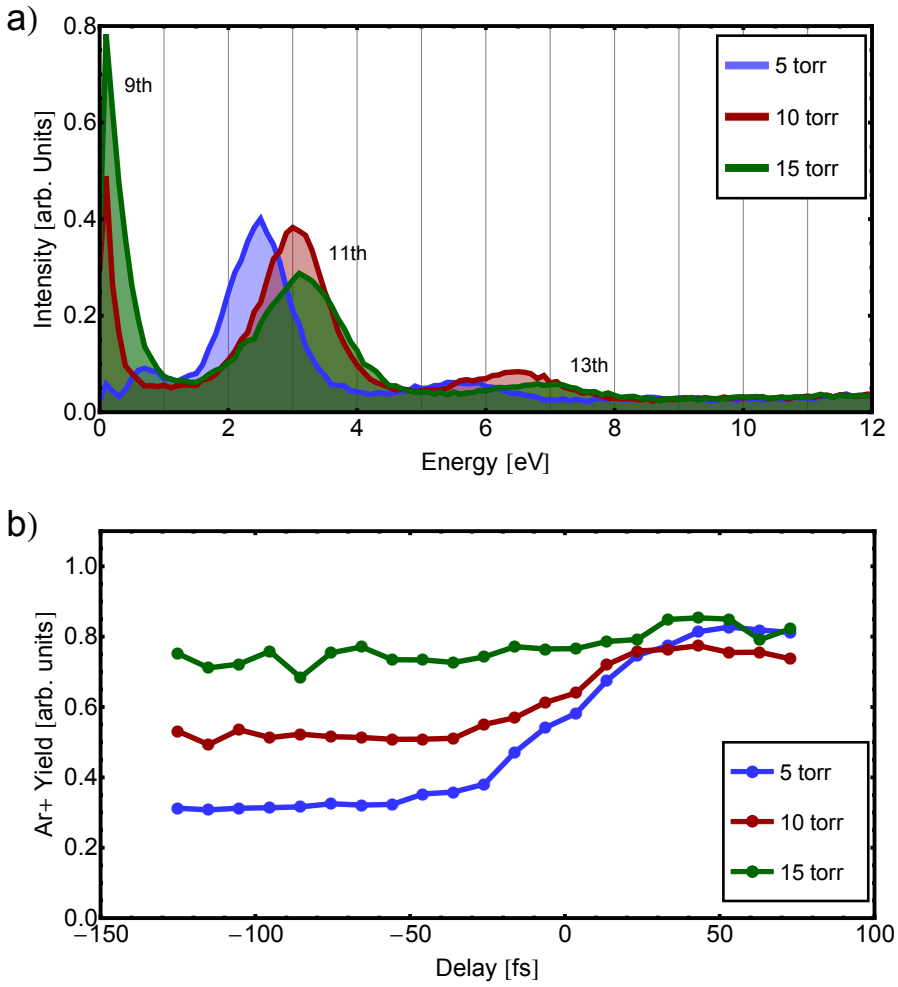

Figure 2.5: Because of the control over the phase matching conditions the harmonics can be tuned towards a resonance. Part a) shows photoelectron energies for three different gas pressures inside of the capillary. The 11th and 13th harmonic of the driving laser are always above that potential and as the pressure is increased the phase matched high harmonics blueshift. The 9th harmonic eventually blueshifted above the ionization threshold. Part b) shows the ionization yield as a function of IR probe delay. Once the 9th harmonic is tuned over the ionization threshold the presence of the IR probe does not induce further ionization and the yield becomes flat versus delay.

waveguide. A full explanation of the time delay is given in Section 2.4.

2.3 COLTRIMS

The cold target recoil ion mass spectrometry (COLTRIMS) reaction microscope detects the charged particles that are generated by an atom or molecule interaction with photons (from the

IR pulse, XUV pulse or a combination). The charged particles are guided to position sensitive detectors by electric and magnetic fields. The detectors allow for full momentum reconstruction of each detected particle which in turn captures the atomic or molecular dynamics.

Figure 2.6 shows the paths of the electrons and ions detected for a typical coincidence experiment (results in Chapters 7 and 8 show specific results for such an experiment). The Figure shows the electrons undergoing a spiral path because of the cyclotron motion of the uniform magnetic field. The two positive ions shown have a conservation of momentum that allows for filtering against false background coincidences.

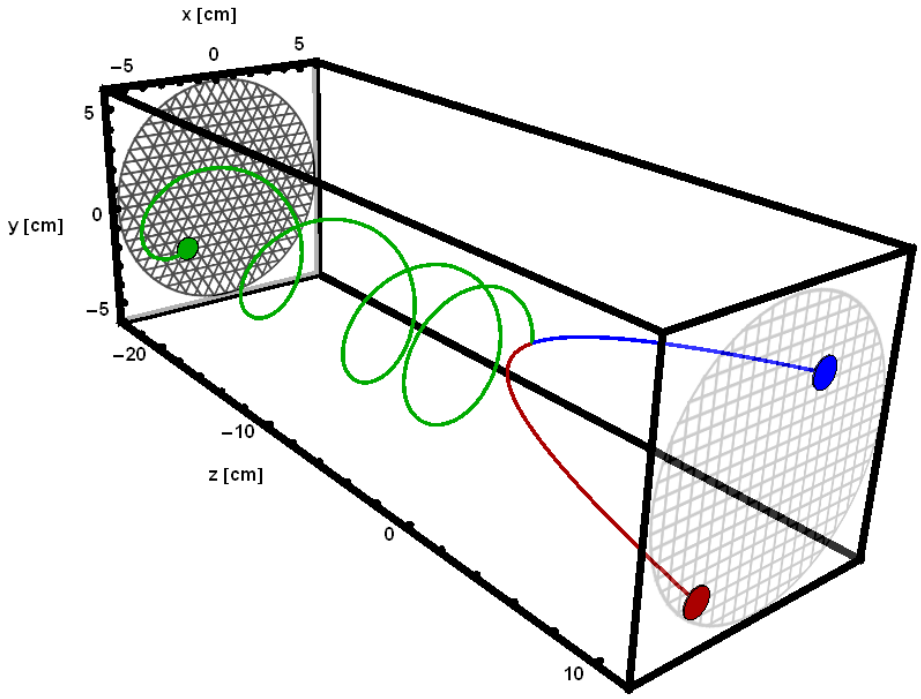

Figure 2.6: Schematic showing the typical paths for ions and electrons in COLTRIMS. The electrons take a spiral path because of the cyclotron motion of the uniform magnetic field. The electrons are accelerated in the same uniform electric field as the ions initially and then go through a zero field drift region. The more massive ions do not experience noticeable deflection due to the magnetic field. Two positive ions are shown dissociating from the interaction region. Note that a second electron is not shown for clarity and represents a realistic coincidence collection of the detector.

A schematic of the COLTRIMS geometry as well as the axis convention that will be used

throughout this text is shown in Figure 2.7. The calculation for the momenta reconstruction requires exact knowledge of the parameters of the detector (electric field, magnetic field, and acceleration distances) as well as the initial position and final position of a charged particle. The individual components of the spectrometer and of the detector and the analysis are given in this Section.

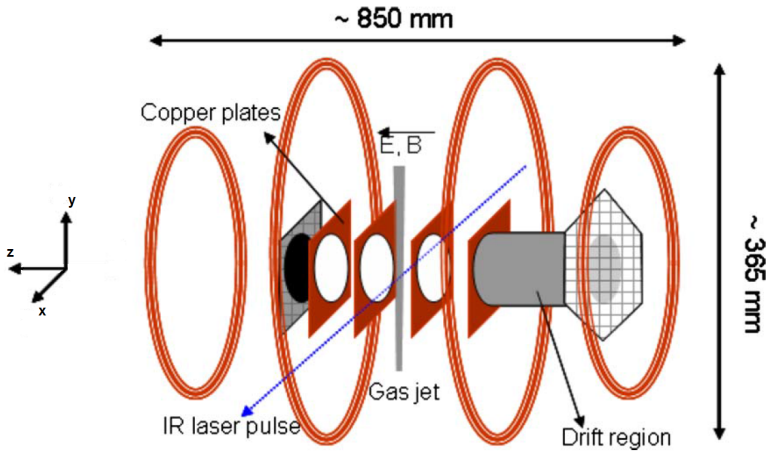

Figure 2.7: Simplified schematics of COLTRIMS showing a smaller representative number of copper plates to form the electric field, the copper coils to form the magnetic field, and ion and the electron detectors. Adapted from [42].

2.3.1 Gas Jet

The COLTRIMS detector was originally designed to only support a supersonic molecular beam; a effusive jet was later added to expand the range of available experiments. It was determined that a supersonic gas jet would provide a better sample over an effusive needle where a needle needs to be close to the interaction region. The supersonic jet provides a much more confined interaction region and greatly decreases the thermal broadening of the energy features. It was also believed it would allow for a better controlled main chamber pressure. However, the limitations of seeding a relatively small interaction region and requiring a high backing pressure make having both the supersonic jet and effusive needle available incredibly advantageous in allowing the study of many

molecules that could not be studied otherwise. A good example of such an experiment was ozone, as discussed in Chapter 8, where high backing pressures of ozone are both impossible to form as well as potentially dangerous. Ozone spontaneously detonates above 20 torr.

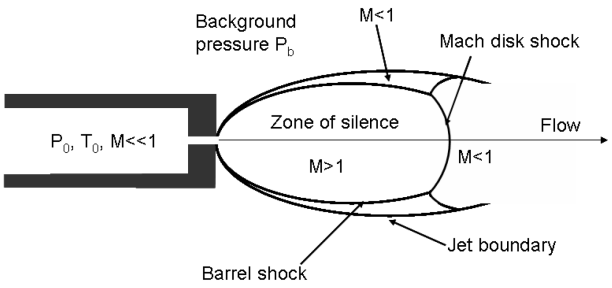

Figure 2.8: Schematic showing the area of stability from in a continuum free-jet expansion. From [42].

The supersonic gas jet is created by the expansion through a 30 μm nozzle. The input side of the nozzle is kept at over 1 atm while the output side is maintained at 5×10^{-5} torr. A low divergence portion of the supersonic expansion is selected by a 300 μm skimmer. The skimmer also serves as a barrier (differential pressure) between the gas jet chamber and the detector chamber. The geometrical shape of the gas jet chamber helps with gas conductance and with efficiently evacuating the background gas to keep the gas jet chamber pressure low. The gas jet chamber is pumped by a 2000 L/s MAG turbo pump (from Leybold). The area around the skimmer is also shaped as a cone to help reduce possible back-scattering that would be detrimental to the gas jet.

For the experiments discussed in Chapter 5, the main detector chamber included a 'catcher' to minimize the increase in the chamber pressure. A tube was inserted inside the chamber with its orifice as close to the interaction region as the detector allows ($\sim$9 cm). The tube is directly connected to a small pumping chamber and turbo pump (300 L/s) to efficiently evacuate the gas. Despite this, the detector chamber pressure would typically increase to 1×10^{-7} torr during gas jet operation (compared to a pressure of 2×10^{-9} torr in standby mode). It was later determined that this was not the limiting factor in minimizing the main chamber pressure during operation.

The catcher (the turbo pump and differential pumping) was replaced so the port could be used to build the effusive gas jet.

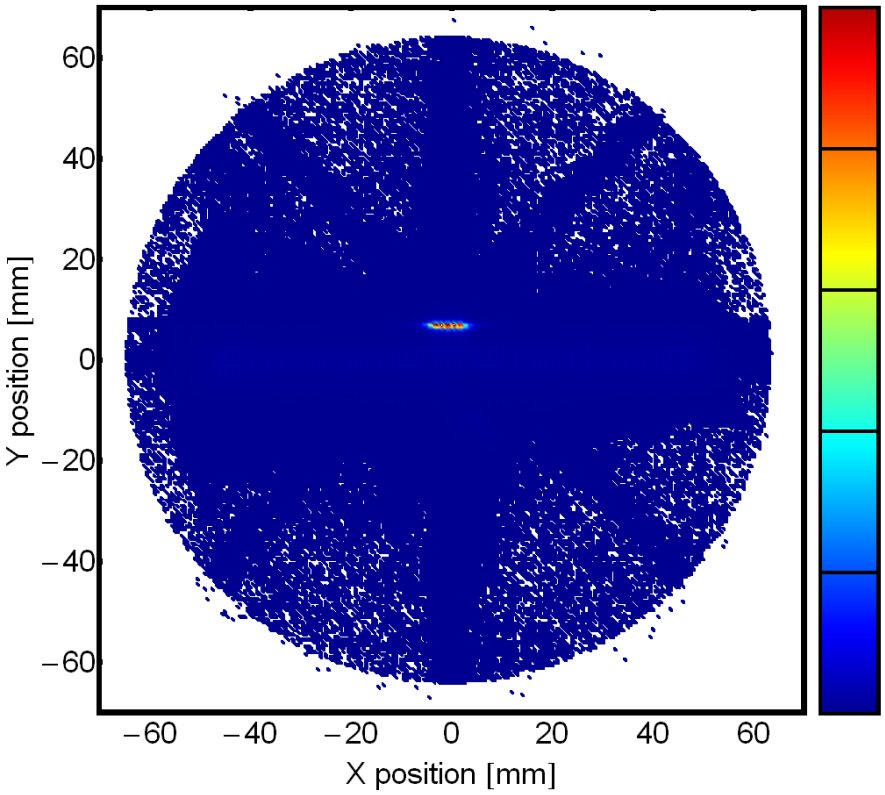

Figure 2.9: Ion DLD image for the supersonic gas jet. A faint horizontal line along the center of the detector arises from the interaction of the XUV pulse train propagating through the chamber interacting with the background gas. The intense region at the center is the interaction of the XUV pulse train with the supersonic gas jet where the molecules have a high initial momentum in the positive y direction.

Figures 2.9 and 2.10 show the distinct difference between the supersonic and effusive gas jets on the ion delay-line detector (DLD) image. A description of this detector will be given in Section 2.3.4. The Figures show the supersonic jet is much more localized, causes very little background signal and therefore provides an effective means to filter the data. Figure 2.9 is an image of the x and y position of the ion impacts on the delay line detector that will be described in more detail in Section 2.3. In both Figures 2.9 and 2.10 there is a faint horizontal line of greater counts centered on the detector and a small intense region offset in the y direction. The line shows the propagation

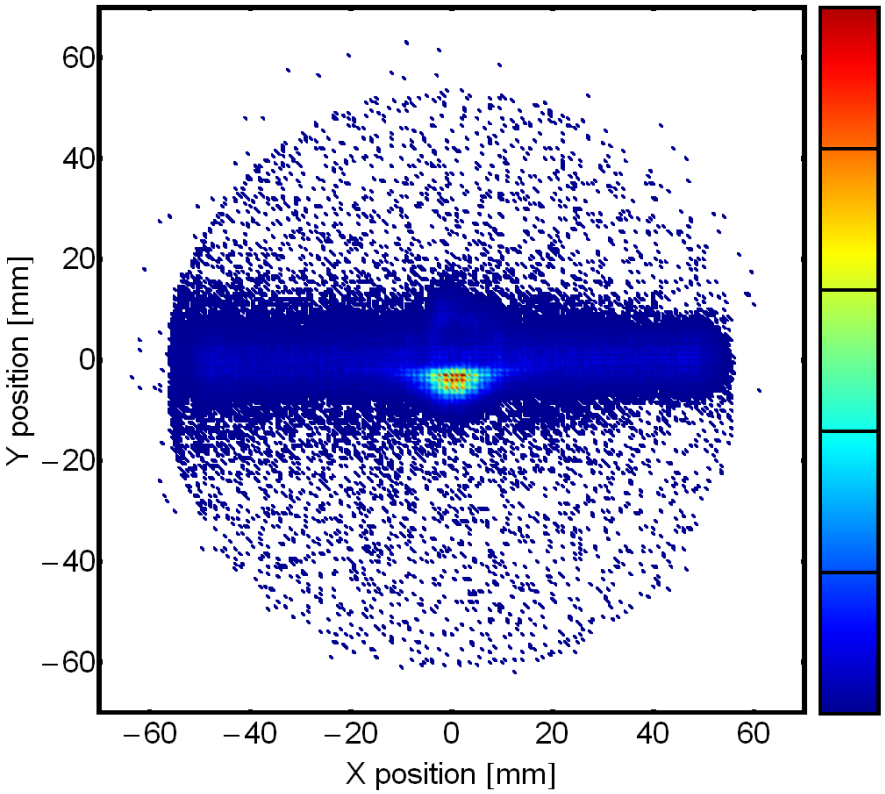

Figure 2.10: Ion DLD image for the effusive gas jet. A faint horizontal line along the center of the detector arises from the interaction of the XUV pulse train propagating through the chamber interacting with the background gas. The intense region at the center is the interaction of the XUV pulse train with the effusive gas jet where the molecules have a lower initial momentum compared to the supersonic jet, and in the negative y direction.

of the XUV ionizing background gas. The small offset region corresponds to ionization events from each gas jet. The offset comes from the y momentum component, in the positive y direction for the supersonic gas jet and in the negative y direction for the effusive gas jet. Considerable care must be put into achieving the correct backing pressure for the effusive jet so that the main chamber pressure is not prohibitively raised. A high background pressure will cause the detectors to saturate with counts, obscuring the jet signal and possibly causing damage to the detectors. Even when achieving the correct pressure there is still a much greater background signal than with the supersonic jet. While the increased count rate with the effusive jet is necessary for certain experiments it must be weighed against a decreased signal-to-noise ratio due to the significant background counts. A major

advantage of COLTRIMS is being able to filter for counts originating only from certain pathways, which can include filtering on events only from the interaction region.

Because the effusive jet must be inserted within the copper plates which generate the electric field it must be biased at the correct voltage in order to appear 'invisible' within the electric field. A simple calculation can be done using the set potentials of the two ends of the copper plates. Further adjustment can be done experimentally by minimizing the spread of the ions from the gas jet.

The supersonic jet provided the source for experiments in Chapter 5 and Chapter 7. The effusive gas jet was used in experiments in Chapter 4 and Chapter 6. Both jets are discussed in Chapter 3 and Chapter 8.

2.3.2 Electric Field

A series of copper plates connected to a resistance chain creates an even potential drop, producing a near-uniform constant electric field. These copper plates surround the interaction region and are responsible for the acceleration of both the ions and electrons. There are 41 copper plates connected in series with 100 kΩ resistors. A typical experiment puts the voltage at -150 V on the plate closest to the electron detector and -450 V on the plate closest to the ion detector. Giving the acceleration region an overall negative potential relative to the grounded vacuum chamber prevents low energy background electrons from being accelerated and detected. The 3 center plates are cut to allow the insertion of the laser and the supersonic gas jet. The acceleration region is approximately 119 mm in the direction of the ion detector and 125 mm towards the electron detector.

There is an area with no electric field referred to as the drift region between the acceleration region and the electron detector that is approximately 245mm long. The region is kept at the same negative potential as the electron end of the acceleration region (typically -150 V), again to reduce low energy background electrons from being detected. This region is designed to refocus the electrons in the time-of-flight direction, correcting for systematic error due to the size of the

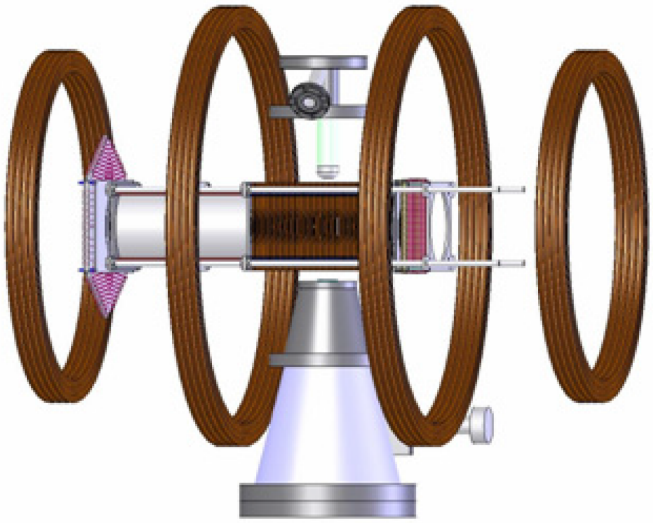

Figure 2.11: Schematic of the spectrometer inside the vacuum chamber. The main magnetic copper coils and the gas jet chamber and catcher are also shown. The catcher, used for earlier experiment to maximize signal to noise, was later replaced with an effusive gas jet used to increase the count rate. From [42].

interaction region. The interaction region's size is set by the finite spot size of the laser focus and the gas jet. Electrons ionized closer to the detector will spend less time in the acceleration region and have a slower velocity in the time-of-flight direction than electrons ionized further from the detector. The electrons ionized further from the detector will therefore arrive at the detector closer in time to the electron that was ionized nearer to the detector. Such a region is not necessary for the ions, as they will not experience the same degree of spread because of their larger mass.

2.3.3 Magnetic Field

A constant magnetic field in the same direction as the electric field is generated by four coils of copper wire. The purpose of the magnetic field is to allow for 4π angular resolution of high energy electrons. Electrons with large momentum perpendicular to the time-of-flight direction that would otherwise escape detection will be put into cyclotron motion, allowing them to be accelerated

towards the detector. Each coil is made up of 100 turns of 10 gauge square copper wire with a typical current of 2.7 A and producing an overall magnetic field of approximately 5.5 Gauss. An additional four coils of wire are used to fine tune the magnetic field in the x and y directions to correct for the Earth's magnetic field. These coils are 37 turns of computer cable and carry approximately 1.7 A of current.

The magnetic field in the x and y directions can be adjusted to center low energy electrons on the detector. The magnetic field in the z (time-of-flight) direction must be adjusted to detect the highest energy electrons. Because the motion is dependent on the magnetic field a simple calculation for the maximum radius detected can be done:

$$r_e = 2\frac{\sqrt{2m_e K_e}}{qB} \tag{2.10}$$

where K_e is the electron's kinetic energy, m_e is the electron mass, q is the fundamental charge, and B is the magnetic field.

As the magnetic field is changed depending on the experiment, it can be calibrated by lowering the electric field so that there are multiple periods of cyclotron motion. The time between nodes gives the magnetic field according to:

$$B = \frac{2\pi m_e}{e\tau} \tag{2.11}$$

where τ is the time between nodes.

Figure 2.12 shows a plot of electron radius of detection versus time-of-flight with a typical calibration set-up. Multiple nodes can be used to accurately find τ and therefore find B.

2.3.4 Detection

Detection of the charged particles is done with microchannel plates (MCP) on each side of the spectrometer, coupled with a delay-line detector (DLD). Each MCP is biased at approximately 2.1 to 2.6 kV, set to maximize detection. Behind each MCP there is a wire grid delay line detector.

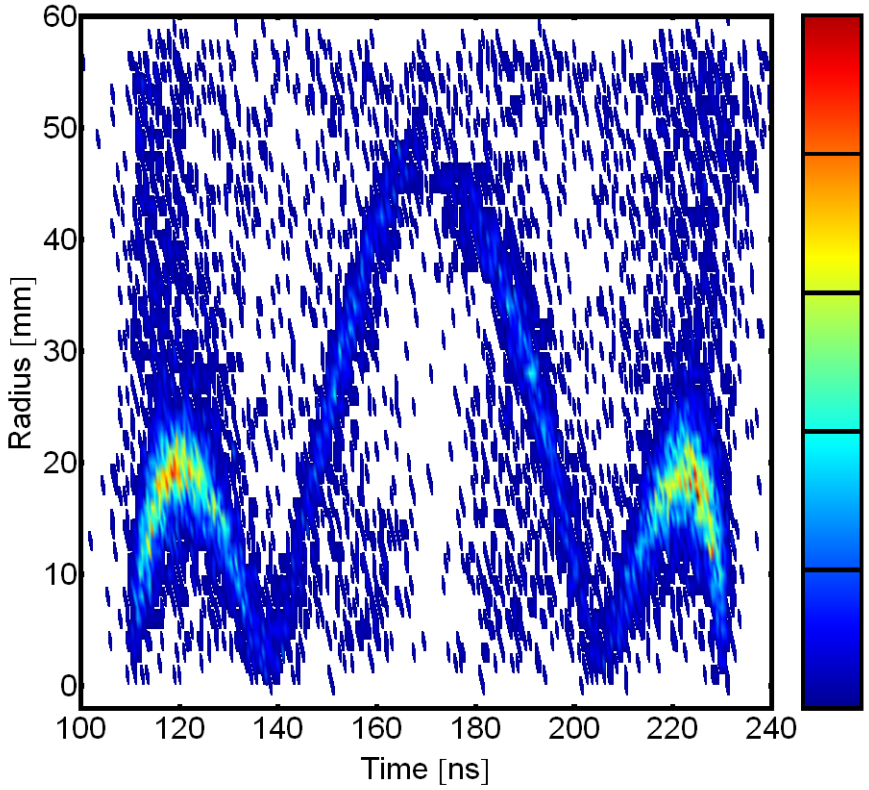

Figure 2.12: A plot of electron counts with their radius from the center of the detector vs. time-of-flight. With a lower electric field multiple nodes are present and can be used for magnetic field calibration as well as an effective measurement for time zero. For data collection, the electric field is adjusted to avoid multiple nodes when possible to maximize resolution.

Each channel on the plate acts as an electron multiplier producing a signal that then travels to the delay line detector ("DLD" for ions and "HEX" for electrons) where it generates a small, measurable current. The pulse of current travels both directions along the wire and the time of the signal is recorded and then compared to a common fixed trigger signal taken from the laser amplifier. By comparing the detection of one end of the wire to the other it provides the position of the particle detected. Comparing the signals to the common trigger provides the time of detection. Assuming the initial position from the interaction region, knowledge of the time-of-flight, and final x and final y positions provides the ability to determine the full momentum of the particle detected.

The MCP for each detector has an active diameter of 120 mm. Consideration must be given

to setting up the experimental conditions such that the detector provides maximum resolution. By maximizing the active area of detection energy resolution can be improved, however care must be taken that counts can be 'missed' on the edge of the detector.

The electrical signal from each delay line is digitized to be recorded. First, each electrical signal passes through a set of differential amplifiers and constant-fraction discriminates in a commercial RoentDek ATR19 module. This provides an adjustable threshold to filter real signals from background noise. The signals are amplified and made into negative nuclear instrumentation module (NIM) pulses. Figure 2.13 shows a schematic of the electronic signal processing. Electronic signals from the DLD are amplified before converted into a digital signal withEach module has a dead time of more than 20 ns. This can present an issue with multi-hit detection. The NIM pulses go to an 8 channel time-to-digital converter (TDC) each using a LeCroy MTD133B chip. Each TDC has a resolution of 500 ps and can acquire up to 16 hits per laser shot. The TDCs has a deadtime around 10 ns. Software provided by RoentDek processes and records the data from the TDCs to the hard disk. More detailed technical information of the various components of the COLTRIMS detector can be found in the RoentDek manuals available on their website (www.roentdek.com) and [42].

While multiple hits can be recorded with each laser pulse, this should not be mistaken for the ability to detect several separate ionization events. Detection is set up with the goal of achieving one real coincidence event with each pulse. Because of Poisson statistics the expectation value must be kept less than one event per shot in order to prevent increasing the number of 'false' coincidences caused by multiple ionization events. Once certain experimental conditions have been met, increasing the flux rate of either the number of photons or particles in the gas jet is not beneficial to detection. This was mentioned briefly in Section 2.1 and is the reason for needing such a high of a repetition rate from the amplifier while still producing high energy pulses to create high harmonics and generate the desired molecular dynamics.

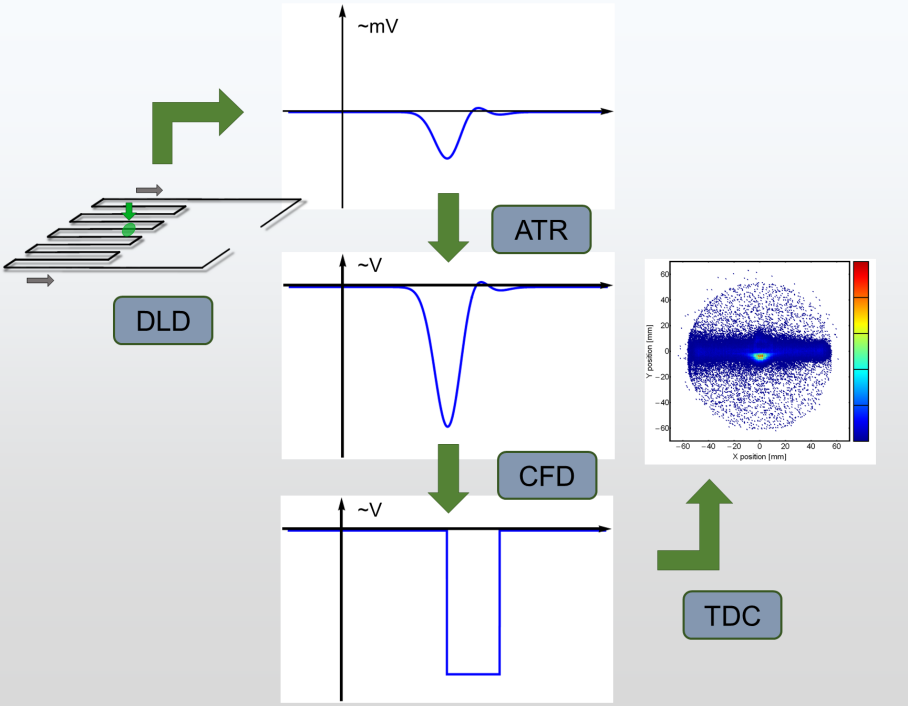

Figure 2.13: A schematic of detection, signal processing by the electronics and digital conversion. It is important to note that the differential amplifier and constant fraction discriminator occurs within the same module (ATR19) though each waveform can be viewed.

2.3.5 Equations of Motion

The paths of ions in the system can be described by the equations of motion for the ion detector. Using the known parameters of the apparatus and the time and position detection information the ion momentum can be calculated:

$$p_{i,x} = \frac{m_i x_i}{TOF_i} \tag{2.12}$$

$$p_{i,y} = m_i \left(\frac{y_i}{TOF_i} - V_{jet} \right) \tag{2.13}$$

$$p_{i,z} = \frac{m_i L_i}{TOF_i} - \frac{qE}{2} TOF_i \tag{2.14}$$

Where (x_i,y_i) is the final ion position, TOF_i is the ion time of flight, L_i is the length of the

ion acceleration region, m_i is the ion mass, and V_{jet} is the gas jet velocity, q is the fundamental charge and E is the electric field. The equations assume a centered initial position.

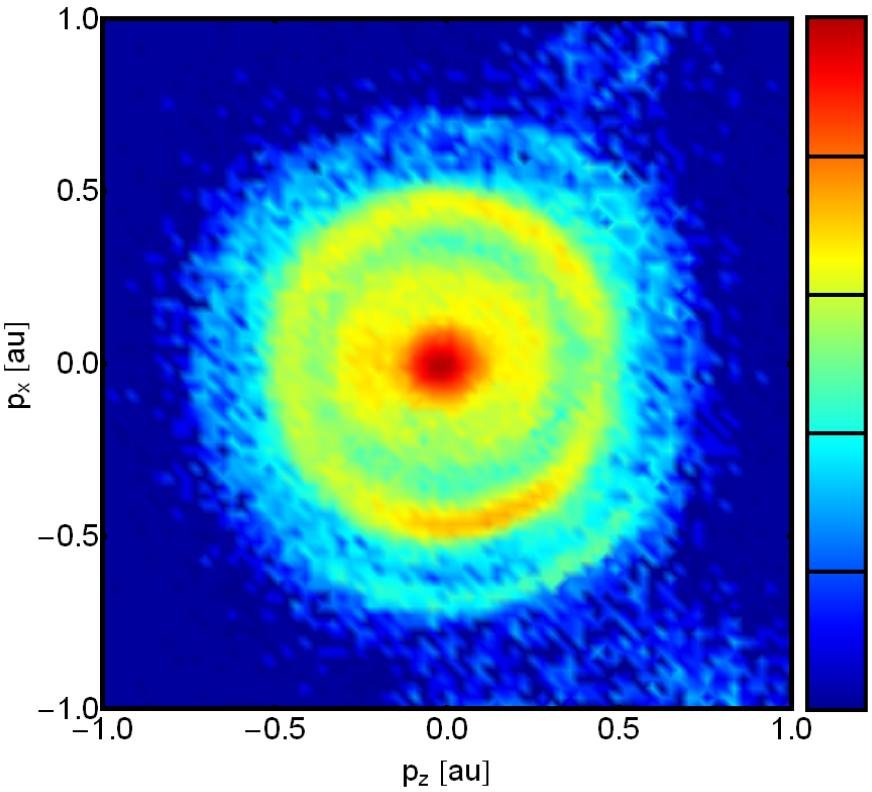

Figure 2.14: A plot of electron momentum showing the capability to determine the exact harmonic energies of the high harmonics from the photoelectron energies. The data has been filtered to take a narrow slice of values in y momentum.

Figure 2.14 shows the capabilities of the electron detector. Four clear energies are visible in the momentum distribution of the photoelectrons from argon. Getting such a distribution requires setting the experimental parameters exactly.

Equations of motion for the electron detector:

$$p_{e,x} = \frac{qB}{2}\left(-x_e cos\left(\frac{qE}{2m_e}TOF_e\right)/sin\left(\frac{qE}{2m_e}TOF_e\right) + y_e\right) \tag{2.15}$$

$$p_{e,y} = \frac{qB}{2}\left(y_e cos\left(\frac{qE}{2m_e}TOF_e\right)/sin\left(\frac{qE}{2m_e}TOF_e\right) - x_e\right) \tag{2.16}$$

$$p_{e,z} = -m_e \left(\frac{L_{e,d}}{TOF_e - TOF_{e,a}} - \frac{qE}{m_e} TOF_{e,a} \right) \tag{2.17}$$

where (x_e,y_e) is the final electron position, B is the magnetic field, TOF_e the electron time of flight, $L_{e,a}$ is the length of the electron acceleration region, $L_{e,d}$ is the length of the drift region, m_e is the mass of the electron, and $TOF_{e,a}$ is the time of flight of the electron inside the acceleration region. Because $TOF_{e,a}$ is not a measurable quantity with the apparatus it must be solved for by inserting equation 2.17 into

$$L_{e,a} = \frac{p_{e,z}}{m_e} TOF_{e,a} + \frac{qE}{2m_e} TOF_{e,a}^2 \tag{2.18}$$

which produces the following third order equation:

$$\left(\frac{qE}{2m_e} \right) TOF_{e,a}^3 + \left(\frac{-qE}{2m_e} TOF_e \right) TOF_{e,a}^2 + (L_{e,a} + L_{e,d})\, TOF_{e,a} - L_{e,a} TOF_e = 0 \tag{2.19}$$

This is equation is solved for within the COLTRIMS analysis routine.

Similarly consideration must be given to making sure the ion detector is maximized for resolution but that counts are not missed. With the knowledge of the expected maximum kinetic energy release (K_{KER}) of two positively charged ions, the electric field (E) can be set by the equation:

$$E = \frac{2m_i L_i}{qR_{DLD}^2} \left(V_{jet} + \sqrt{2 \left(\frac{m_2}{m_1} \right) \left(\frac{K_{KER}}{m_1 + m_2} \right)} \right)^2 \tag{2.20}$$

where R_{DLD} is the radius of the DLD MCP.

2.4 Beam Line

Time domain spectroscopy requires the ability to optically start an atomic or molecular dynamic and then probe the molecule with a second pulse at various time delays. The short duration of the amplified Ti:sapphire pulses as well as the high harmonic generation provide the

Ion Holder	65 V
Ion Signal/Reference	180 V
Ion MCP back	0 V
Ion MCP front	-2100 V
Ion Spectrometer End	-450 V
Electron Spectrometer End	-150 V
Electron MCP Front	-24 V
Electron MCP Back	2650 V
Electron Signal/Reference	2800 V
Electron Holder	2900 V

Table 2.1: Typical operating voltages for COLTRIMS.

time resolution as the second pulse is scanned. The beam path geometry for the XUV-IR, pump-probe configuration that was used for all atomic and molecular dynamics experiments with the exception of Chapter 5 is shown schematically in Figure 2.15. For Chapter 5 a cross-beam geometry was used. The 800 nm (IR) beam out of the amplifier is split before the XUV waveguide. The XUV pulse is generated in the waveguide and its output mode is imaged to the center of the COLTRIMS main chamber with a pair of multilayer mirrors specifically coated for our apparatus, each designed to reflect one or more of the harmonics. One of the mirrors has a 1 m radius of curvature, allowing for 1-to-1 imaging of the output of the waveguide to the interaction region of the detector. The IR light is sent through a variable delay stage and is recombined collinearly with the XUV beam using a mirror with a 3 mm drilled hole in the center.

The variable time delay between the IR and XUV beams is controlled by a motorized stage, with a total travel of 5 cm. Using our own calibration we found the smallest step size allowed was 260 attoseconds and the setup was interferometrically stable for sub-optical cycle resolution. The IR beam is focused into the center of the detector with a 2 m radius of curvature mirror. While previous work used a lens for focusing, it was determined that this produced too much dispersion and would not allow for a short pulse in the interaction region. Due to the pump-probe geometry, it is difficult to precompensate for the added dispersion with a transmissive optic in only one arm of the interferometer without affecting the stability. The recombination mirror only reflects an annular portion of the IR beam and therefore loses much of its intensity. Previous calculations

show that the focal spot size only changes by a few percent compared to a Gaussian profile, though consideration must be taken for the lost energy [42]. With typical experimental conditions the IR beam focuses to approximately 50 μm in diameter.

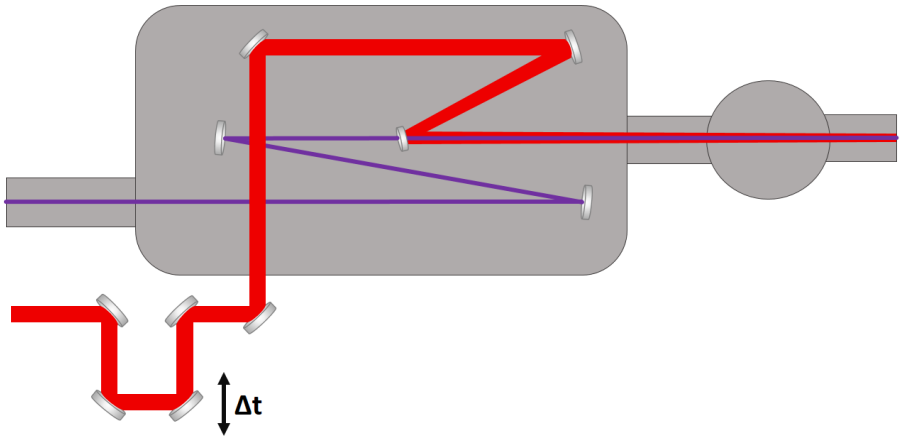

Figure 2.15: Schematic of the recombination of the XUV and IR beam lines before entering the COLTRIMS main chamber. The high harmonic beam reflects off of two multilayer mirrors before passing through the center of an annular mirror. The IR beam is focused with a curved mirror directly before being collinearly recombined with the annular mirror.

The XUV spot size is also approximately 50 μm in diameter. This number is approximated by assuming good imaging of the waveguide output to the center of the detector. The gas-filled capillary has an inner diameter of 150 μm and only portions of the guided wave with sufficient intensity cause the high harmonic process. We assume to be close to the optimal waist size of $\omega_0 = 0.64a$ where a is the inner bore radius [6].

Overlapping the XUV and IR beams temporally and spatially in the interaction region is done with a kick-out mirror in the differential pumping chamber. A CCD camera is placed at the same distance as the interaction region inside the COLTRIMS chamber. This allows for accurate resolution of each beam's spatial profile. The IR beam that copropagates with the XUV can pass outside of vacuum and can be used to find temporal overlap by looking for constructive and destructive interference fringes from the two coherent beams. This interference allows for

a measurement equivalent to a cross correlation. The XUV beam follows the same path as its copropagating IR. This procedure assumes the IR beam is well aligned with the XUV waveguide. Because the beams are collinear, once spatial overlap is found, it should be consistent along the beam path. Spatial overlap is therefore checked after the beams pass through the COLTRIMS chamber as well.

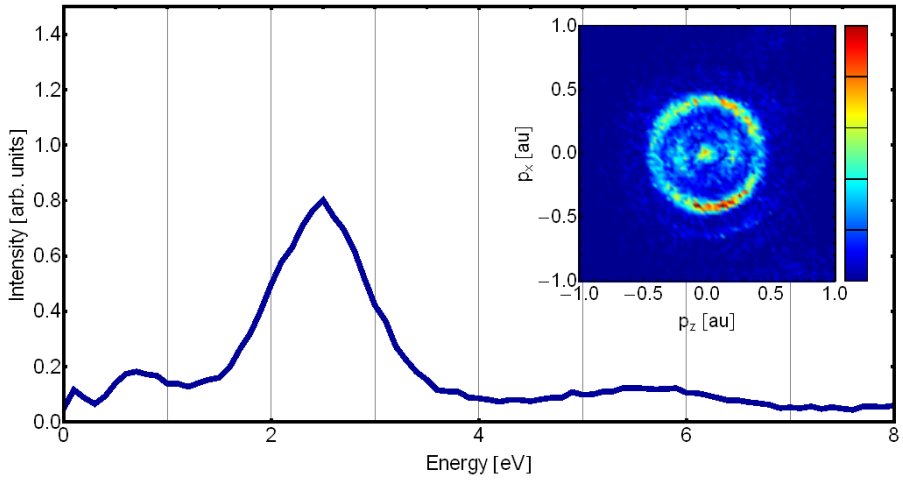

Figure 2.16: A plot showing typical electron momentum and electron energy which demonstrates the capability to determine the exact frequency of the high harmonics from the photoelectron energies. This requires exact knowledge of the detector parameters but allows for knowledge of the XUV pulse train energies.

Figures 2.16 and 2.17 give an example of checking spatial and temporal overlap with the detector. Figure 2.16 shows the photoelectron energies and momentum distribution for ionization due to only the XUV pulse. As shown clearly by the inset of the electron momentum, the ionization comes primarily through the 11th harmonic which sits well of above the ionization threshold of argon. The 13th harmonic is also visible.

Figure 2.17 shows the photoelectron energies and momentum distribution changed for ionization due to the XUV pulse overlapped with the IR pulse. An effective 10th harmonic energy peak appears due to the interaction of the XUV and IR. This interaction allows for a 9th + 1ω and 11th − 1ω interaction. Figure 2.17 is normalized for comparison purposes and does not show the increased count rate from Figure 2.16. The calculation of photoelectron energies will be discussed

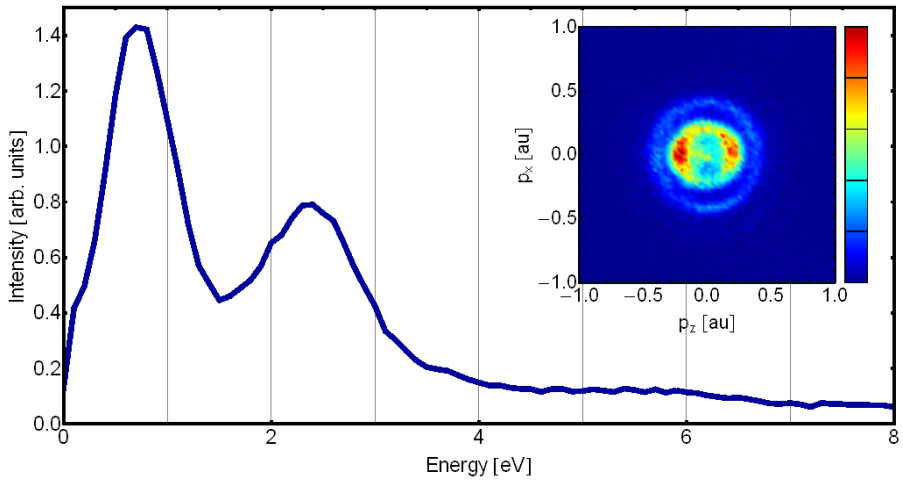

Figure 2.17: A plot showing typical electron momentum and electron energy which demonstrates the capability to determine the photoelectron energies in the presence of both the high harmonic pulse train and the IR pulse during temporal overlap.

in further detail in Section 2.7.

After high harmonic generation, the beam line must be in vacuum until it reaches the detector in order to allow the XUV light to propagate. The deep UV and XUV portions of the spectrum are highly dispersive and absorptive in the atmosphere. This presents experimental difficulties, as the most sensitive optics for beam alignment must also be under vacuum. Motorized mirror mounts are used for the multilayer mirrors. A 300 L/s turbo pump, designed to maintain a 10^{-5}-10^{-6} torr pressure inside the box, was decoupled from the recombination vacuum box to allow for interferometric stability.

A second prechamber exists to allow for the "kick-out" mirror to be inserted to check for spatial and temporal overlap as well as to maintain a low operating pressure in the main chamber through differential pumping. This kickout chamber is pumped with an additional 300 L/s turbo pump and contains none of the possible outgassing components of the recombination chamber. An additional aperture was added to allow for differential pumping between the kickout chamber and multilayer mirror chamber in additional to the existing differential pumping before the main chamber. With the addition of this 6 mm aperture the main chamber can maintain an operating

pressure below 5×10^{-9} torr while open to the beam line.

Chapter 3

Argon[1]

This Chapter will discuss the results and analysis for studies done with argon as the target in the gas jet with applications to other noble gases. The Chapter covers several experimental photon energies and set-ups that all contribute towards a greater level of understanding. In rare-gas atoms, Auger decay in which an inner-valence shell ns hole is filled is not energetically allowed. However, in the presence of a strong laser field, a new laser-enabled Auger decay channel can open up to increase the double ionization yield. This process is efficient at high laser intensities, where an ns hole can be filled within a few femtoseconds of its creation. This novel laser-enabled Auger decay process is of fundamental importance for controlling electron dynamics in atoms, molecules, and materials.

3.1 Laser Enabled Auger Decay

Auger decay is an important decay process in highly excited systems, that is, relevant to radiation physics, x-ray spectroscopy, x-ray lasers, and atmospheric chemistry. In Auger decay, absorption of a high-energy photon leads to the ejection of an inner-shell primary photoelectron. The resulting hole is then filled by an electron from an outer shell, with any excess energy carried away by ejecting a second Auger electron. Advances in laser and x-ray technology now make it possible to create an inner-shell core hole using a femtosecond or attosecond burst of x-rays

[1] The results of this chapter are in part based on "P. Ranitovic, X. M. Tong, C. W. Hogle, X. Zhou, Y. Liu, N. Toshima, M. M. Murnane, and H. C. Kapteyn, Phys. Rev. Lett. **106**, 053002 (2011)" [43] and "X. M. Tong, P. Ranitovic, C. W. Hogle, M. M. Murnane, H. C. Kapteyn, and N. Toshima, Phys. Rev. A **84**, 013405 (2011)" [44].

and to observe or manipulate the resultant photoelectron or Auger electron using an ultrafast infrared (IR) laser. Laser-assisted photoemission was first observed in atoms and more recently in solids [45, 46]. It is now used to characterize x-ray pulses and to capture fast electron dynamics in atoms and materials [32, 47]. In a laser-assisted process, an atom or material is simultaneously irradiated by ultrafast x-ray and laser pulses. Characteristic sidebands appear surrounding the photoemission and Auger peaks, corresponding to simultaneous absorption and emission of laser photons in addition to the x-ray photon. The magnitude and shape of these sidebands change as the time delay between the x-ray and laser pulses is changed, encoding information about the x-ray pulse duration as well as any underlying electron dynamics in the atom or material [48–52]. However, to date laser-assisted Auger decay represented a means by which an existing Auger decay channel could be modified and exploited. It was not understood that a strong laser field can also turn on and control the Auger decay process itselfwhich is a fundamental decay mechanism for matter exposed to ionizing radiation.

3.1.1 Experimental Generation of a ns Hole

We identify, through theory and experiment, a novel ionization channel that opens up only in the presence of an intense laser field. Experimentally we find that in the presence of a sufficiently intense IR laser and an extreme ultraviolet (XUV) field, the double ionization yield of Ar is enhanced by 50% compared to the case when the laser pulse arrives after the XUV pulse. Although Ar^{2+} can also be produced by sequential and nonsequential absorption of XUV and IR photons (shakeup and shake-off processes), the observed ratio of doubly to singly ionized argon is larger than can be theoretically explained by these processes alone. Therefore, we need to include a new double ionization pathway: IR laser-enabled Auger decay (LEAD), which is energetically forbidden without the presence of the IR field. Normally in a rare gas atom, Auger decay following the creation of an ns hole by an XUV photon is not energetically allowed. However, our theoretical predictions show that the laser-enabled Auger decay rates are even larger than the radiative decay rates for laser intensities above 10^{13} W/cm^2, and thus the inner-valence hole can be filled by the LEAD process

on few-femtosecond time scales. This novel decay channel is also quite general, representing a fundamentally new mechanism for generating ions and Auger electrons that must be considered in ultrafast x-ray experiments. It also provides a new route for controlling electron dynamics using ultrafast light fields.

Figure 3.1 (b) illustrates the possible single and double ionization channels in Ar. We consider three cases: the IR pulse precedes the XUV pulse (region I); the two pulses overlap in time (region II); and the IR pulse follows the XUV pulse (region III). Figure 3.1 (a) shows that the Ar^{2+} yield is negligible for region I, while the yield increases dramatically for positive time delays, peaking in region II when the XUV and IR pulses overlap. The enhancement of the Ar^{2+} yield in region III is due to field ionization of Ar^{+*} and Ar^{**} states excited by the XUV pulse, and due to the LEAD process. We note that without the IR pulse the $3p^{-1}$ and $3s^{-1}$ highly-excited Ar^{+} states radiatively decay on a nanosecond time-scale. The most interesting behavior, however, occurs in region II when the XUV and laser pulses overlap in time. The observed enhancement in the Ar^{2+} signal strongly suggests that the laser field modifies the mechanism for populating the Ar^{+*}/Ar^{**} states created after the absorption of a single XUV photon. There are two possible mechanisms for the observed enhanced Ar^{2+} yield in region II: first, the laser field can influence the shake-up and IR-ionization sequence by modifying, broadening, and shifting of the Ar^{+*} resonances [15, 53]; and second, the laser field can provide the additional energy required to open up a shake-off channel, which does not occur in region III (where the XUV pulse excites unperturbed Ar^{+*} states that are sequentially ionized by the IR pulse).

To investigate the physical origin of the Ar^{2+} signal we note that there are four possible ways to create Ar^{2+} in the presence of simultaneous IR and XUV (42 eV) fields: (a) IR assisted shake-off and shake-up processes in regions II and III, (b) knockout ionization processes, (c) single photon double excitation by the XUV pulse, followed by IR-induced double ionization, and (d) a new mechanism of IR-enabled Auger decay of an XUV-induced $3s$ hole.

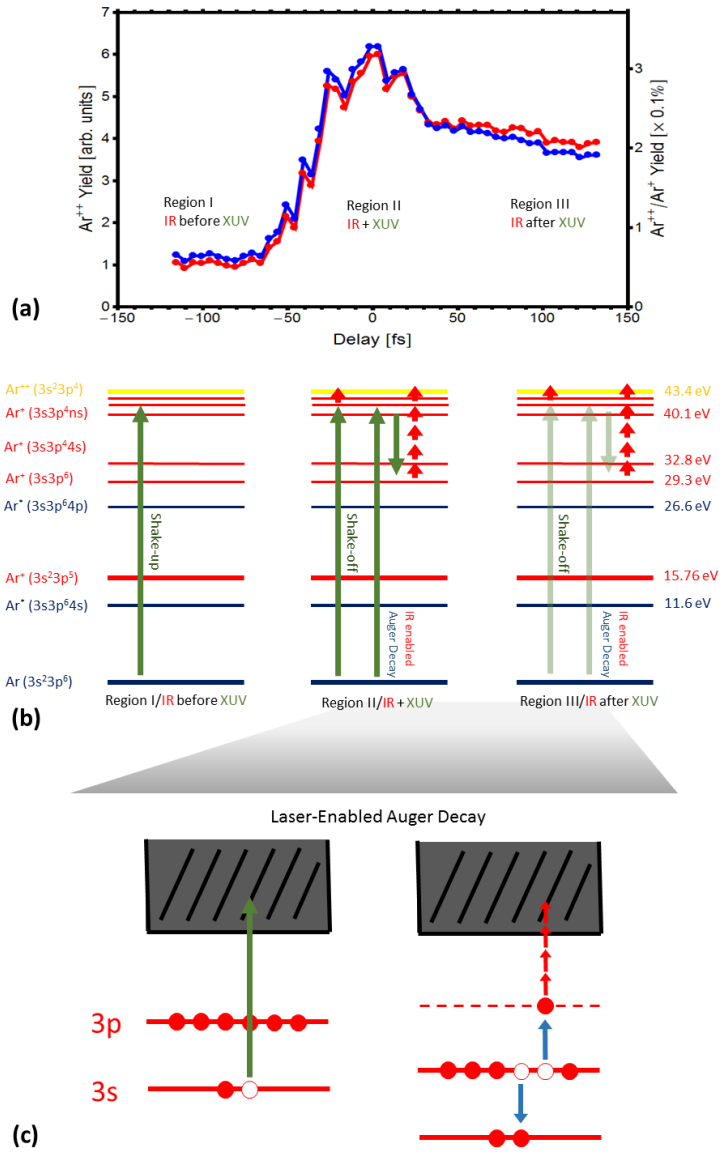

Figure 3.1: (a) Ar^{2+} and Ar^{2+}/Ar^{+} yields as a function of the XUV pump and IR probe delay. The three regions correspond to the different relative delays of the XUV and IR pulses. (b) Schematic diagram of double ionization pathways in different regions. In region II, the main double ionization channels are labeled as shake-off and IR-enabled Auger decay. In region I, since Auger decay is not energetically allowed, the XUV pulse creates Ar^{+} and Ar^{2+} states. These states, respectively, radiatively decay and autoionize, and do not contribute to the Ar^{2+} yield. In region III the IR pulse arrives after the XUV pulse, and doubly ionizes the Ar^{+} and Ar^{2+} states created by the XUV pulse, and opens up the LEAD channel. In region II the IR field enhances the Ar^{2+} yield by altering the atoms electronic structure, influencing thus the LEAD, shake-up or shake-off, and other allowed channels. (c) The laser-enabled Auger process is shown through the creation of a 3s hole with an XUV pulse and then ionization with additional IR energy. This process contributes to the double ionization yield in both regions II and III.

3.1.2 Theoretical Calculations

The double ionization probability of Ar through channels (a) and (b) depends on the excess energy available above the double ionization threshold of 43.5 eV in Ar [54]. Field ionization by the IR field provides this excess energy when Ar is exposed to a combined action of XUV and IR fields. Thus, to estimate the expected Ar^{2+}/Ar^{+} ratio from channels (a) and (b), we first calculate the photoelectron yields above and below the double ionization threshold. Second, we calculate the shake-up and shake-off ionization probabilities from the $3s$ and $3p$ orbitals. We do this by solving the time-dependent Schrödinger integral equation [55] by the split-operator method in the energy representation [56] to obtain the above-threshold ionization (ATI) distribution $dP(E)/dE$ from both $3s$ and $3p$ orbitals. The IR intensity used in the calculation was 5×10^{12} W/cm^2. The detailed numerical method can be found elsewhere [57]. The double ionization yield depends on the ATI spectra with total energy higher than the double ionization threshold, according to

$$P^{++} = \int_{E>E_c} \frac{dP(E)}{dE} dE \tag{3.1}$$

where E is the ATI electron energy and E_c is the minimum energy needed to open the double ionization channel. We find that the ATI electrons above the E_c threshold contain 30% of the total ATI yield. On the other hand, the total shake-off (including shake-up) probability after removing a $3p$ or $3s$ electron can be calculated by using the sudden approximation

$$P = (1 - \langle \tilde{\psi}_{3p} | \psi_{3p} \rangle^2) n_{occ} \tag{3.2}$$

where $\tilde{\psi}_{3p}$ and ψ_{3p} are the $3p$ wave functions of Ar and Ar^{+} calculated by utilizing density functional theory with the self-interaction correction method [58], while n_{occ} is the number of the valence Ar^{+} electrons. We find the shake-up or shake-off probability to be $P = 4\%$, after the sudden removal of $3p$ and $3s$ electrons. By multiplying this probability with the double ionization photoelectron yield calculated above, we find that the upper limit for the shake-off yield is 1.2%. However, the measured fractional Ar^{2+} yield shown in Figure 3.1 (a) peaks at 4% near time zero, which means that channels (c) and (d) must also contribute significantly to double ionization.

In the case of process (c)-single-photon double excitation to Ar^{**} by the XUV pulse followed by IR-induced double ionizationthe first step of creating Ar^{**} has been studied using synchrotron light in the energy range considered here [59, 60]. In the presence of an additional IR field, the XUV-induced Ar^{**} states can be promoted into the double ionization continuum, thus contributing to the total Ar^{2+} yield. Because doubly excited states in general autoionize on femtosecond time scales, their signature would be seen as a decay in the Ar^{2+} yield at long time delays, as indeed seen in region III of Figure 3.1(a). Calculating exactly how the IR laser influences the creation of doubly excited states in region II still remains a theoretical challenge.

Route (d), which represents a novel IR-enabled Auger decay route for the XUV-induced $3s$ hole, as shown in Figure 3.1(b), is also possible. After the creation of a $3s$ hole with the XUV pulse, the $3p$-$3s$ Auger decay is energetically forbidden. However, this double ionization channel can be opened up in the presence of a sufficiently high IR laser field. In the case of Ar, an Auger-induced 3p electron needs 14.8 eV of extra energy to reach the double ionization continuum. Assuming that the wave functions of the atomic ion with a subshell hole (N − 1 electron system), the doubly ionized ion core (N − 2 electron system), and the Auger electron are $\Psi_h(N-1)$, $\Psi_c(N-2)$, and ψ_a with the corresponding Hamiltonians $H_h(N-1)$, $H_c(N-2)$, and h_a, respectively, we can write the time evolution of the Auger electron wave function as

$$\psi_a(\mathbf{r},t) = -i\int_{-\infty}^{t} e^{-i\int_{\tau}^{t} h_a(t')dt'} e^{-i(E_h-E_c)\tau} F(\mathbf{r})d\tau \tag{3.3}$$

Here E_h and E_c are the total energies of the $\Psi_h(N-1)$ and $\Psi_c(N-2)$ states, respectively. To derive the above equation, we assume that the IR laser only affects the Auger electron and that it does not perturb the occupied orbitals in $\Psi_h(N-1)$ and $\Psi_c(N-2)$. Since the Auger process is a two-electron process, $F(\mathbf{r})$ is evaluated as

$$F(\mathbf{r}) = \sum_{i=1}^{N-2} \langle \Psi_c(N-2)| \frac{1}{|\mathbf{r}-\mathbf{r}_i|} |\Psi_h(N-1)\rangle \tag{3.4}$$

which does not depend on the IR field. The Hamiltonian of the Auger electron in the IR

laser is written as

$$h_a(t) = -\frac{\nabla^2}{2} + V_{eff}(r) - zE(t) \tag{3.5}$$

where $V_{eff}(r)$ is the model potential [61] of the atomic ions, z is the electron coordinate along the IR polarization direction, and $E(t)$ is the IR field strength. For Ar, $|\Psi_h(N-1)\rangle$ can be written as $|3s3p^6\,{}^2S\rangle$, which can be represented as [62]

$$\begin{aligned} |\Psi_h(N-1)\rangle =& \frac{1}{\sqrt{15}}|3s(3p^4\,{}^1S)3p^2\,{}^2S\rangle \\ &+ \frac{1}{\sqrt{3}}|3s(3p^4\,{}^1D)3p^2\,{}^2S\rangle \\ &+ \sqrt{\frac{3}{5}}|3s(3p^4\,{}^3P)3p^2\,{}^2S\rangle \end{aligned} \tag{3.6}$$

$|\Psi_c(N-2)\rangle$ is $|3s^2 3p^4\,{}^1S\rangle$ or $|3s^2 3p^4\,{}^1D\rangle$. The last term in Equation 3.6 does not contribute to the LEAD due to conservation of the angular momentum and parity. The final doubly charged ions created by the LEAD can be in the ^{1}S (the upper limit is 1/15) or ^{1}D (the upper limit is 1/3) states, limiting the total double ionization yield to be 40% of the hole population.

By defining a radial function $f(r)$ as

$$f(r) = \int_0^\infty R_{3s}(r_1)\frac{r_<}{r_>^2}R_{3p}(r_1)R_{3p}(r)r_1^2 dr_1 \tag{3.7}$$

where $r_<$ ($r_>$) is the smaller (larger) one of the r and r_1, and R_{3s} and R_{3p} being the radial wave functions of $3s$ and $3p$ states, we obtain

$$F(\mathbf{r}) = \begin{cases} -\frac{1}{\sqrt{3}}f(r)Y_{00}(\hat{\mathbf{r}}) & \text{for } ^1\text{S} \\ -\sqrt{\frac{2}{15}}f(r)Y_{2M}(\hat{\mathbf{r}}) & \text{for } ^1\text{D} \end{cases} \tag{3.8}$$

^{1}S (^{1}D) stands for the final state of the doubly ionized species. Using the expression for $F(\mathbf{r})$, we calculate the Auger election wave function from Equation 3.3 numerically [56]. Again, the single electron wave functions of the occupied orbitals in $|\Psi_h(N-1)\rangle$ and $|\Psi_c(N-2)\rangle$ are calculated from the density functional theory with the self-interaction correction method [58].

To speed the convergence of the simulation, we add a temporal window function $e^{-\tau^2/T^2}$ in Equation 3.3. Thus, after a long propagation time we can expand ψ_a with a set of wavefunctions as

$$\psi_a(\mathbf{r}, t \to \infty) = \int C(\epsilon)\psi_\epsilon(\mathbf{r})d\epsilon \tag{3.9}$$

where $\psi_\epsilon(\mathbf{r})$ is the laser-field-free atomic continuum wave function, and ϵ is the Auger electron energy [55]. The energy distribution of the emitted electron can be expressed as

$$\frac{dP(\epsilon)}{d\epsilon} = |C(\epsilon)|^2 \tag{3.10}$$

and the LEAD rate can be written as

$$R_a = \frac{\sqrt{2\pi}}{T}\int_0^\infty \frac{dP(\epsilon)}{d\epsilon}d\epsilon \tag{3.11}$$

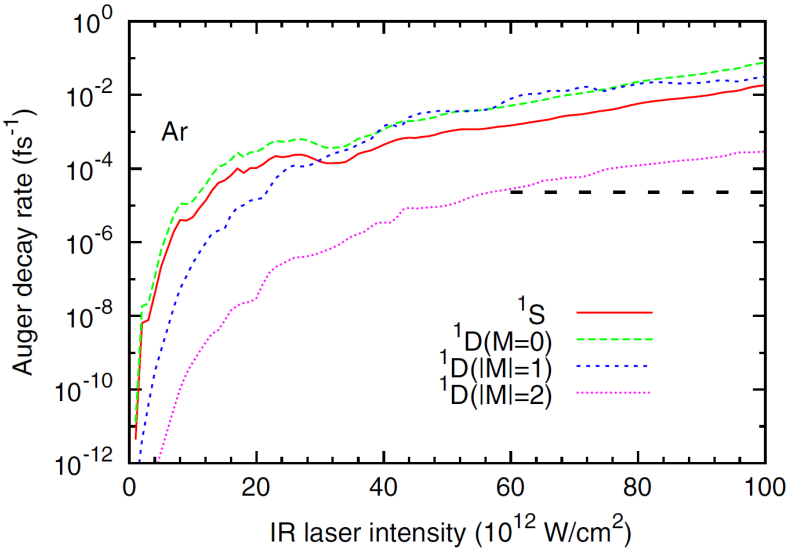

Figure 3.2: Calculated IR laser-enabled Auger decay rates for Ar. At lower laser intensities, the leading decay channels are the ^{1}S and ^{1}D (M=0) states. As the IR laser intensity increases, the contribution from the ^{1}D (M=0) state is larger than that from the ^{1}S state. Radiative $3p$-$3s$ decay is represented by the dashed line.

The $\sqrt{2\pi}/T$ term is introduced because we added a temporal window function. If there is no IR laser field present, Equation 3.11 reduces to the standard expression for the Auger decay rate. Because of the energy deficiency, the Auger decay rate goes to zero for an inner-valence $3s$ vacancy of Ar without the presence of the IR field.

3.1.3 Calculation of the LEAD Rate

Based on the above approach, we can now calculate the LEAD rate in Ar. From Figure 3.2 we see that laser intensities of $\approx 10^{13}$ W/cm^2 can indeed open up a new laser-enabled Auger decay channel, with a rate of 4.3×10^{-4} fs^{-1}, which is comparable or even larger than the radiative decay rate of the $3p$ electron. Thus, the contribution to the Ar^{2+} yield from the LEAD channel is comparable to contributions from the shake-off channel, and must therefore contribute to the total Ar^{2+} yield.

New ionization pathways are possible when matter is irradiated by intense laser and x-ray fields. In this work, to explain the yield of Ar^{2+} ions in the presence of combined IR and XUV fields, we needed to include a new double ionization pathway: IR laser-enabled Auger decay, which is energetically forbidden without the presence of the IR field. Our theoretical predictions showed that LEAD rates are even larger than the radiative decay rates for laser intensities above 10^{13} W/cm^2, and that the $3s$ hole can be filled by the LEAD process on few-femtosecond time scales. This novel decay channel is also quite general, representing a fundamentally new mechanism for generating doubly charged ion cores, ionic Rydberg states, and Auger electrons. It also provides a new scheme for controlling electron dynamics in atoms, molecules, and solids using IR fields.

3.2 Ar^+ vs. Ar^{2+} Control

In a different experiment, a spectrally tailored high harmonic beam, with both VUV and XUV harmonics, was used to coherently excite Rydberg states of argon below the single and double ionization thresholds by means of the 7th-9th, and 25th-27th harmonics of the driving IR laser field. Figure 3.4 shows the set-up for reflecting both low and high harmonics in a non-blueshifted

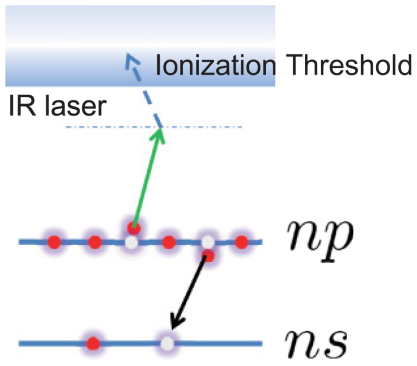

Figure 3.3: Schematic diagram of IR-enabled Auger decay in a rare-gas atom.

(phase matched for a fundamental energy of 1.61 eV) and blueshifted case (phase matched for a fundamental energy of 1.69 eV). By tuning the pressure of the harmonic generation medium we can blue-shift the central energy of the harmonic combs in such a way that the VUV harmonics (i.e. 7th and 9th) are either nonresonant (depicted in red) or resonant (depicted in blue) with the Ar* Rydberg states. At the same time, the multilayer mirror, coated to reflect photons with energies around 42 eV, can select either one dominant (i.e. 25th) or two dominant XUV harmonics (25th and 27th) that can directly double ionize and excite Ar^+ slightly below the double ionization threshold. By adding a weak IR field ($\sim 3 \times 10^{11}$ W/cm^2), delayed relative to the harmonic beam, we can couple the states excited by the VUV/XUV beam directly into the single/double ionization continuum and control the phases of the interfering electron wave packets, which in turn results in the Ar^+ and Ar^{2+} yield modulation.

In Figure 3.4 inset part (a), a theoretical simulation shows the total Ar^+ yield when the resonant and nonresonant VUV beam acts as a pump, and the IR field acts as a probe. The oscillation of resonant and nonresonant cases are dephased from one another. Since in this case only one IR field is present, only the quantum interferences play a role in the total yield modulation. By keeping the IR probe pulse the same, and by adding a second, weak IR pulse phase-locked to the VUV pulse, shown in inset (b) in Figure 3.4, we start mixing optical and quantum interferences as the probe IR beam is delayed. The optical interferences in between the two IR pulses have the

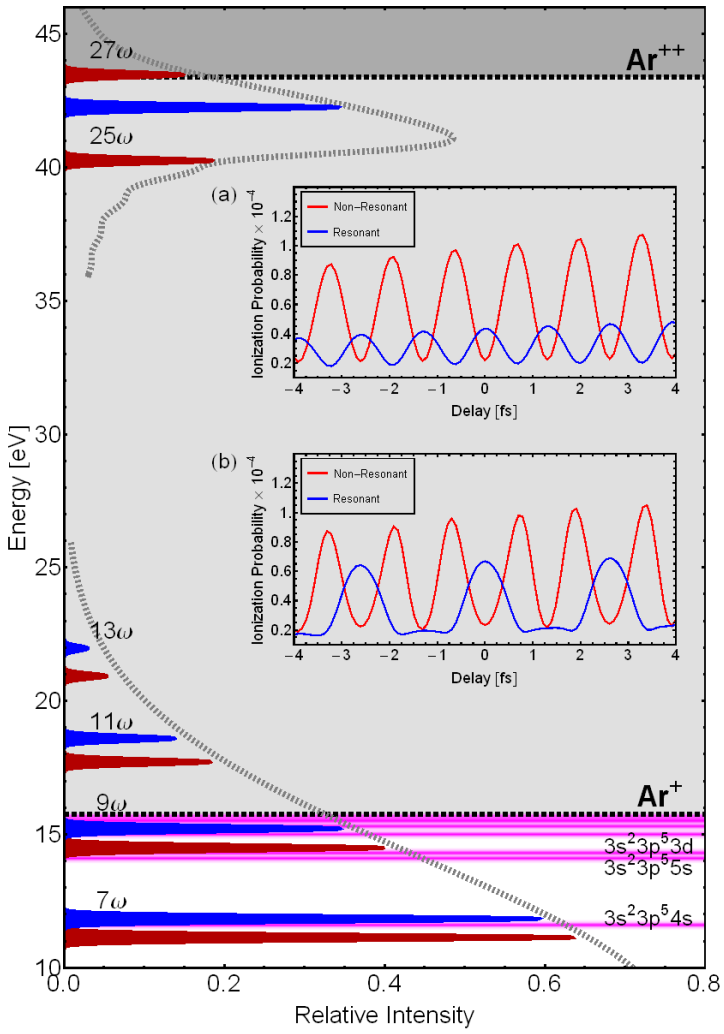

Figure 3.4: Schematic of the low (VUV) and high (XUV) harmonic reflectivity curves and ionization levels for Ar. The inset part (a) shows the simulated Ar^+ yield when the resonant and nonresonant VUV beam acts as a pump, and the IR field acts as a probe. The oscillating yield occurs due to quantum interferences. The inset part (b) includes a second IR pulse phase-locked to the VUV pulse in the simulation, therefore including optical and quantum interferences as the probe IR beam is delayed.

same phases in both resonant and nonresonant cases, while the phase of the quantum interferences changes as we tune the VUV harmonics in and out of the Ar^* resonances. From Figure 3.4(b), we see that when the optical and quantum interferences are in phase (i.e. the resonant case), the total Ar^+ yield oscillates with a full cycle periodicity. In the nonresonant case the quantum and the optical interferences are off phase, which results in the total yield modulation close to half a

cycle oscillation.

Figure 3.5 directly demonstrates tuning the VUV harmonic frequencies over a resonance. Figure 3.5 parts (a),(c) show the experimental Ar^+ yield as a function of IR delay where negative delays refer to the IR pulse arriving before the XUV pulse train. In Figure 3.5(a) the harmonics are minimally blue shifted (nonresonant case). In part (c) the harmonics are blue-shifted such that the 9th harmonic resonantly excites the atom resulting in a clear change in the femtosecond scale yield. In both cases the IR probe pulse does not have significant intensity to ionize Ar without interacting with the XUV pulse. Parts (b) and (d) show the theoretical simulations for the same energies. They are in excellent agreement. The Figure shows both the cycle-averaged behavior as well as an inset showing sub-optical cycle resolution. We note that in part (a) the single ion yield oscillates with a half-cycle periodicity (or a period of 1.3 fs) whereas in part (c) this changes to full-cycle (or a period of 2.6 fs).

Figure 3.6 shows the photoelectron data for the same non-blueshifted and blueshifted cases described for Figure 3.5 along with the theoretical simulations. Again we note agreement between experiment and the simulation. In particular the Figure highlights the difference between half optical cycle oscillation (parts (a) and (b)) and full optical cycle oscillation (parts (c) and (d)).

Figure 3.7 shows the photoelectron energies for electrons collected in coincidence with Ar^{2+} in the resonant case. Although the photoion-photoelectron count rate was low for this experiment it demonstrates our ability to simultaneously probe the photoelectrons from the double ionization threshold as well as the single ionization.

3.3 Extension of LEAD to other Noble Gases

To find further evidence of LEAD processes, we performed experiments on the double ionization of Ar and Xe atoms using time-resolved femtosecond IR and 36 eV XUV pulses. For argon, 36 eV is well below the double ionization threshold, and several possible double ionization channels open up in the presence of an IR pulse as intense as 7×10^{12} W/cm^2 [43]. For xenon, the 36 eV photon energy is just above the double ionization threshold and the number of double ionization

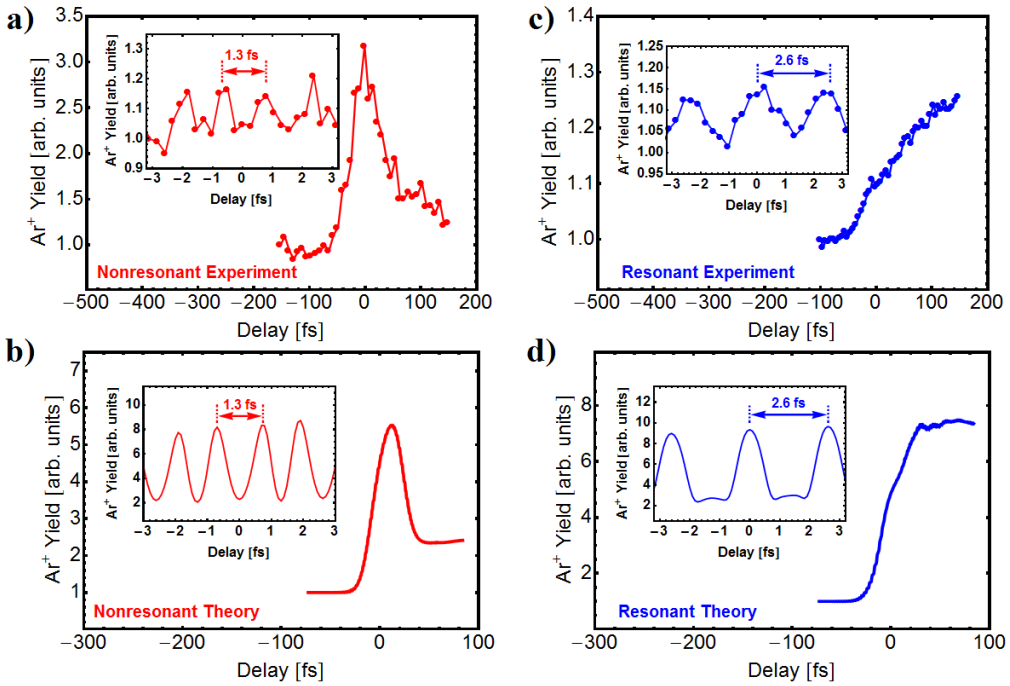

Figure 3.5: Single ionization yield (a) Nonresonant experiment (b) Nonresonant theory; both show half cycle oscillations, (c) Resonant experiment (d) Resonant theory; both show full cycle oscillations. The nonresonant theory and experiment uses harmonics phase matched to a fundamental of 1.61 eV. The resonant theory and experiment uses harmonics phase matched to a fundamental of 1.69 eV.

channels significantly reduces compared with the ar case. For example, Xe^{**} ($5p^4$) and Xe^{+*} ($5p^5$) states are not possible, as was the case in Ar. In Xe, a 36 eV XUV photon can create a $5s$ hole and leave the singly charged Xe in the ground state after a $5p$-$5s$ radiative relaxation, or leave $5s$ Xe in a highly excited state as shown in 3.8 lower panel. In the former case, the IR pulse can ionize Xe^+ through the LEAD process with rates several orders of magnitude larger than the radiative $5p$-$5s$ decay as shown in Figure 3.8 upper panel. The ability to enable Auger decay with rates significantly higher than radiative decay opens up possibilities for controlling electron-electron interactions in atoms and molecules. Using part of the laser output, high harmonics are generated in Ar gas and then refocused multilayer XUV mirrors which reflect photon energies around 36 eV. A 200 nm thick Al filter is inserted in the XUV beam to attenuate the driving IR pulses reflected from the XUV mirrors. This results in higher reflectivity of lower harmonics. In this case, the 13th and 15th

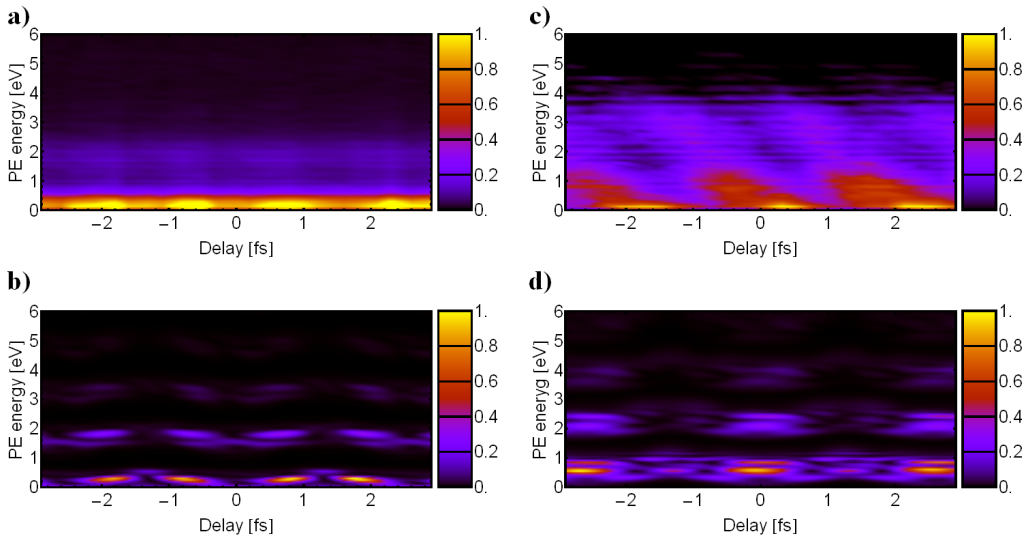

Figure 3.6: Photoelectron energies vs. delay (a) Nonresonant experiment (b) Nonresonant theory; both show half cycle oscillations, (c) Resonant experiment (d) Resonant theory; both show full cycle oscillations. The nonresonant theory and experiment uses harmonics phase matched to a fundamental of 1.61 eV. The resonant theory and experiment uses harmonics phase matched to a fundamental of 1.69 eV.

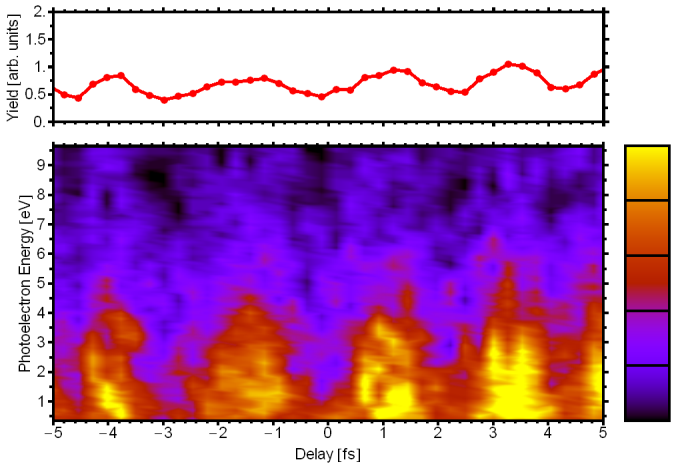

Figure 3.7: Photoelectron energies vs. delay filtered in coincidence with Ar^{2+}. The photoelectrons also show full optical cycle oscillations.

harmonics are reflected from the XUV optics as seen in the Ar photoelectron spectrum shown in Figure 3.9 (lower panel). The probing IR has an intensity of approximately 7×10^{12} W/cm^2.

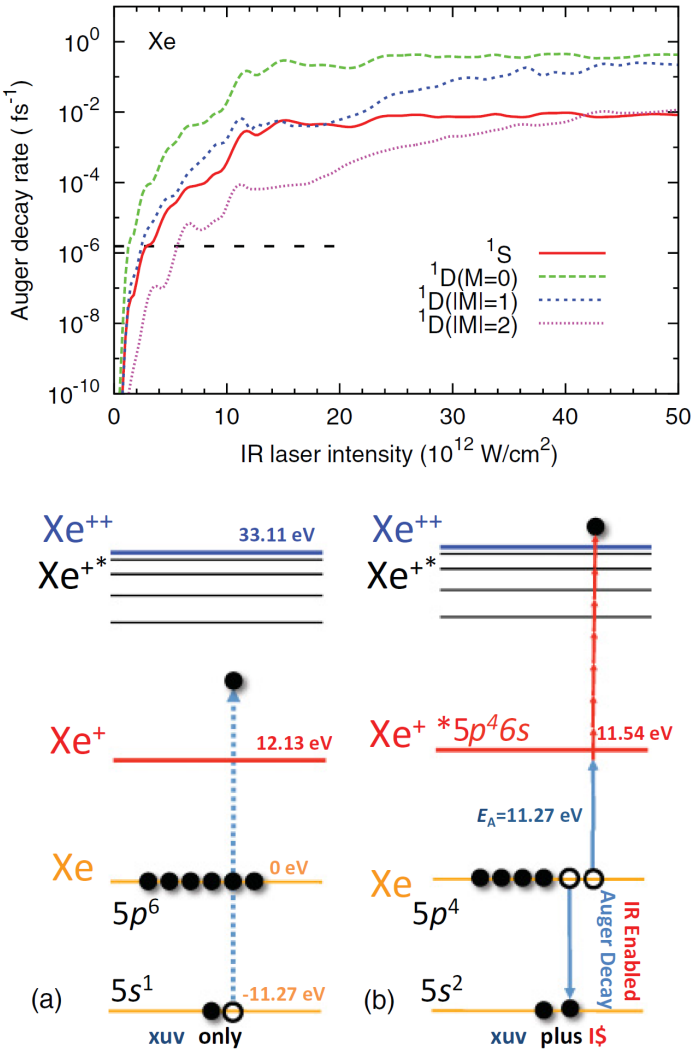

Figure 3.8: Upper: IR-enabled Auger decay rates for Xe, with Xe^{2+} ions in the ^{1}S state (solid line) and ^{1}D states (dashed lines). The horizontal dashed line indicates the radiative decay rate of the hole. Lower: (a) Xe energy diagram for the lowest single and double ionization thresholds with a 5s electron ionized by an XUV pulse. (b)A 5p electron can be ejected to an Xe^{+*} Rydberg orbit or the Xe^{2+} continuum through the LEAD process after a respective absorption of at least one or seven IR photons.

3.3.1 Argon and Xenon Experimental Results

Figure 3.9, upper and lower panels, respectively, shows the argon double ionization yield as well as the ratios of Ar^{2+}/Ar^+ yields, and a photoelectron yield, taken in coincidence with Ar^+

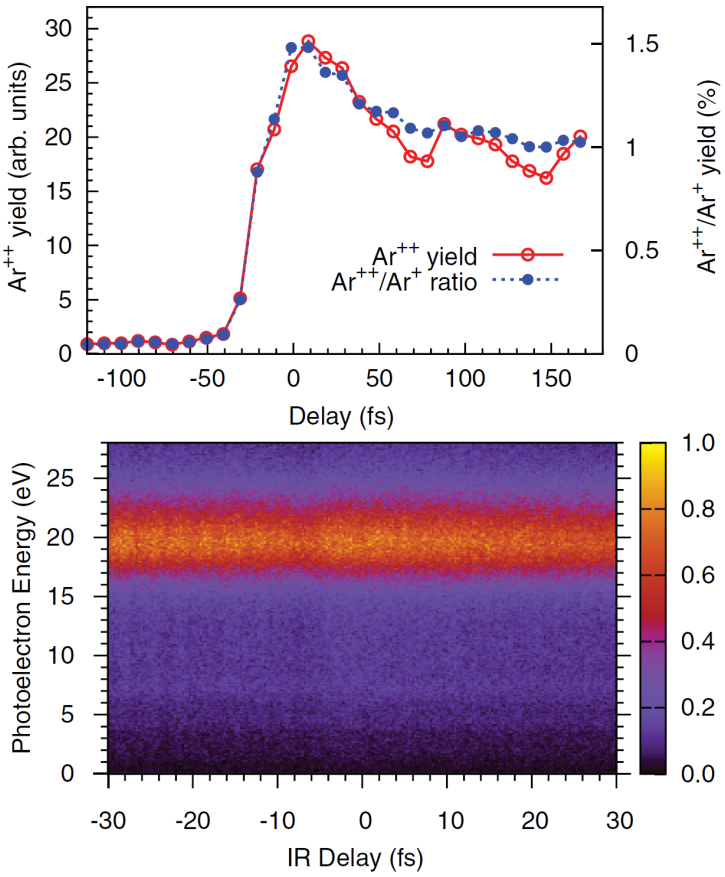

Figure 3.9: Ar^{2+} and Ar^{2+}/Ar^{+} yields as a function of the delay between the XUV and IR pulses (upper panel). The photoelectron spectra taken in coincidence with Ar^{+} ions in the overlap region (lower panel).

atoms, as a function of the XUV-IR relative delay. Negative delays represent the case when the IR pulse precedes the XUV pulse, while positive delays present the case when the IR pulse arrives after the XUV pulse. The two pulses overlap temporally for the delays between -30 and +30 fs (overlap region). Figure 3.9, upper panel, shows that the moderate IR field enhances the Ar^{2+} yield by roughly 30 times in the overlap region, while the Ar^{2+}/Ar^{+} ratio maximizes at about 1.6%. The photoelectron yield taken in coincidence with Ar^{+} ions (Figure 3.9, lower panel) shows a peak around 20 eV corresponding to photoionization of a $3p$ electron by the 36 eV XUV photon. If the XUV pulse ionizes a $3s$ electron (binding energy 29.2 eV), we expect to see a photoelectron signal

around 6.2 eV, after subtracting the ponderomotive potential of about 500 meV. The photoelectron yield in that region shows two lines at 4.2 and 7.4 eV, corresponding to a $3p$ electron ionized by the 13th and 15th harmonics leaking though the XUV reflective optics. Since the 36 eV XUV photon is 7.5 eV below the double ionization threshold, the Ar^{2+} enhancement in the overlap region could come from coupling of the Ar^{+*} and Ar^{**} 3p states into the double ionization continuum by the IR pulse. Single-photon double ionization is a resonant process and the Ar^{2+} yield of IR field ionization of Ar^{**} should be sensitive to the XUV energy. The pattern of the Ar^{2+}/Ar^{+} yield obtained by the 36 eV XUV photon is similar to the one obtained by the 42 eV XUV source [43]. Therefore, the additional double ionization yield enhancement also comes from a LEAD process where the 36 eV photon ionizes a $3s$ electron, while the IR field couples an Auger $3p$ electron to the double ionization continuum.

Figure 3.10, upper and lower panels, respectively, shows a Xe double ionization yield as well as the ratios of Xe^{2+}/Xe^{+} yields, and the photoelectron yield, as a function of XUV-IR relative delay. The data was taken by using similar XUV and IR parameters as for the Ar data shown in Figure 3.9. By doubly ionizing Xe using a 36 eV XUV pulse, we make sure that the highest double ionization threshold ($^1D_2$ 35.5 eV) is still below the XUV photon energy. By doing so, we eliminate the double ionization contribution from the Xe^{+*}/Xe^{**} 5p states ionized by the IR pulse. This results in a significantly smaller enhancement of the Xe^{2+} yield in the overlap region, compared with the Ar^{2+} enhancement (30:1.7 in favor of Ar), and in a higher Xe^{2+}/Xe^{+} ratio (4:1.6 in favor of Xe). The flat Xe^{2+} yield for positive IR delays shows that short-lived, autoionizing double excited states probably do not play a significant role in this case. From the photoelectron spectra [Figure 3.10 (lower panel)], we notice that the lower harmonics (13th and 15th) contribute more significantly to the Xe^{+} yield compared with the Ar case. Thus, the Xe^{2+}/Xe^{+} yield coming from the 36 eV photon channel is probably even higher than shown in Figure 3.10 (upper panel). In the case of Xe, 7×10^{12} W/cm^2 IR intensity can ionize Xe, as seen at 0.2 eV electron energy at both positive and negative delays in Figure 3.10. By setting up the experiment in this way, we make sure that the LEAD process is experimentally possible, since the Xe LEAD deficiency is

only 9.80 eV. However, even though we were able to decrease the number of the IR-enabled double ionization channels by using an XUV photon energy just above the double ionization threshold, isolating unambiguously the LEAD process remains an experimental challenge.

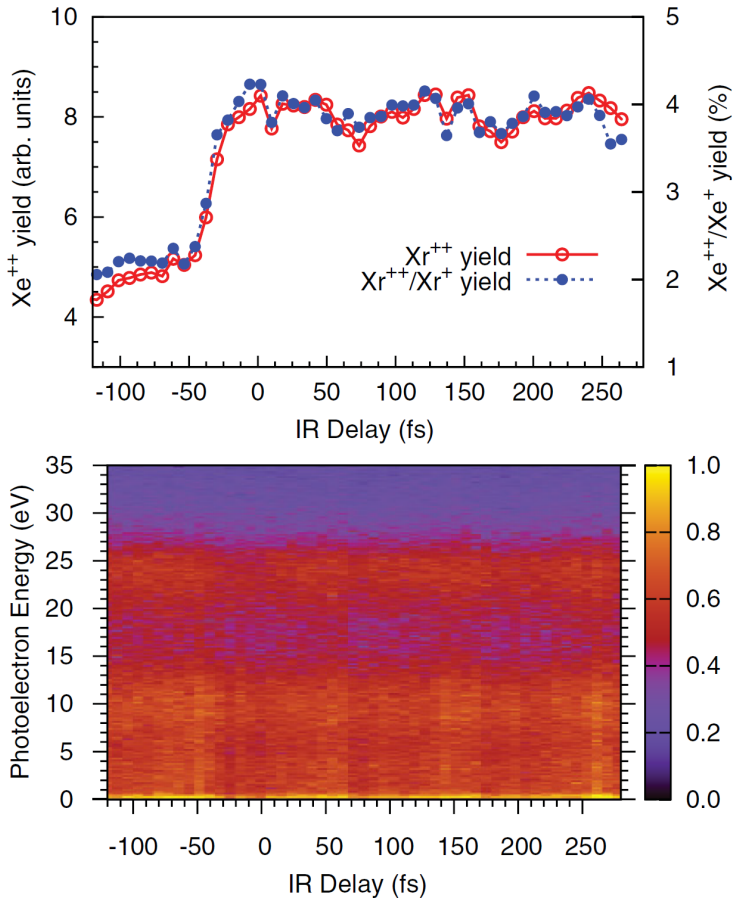

Figure 3.10: Xe^{2+} and Xe^{2+}/Xe^{+} yields as a function of the delay between the XUV and IR pulses (upper panel). Photoelectron spectra taken simultaneously with the Xe ions (lower panel).

3.3.2 Attosecond Time Scale Dynamics

In addition to exploring femtosecond delays, we performed a time-resolved experiment with attosecond resolution in the overlap region. Figure 3.11 shows the Xe^{2+} versus Xe^{+} yield as a function of the XUV-IR delays. In this experiment, in addition to the 36 eV XUV harmonic we

allow the lower harmonics (lower than the Xe ionization potential) to populate neutral Xe^* states. We did this by taking the Al filter out of the XUV beam. By doing this, we lock a weak IR pulse (3×10^{11} W/cm^2) to the XUV pulse in the time domain, and let both beams copropagate. The inset of Figure 3.11 shows the XUV and IR pulses in the time domain. As we delay the probe IR beam (7×10^{12} W/cm^2) on an attosecond time scale relative to the XUV–IR pump beam, we change the total intensity the atom sees at the instant of the strobe XUV pulse [15, 63]. By doing so we control the Xe^{2+}/Xe^{+} yields both by modulating the total IR intensity and by interfering the electron wave packets. The phase difference of about a half optical cycle is telling us that different processes are responsible for the coherent control of the single and double ionization Xe yields. The interference of the two electronic wave packets with the final energy of the 8th harmonic (7th + IR and 9th − IR) are responsible for the modulation of the Xe^{+} yield, while the modulation of the Xe^{2+} yield can occur through several different channels. The LEAD channel is very sensitive to the IR intensity as shown in Figure 3.8, but also it is possible that the phase of the XUV and IR pulses plays a role. Thus, we are not surprised that the Xe^{+} and Xe^{2+} yields get modulated at different phases, and with different amplitudes. We expect that the LEAD process would depend on the time delay between the attosecond XUV pulse (creation of the hole) and the probing IR field (induced Auger decay). Thus we can both induce Auger decay by employing an IR laser field and control the process by tuning the time delay between the two pulses.

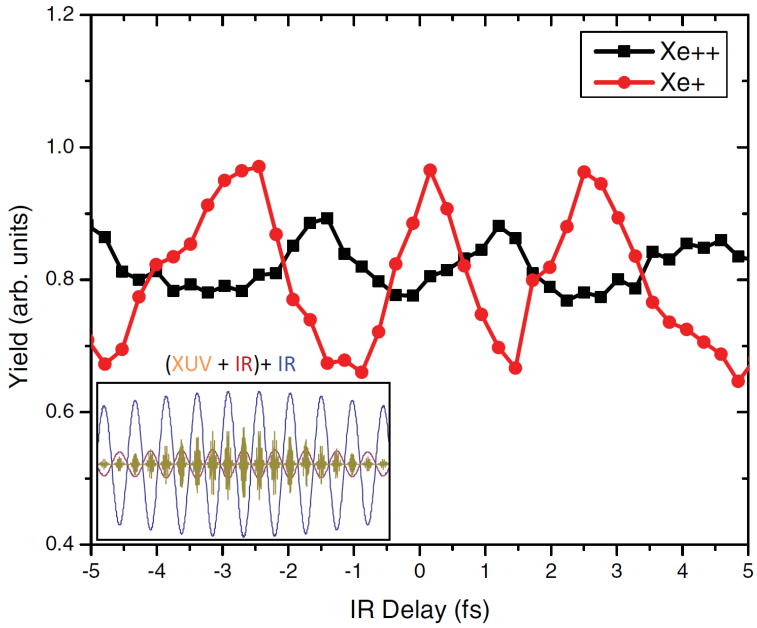

Figure 3.11: Xe^{+} and Xe^{2+} yields as a function of the XUV-IR pump and IR probe pulses. The XUV and IR pulses in the time domain are shown in the inset.

Chapter 4

Helium[1]

High-order harmonic generation (HHG) is a unique source of ultrashort-pulse light spanning the ultraviolet and soft x-ray regions, that is ideal for initiating and probing fast dynamics in atoms, molecules, and materials [47, 64–67]. Atoms irradiated with combined femtosecond laser and extreme ultraviolet (XUV) fields ionize through multiphoton processes, even when the energy of the XUV photon is below the ionization potential. However, in the presence of two different XUV photons and an intense laser field, it is possible to induce full electromagnetic transparency. Taking helium as an example, the laser field modifies its electronic structure, while the presence of two different XUV photons and the laser field leads to two distinct ionization pathways that can interfere destructively. This Chapter discusses a new approach for coherent control in a regime of highly excited states and strong optical fields.

4.1 Ionization pathway interference

Because the high harmonic field is perfectly synchronized to the generating laser field, complex reaction pathways relevant to radiation physics and chemistry can be probed [14, 68, 69]. In such highly excited processes, the laser field plays a crucial role in initiating, interrupting, or probing a reaction. However, the full influence of the laser field on highly excited reaction pathways is still being uncovered [70, 71], despite a wealth of theory and experiments exploring these processes. For example, calculations that model how dynamics are probed by HHG generally ignore the dynamic

[1] The results of this chapter are in part based on "P. Ranitovic, X. M. Tong, C. W. Hogle, X. Zhou, Y. Liu, N. Toshima, M. M. Murnane, and H. C. Kapteyn, Phys. Rev. Lett. **106**, 193008 (2011)" [63].

modification of the electronic structure of the atom or molecule by the laser field itself. Moreover, although helium is fully accessible to state-of-the-art theoretical calculations, even a simple two-color ionization process has to date proven to be far from simple to understand [15, 34, 57, 72–74].

4.1.1 Two-Color Multiphoton Processes

We study one of the simplest multiphoton processes: two-color multiphoton ionization of helium in combined infrared (IR) laser and extreme ultraviolet (XUV) high harmonic fields in a regime where two different ionization pathways can interfere coherently: 13th + 3ω and 11th + 5ω. We show both theoretically and experimentally that this two-color multiphoton ionization process can be viewed intuitively as a double-slit interference experiment in the frequency domain, and that ionization can be turned on or off by manipulating the two interfering pathways and shown in Figure 4.1. In addition to participating in the multiphoton absorption process, the strong IR field also alters the He excited state electronic structure by Floquet state (or dressing state), resulting in energy sidebands [57]. This allows us to adjust the position, amplitude and phase of the two multiphoton ionization channels, by tuning the XUV fields to the laser-dressed He $2p$ absorption resonance. Most importantly, by analyzing the multiphoton ionization process in the frequency domain, we develop an intuitive understanding of strong field two-color ionization to show, for the first time, that full laser-induced XUV electromagnetic transparency in He is possible. In the two-photon absorption schemes widely used for coherent control using visible laser fields [75–81], the phase of a weak, nonperturbative IR pulse can control absorption through interfering two-photon transitions. A multicolor, multiphoton XUV + IR ionization process is similar in some respects, except that in this case, the final state is in the continuum. Moreover, we show that a strong IR laser field can play multiple roles in a multicolor, multiphoton, XUV + IR ionization process, as is illustrated schematically in Figure 4.1. Specifically, by coherently populating laser-dressed excited states of He with the two tunable XUV harmonics (11th and 13th), and simultaneously using the same IR laser to couple the excited states to the continuum with equal amplitudes but with opposite phases, it is possible to make a He atom fully transparent to multiphoton XUV +

IR ionization. The phases of the two interfering channels are controlled by introducing suboptical cycle delays between the XUV and IR pulses, while the amplitudes are controlled by using the IR field to modulate the electronic structure of the He atom, thus changing the absorption cross sections of the two XUV harmonics through ac and dc Stark shifts that move and broaden the atomic resonances [15].

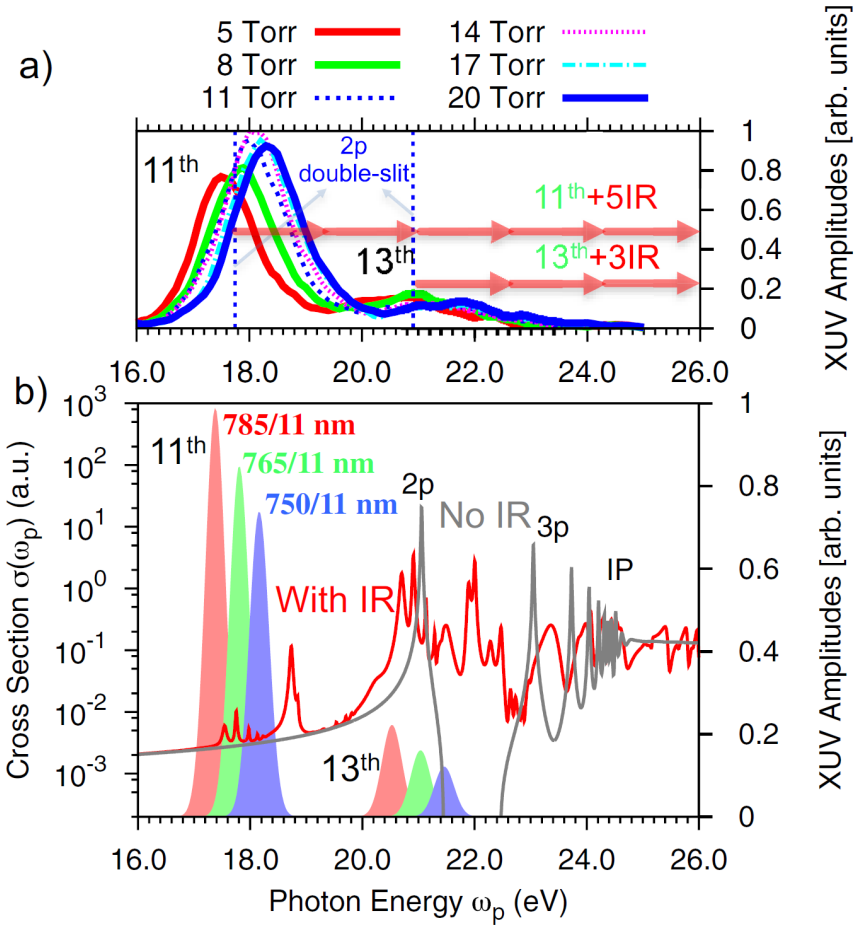

Figure 4.1: (a) Tuning of the harmonics in the frequency domain into the IR-created $2p$ double slit by varying the phase-matching conditions in a xenon-filled waveguide. The dashed vertical lines represent the calculated sidebands of the dressed Floquet $2p$ state of He. The two interfering quantum pathways are 11th + 5ω and 13th + 3ω. (b) Calculated He excitation cross section, with and without the presence of an IR field of intensity 4×10^{12} W/cm^2. The relative amplitudes of the harmonics are shown on the right axis. By changing the absorption cross section of He using the IR laser field, the amplitudes of the two interfering quantum pathways are controlled.

We note that the modulation of the He^+ ionization yield, when irradiated by a combined laser and comb of XUV harmonic fields, can also be explained as a time-domain process resulting from interferences between transitions to many different states [72]. This time-domain picture is useful for attosecond phenomena, whereas the frequency domain approach presented here is best suited for understanding how to coherently control highly excited processes, including for example, how to induce XUV transparency in atoms.

For this experiment, high harmonics are generated in Xe gas and then refocused into a the effusive gas jet seeded with helium. using a pair of multilayer XUV mirrors which reflect photon energies up to ∼22 eV. A 100 nm thick Al filter is inserted in the XUV beam to attenuate the driving IR pulses reflected from the XUV mirrors, and to eliminate harmonics lower than the 11th order. The amplitudes of the harmonics can be controlled using different combinations of XUV mirror coatings, while the exact energies of the harmonics can be continuously tuned by the phase-matching conditions via pressure tuning of Xe. Figure 4.1(a) shows that we can adjust the relative amplitudes of the XUV harmonics to be 4:1 in favor of the 11th harmonic, and change the phase-matching conditions in the waveguide to continuously drive the energy of the 13th harmonic across the $2p$ resonance in He. Another part of the laser beam is temporally and spatially recombined with the XUV beam in a collinear fashion, and focused onto the He target at a laser intensity of $\approx 4 \times 10^{12}$ W/cm^2. The XUV pulse duration was approximated to be 10 fs.

4.1.2 Theoretical Calculations

To predict the amplitude of a multicolor or multiphoton absorption or ionization channel and to compare with our experimental data, we calculate how a weak IR field modifies the absorption cross section of He (at the same IR intensity used in the present experiment), using an approach outlined in [53]. This calculation, shown in Figure 4.1(b), provides a photoabsorption map that helps us to compare the relative amplitudes of the two ionization channels. In general the intuitive picture of how an IR field broadens the resonances is confirmed by this calculation: the presence of the IR field shifts and broadens the He resonances, and modifies the electronic structure, leading

to a drop in the absorption cross section for the resonant XUV energies, and an increase in the absorption cross section between the resonances. We note that the width of the resonance represents the lifetime or the ionization rate of the dressed state, and the ionization probability is proportional to the absorption cross section. Therefore, in the following discussion, we will not distinguish absorption and ionization. We also see that the IR field modifies the electronic structure of He by inducing fine-structure features in the absorption cross section. For our coherent control of multiphoton XUV + IR ionization, the IR wavelength defines the width of the $2p$ double slit (two IR photons), while the IR intensity defines the position of the double slit in the frequency domain.

To experimentally observe how the IR field modifies the amplitude of the 13th + 3 IR photons ionization pathway as a function of the exact XUV photon energy, we monitor the time dependent He^+ yields on the femtosecond time scale, as the 13th harmonic is scanned across the $2p$ resonance. Figure 4.2(a) plots the He^+ yield for three different XUV 13th harmonic energies below (red curve), at (green curve), and above (blue curve) the He $2p$ resonance, as a function of IR laser time delay. The easiest way to see how the IR pulse modifies the absorption cross section of He is to tune the 13th harmonic into the He $2p$ resonance (green curve corresponding to a 765/13 = 58.8 nm XUV wavelength), and compare the ion yields for different time delays of the IR laser pulse. At zero time delay between the XUV and IR fields, absorption of the 13th harmonic occurs in the presence of the IR-modified resonance [Figure 4.1(b)]. This significantly decreases the He^+ yield compared with when the IR laser arrives well after the XUV field (positive IR delays). The inset of Figure 4.2(a) shows the experimentally observed and theoretically calculated photoelectron momenta at IR laser time delays of 200 fs. A g-wave angular distribution with 4 nodes in the positive p_x direction confirms that the XUV pulse excites only the $2p$ eigenstate of He, which is then sequentially promoted into the continuum by absorption of at least 3 IR laser photons.

4.2 Resonance Tuning

When the XUV photon energy is tuned above the $2p$ resonance (blue curve of Figure 4.2(a) corresponding to a 750/13 = 57.7 nm XUV wavelength), the He^+ yield reveals a slight asymme-

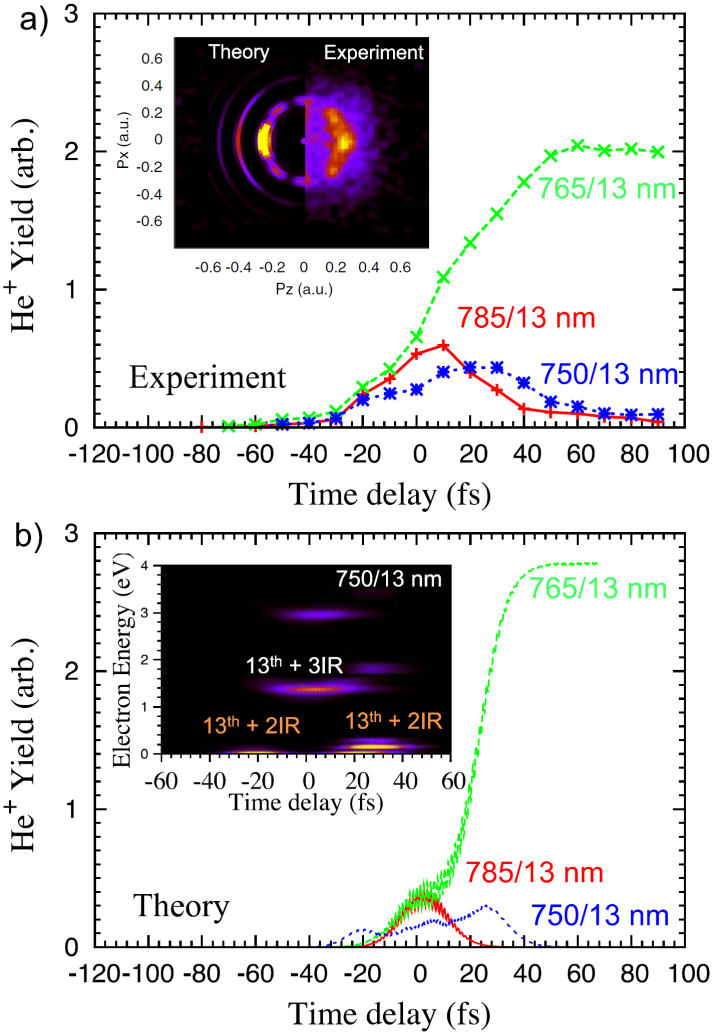

Figure 4.2: (a) He^+ yields for XUV and IR illumination (laser intensity of 4×10^{12} W/cm^2), in the case of the three different two-color XUV spectra of Figure 4.1(a). The inset shows the theoretical and experimental photoelectron momenta at 200 fs IR delay, along the negative and positive p_z axis, respectively. (b) Theoretical calculation of the He^+ yield under the same conditions as (a). The inset shows calculated photoelectron energies corresponding to the 750/11 nm and 750/13 nm XUV beams. The 13th + 2ω (2 IR photon) channel appears at $\pm$25 fs IR delays.

try around zero time delay. The enhancement of ionization for the positive IR delays is rather counterintuitive, and has not been observed previously. However, it has very recently been predicted theoretically [15], and can be explained as follows. In combined XUV and IR laser fields of duration 10 fs and 30 fs, respectively, small negative IR time delays correspond to the case of

ionization of He on the leading edge of the IR laser pulse (IR pulse arrives later in time than the XUV pulse). For small positive IR delays, He is ionized on the trailing edge of the IR laser pulse (IR arrives before the XUV pulse). When He is ionized as the laser intensity is increasing, the IR field ponderomotively drives the electron to periodically reencounter its parent ion, making it possible for the continuum photoelectron to recombine. This reduces the overall level of ionization by a surprisingly substantial amount. When He is ionized on the trailing edge of the laser pulse (i.e., 20 fs delay), electrons are released after the peak intensity is gone. This shuts off the recombination channel that effectively reduces the ionization rate.

Figure 4.2(b) plots the theoretical He^+ yield as a function of time delay between the XUV and IR fields. Good qualitative agreement with the experimental data can be seen. For the three XUV photon energies spanning the He $2p$ resonance, the calculated ion yield exhibits the observed yield asymmetry around zero delay. To explain different asymmetric yields for the two nonresonant XUV photon energies [red and blue, Figure 4.1(a)], we calculated the photoelectron energies corresponding to the 750/13 nm XUV wavelength. The inset of Figure 2(b) shows that the additional enhancement at ± 25 fs delay comes from absorption of 2 IR photons. The 13th + 2 IR photons ionization channel only turns on for long relative time delays between the XUV and laser fields. This channel shuts off at higher intensity (around zero delay) because the He ionization potential is ponderomotively increased [15, 73].

Armed with the knowledge of the roles the XUV and IR fields play in 2-color multiphoton ionization, we now demonstrate experimentally and theoretically that we can very sensitively control multicolor multiphoton ionization of He by interfering two ionization pathways, with the potential to completely shut off the ionization process. Varying the time delay between the XUV and IR pulses with subcycle resolution introduces ultrafast modulations of the He^+ yield. Experimental and theoretical results for different XUV photon energies and amplitude ratios are plotted in Figure 4.3. Figures 4.3(a)-4.3(c) show how the amplitude of the oscillation in the ion yield changes as the 11th-13th harmonic pair is scanned across the He $2p$ resonance that forms the Floquet double slit in the laser field, for different amplitude ratios of the 11th and 13th harmonic. Figure 4.3(d) plots

the experimentally observed oscillation in the He^+ yield when the 13th harmonic is below the $2p$ resonance. This measurement is in very good agreement with the superimposed calculated ion yield for the same IR laser intensity of 4×10^{12} W/cm^2, and for a 4:1 amplitude ratio of the 11th and 13th harmonics. Thus, we have confidence in our ability to predict the ionization yield in the two color, laser-dressed, multiphoton XUV + IR ionization process.

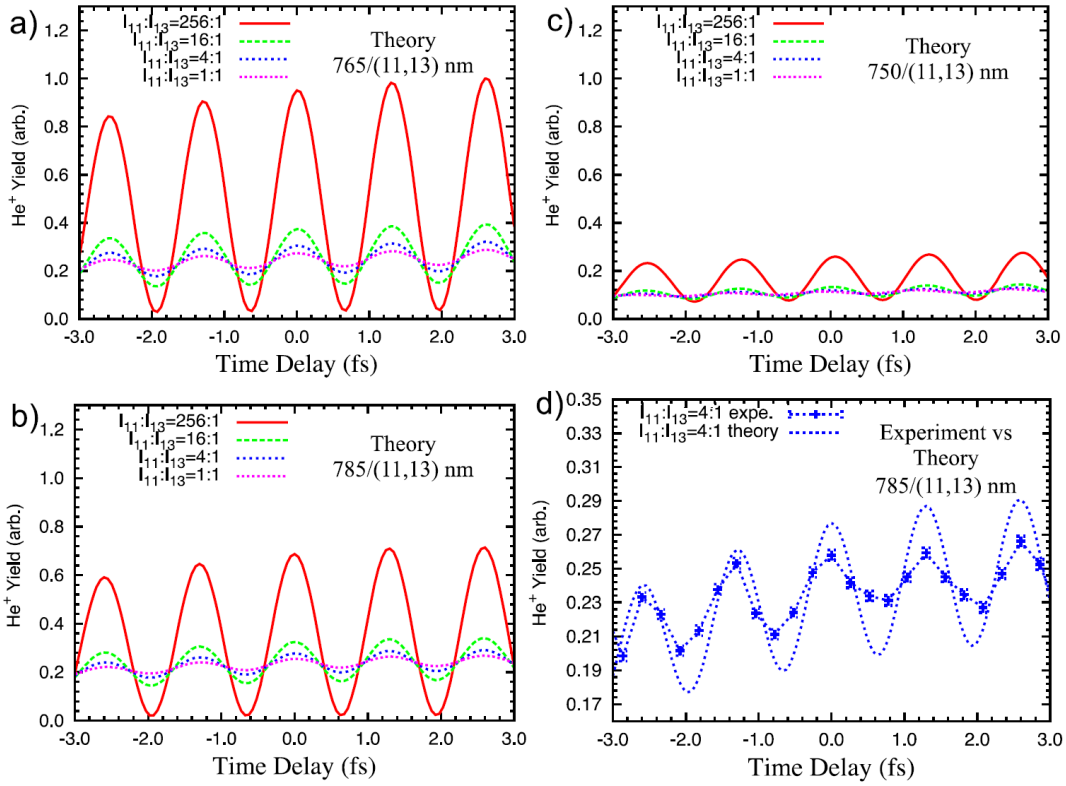

Figure 4.3: (a)-(c) Calculated modulation of the He ionization probability for different ratios of the 11th:13th harmonic fields, and for two-color 765/(11,13) nm, 785/(11,13) nm, and 750/(11,13) nm XUV beams, respectively. (d) Experimental and theoretical modulation of the He^+ yield for a laser intensity of 4×10^{12} W/cm^2, and a 785/(11,13) nm XUV field. The red curve of (a) demonstrates that a ratio of 256:1 for the 11th vs the 13th harmonic can result in nearly complete cancellation of XUV absorption.

At the IR-dressed $2p$ resonance and for an 11th:13th harmonic amplitude ratio of 256:1, we observe a near perfect modulation of the He^+ yield, with the maximum-to-minimum ratio of ≈ 40 [red curve of Figure 4.3(a)], thus demonstrating the potential to completely shut off the multiphoton

ionization process. For 785/13 nm wavelength XUV beams [red curve Figure 4.3(b)], the ratio is $\approx$ 30, while for 750/13 nm XUV beams and 11th:13th ratio of 256:1 [red curve Figure 4.3(c)], the modulation of the ion yield drops to only 5. We note that in the latter case, the maximum yield is slightly shifted from zero delay, unlike the other two cases that both maximize at zero. The highest amplitude of the oscillation, leading to complete electromagnetic transparency at the correct relative time delays, occurs for the case when the two XUV photons excite the He $2p$ Floquet states exactly through two sidebands (two Fourier components), as shown in Figures 4.1 and 4.3(a).

4.2.1 Tuning for Full Transparency

The intuitive Young double-slit picture is that for harmonic photon energies of 765/11 nm and 765/13 nm, the two XUV photons go through a double-slit interference in frequency space that is created by the IR laser field, as shown in Figure 4.1(a). Below the resonance, the photon pair does not go fully through the double slit, but still partly overlaps with the $2p$ sideband at 17.7 eV and 20.9 eV, as seen in Figure 4.1(b), and more robustly in Figure 4.1(a). Above the $2p$ resonance, the two XUV photons almost completely miss the double slit (Figure 4.1(a) and Figure 4.1(b)), which results in a small modulation in the ionization yield in Figure 4.3(c). Moreover, in this case the 3p Floquet sidebands start playing a role, making the two XUV photons to go through two double slits in series, which are displaced with respect to each other in the frequency domain. This can be seen in Figure 4.1(b), where the 13th harmonic overlaps with the 3p (and higher) IR-dressed states at 21.5 eV. This also results in shifting of the maximum yield from zero delay, as shown in Figure 4.3(c).

In conclusion, we demonstrate that full electromagnetic transparency to XUV light in helium can be achieved by destructively interfering two distinct multiphoton ionization pathways. Through combined theory and experiment, we show how a laser field can modify the electronic structure of an atom, optimizing the destructive interference between two ionization pathways under the correct conditions. This approach opens up new possibilities for coherent control of highly excited states, and emphasizes the important and complex role the IR laser field plays in strong-field ionization.

We believe that this concept can be applied to induce and control the outcome of chemical reactions, as well as in condensed matter physics where the concept of the resonance dressing, shifting, and broadening can be applied to the electronic band structure.

Chapter 5

Bromine[1]

Imaging and controlling reactions in molecules and materials at the level of electron dynamics is a grand challenge in science, relevant to our understanding of charge transfer processes in chemistry, physics, and biology, as well as material dynamics. Direct access to the dynamic electron density as electrons are shared or transferred between atoms in a chemical bond would greatly improve our understanding of molecular bonding and structure. In this Chapter, we show how the entire valence shell electron density in a molecule rearranges, from molecular-like to atomic-like, as a bond breaks. An intense ultrashort laser pulse is used to ionize a bromine molecule at different times during dissociation, and we measure the total ionization signal and the angular distribution of the ionization yield. Using this technique, we can observe density changes over a surprisingly long time and distance, allowing us to see that the electrons do not localize onto the individual bromine atoms until the fragments are far apart (∼5.5 Å), in a region where the potential energy curves for the dissociation are nearly degenerate. These observations agree well with calculations of the strong-field ionization rates of the bromine molecule.

5.1 Visualization of electron dynamics

Probing the dynamic electron density distribution during a chemical reaction can provide important insights, making it possible to understand and control chemical reactions. For example,

[1] The results of this chapter are in part based on "W. Li, A. A. Jaroń-Becker, C. W. Hogle, V. Sharma, X. Zhou, A. Becker, H. C. Kapteyn, and M. M. Murnane, Proceedings of the National Academy of Sciences **107**, 47, 20219 (2010)" [82].

during the passage through a conical intersection, electronic excitation is rapidly converted into nuclear motion, and the nature of how the electron cloud rearranges is still poorly understood. Three distinct and promising approaches make it possible to probe electron dynamics in molecules. First, high harmonic generation from a molecule can exhibit characteristic features because of quantum interferences and diffraction of an electron originating from and then recolliding with the same molecule. Although the conditions under which accurate reconstruction of a complete electronic wave function is possible are still a topic of intense debate, nevertheless, these characteristic interferences can reveal dynamical changes in the nuclear and orbital structure of a molecule as it changes configuration [83–86] or dissociates [87]. In the case of dissociation, by measuring the amplitude and phase of the high harmonic signal from a dissociating molecule, destructive interferences in the high harmonic signal were observed that were attributed to recombination of a lone electron in a single excited state [87]. To follow multielectron dynamics in a molecule, further work will be needed, because the quantum interference signal can be masked by competing contributions from different nearly degenerate valence orbitals, in particular at large internuclear distances.

A second approach for obtaining information about electron dynamics is to map the electron density distribution in the valence shells of a molecule, simply by measuring the molecular frame ionization yield after illumination by a strong laser field. Past work probing static molecules in the ground state has shown through both theory and experiment that the resulting ion yield reflects the symmetry of the molecular orbital from which the electron is ionized [88–93]. As a result, strong-field ionization should be particularly attractive for capturing electron orbital dynamics because it directly relates to the electron density distribution (i.e., orbital shape) of a molecule. In a third approach, the coupling between an excited electron and nuclear motion in a molecule can be probed by using time-resolved photoelectron spectroscopy (TRPES) [12, 68, 94]. In TRPES, a vacuum ultraviolet (VUV) pulse is used to single-photon ionize a molecule, making this technique particularly useful for measuring how the binding energies of electrons in different valence orbitals change as the molecule dissociates. However, the linear response in a photoelectron spectroscopy measurement makes it challenging to follow shifts in the binding energies and to directly probe

the varying electron density in the bond, on time and length scales for which the potential energy curves become nearly degenerate. A femtosecond laser strong-field ionizes a molecule as it undergoes photodissociation. The dissociation itself is initiated in a simple, single-photon transition by using a pump pulse. A higher intensity probe pulse is then used to ionize the molecule at various time delays, causing the fragments to fly apart rapidly with a distribution that reflects the instantaneous electron distribution. Both the detected ionization rate and fragment angular distribution directly reflect how the entire valence shell electron density in a molecule rearranges, from molecular-like to atomic-like, as a bond breaks. The experimental results can be successfully interpreted through careful comparison with theory. This also shows an ability to capture multielectron dynamics in a reaction up to significantly larger internuclear distances than with other methods. It also exhibits high sensitivity to small variations in the binding energy and electron density, as well as excellent time resolution compared with other approaches. This approach thus allows us to see that the electrons do not localize onto the individual bromine atoms until the fragments are far apart (∼5.5 Å), in a region where the potential energy curves for the dissociation are nearly degenerate.

5.1.1 Experimental Bromine Dissociation

The sample consists of a bromine molecular beam from the supersonic gas jet. Dissociation of the Br_2 is initiated by a 400 nm ultrafast laser pulse (intensity $\sim 2 \times 10^{11}$ W/cm^2, pulse duration ∼40 fs) generated by frequency doubling the 800 nm laser output. The absorption of a single 400 nm photon excites the bromine molecule from the ground state to the C ($^1\Pi_u$) dissociative state. To confirm that the Br^+ ions are indeed originating from strong-field ionization of the dissociative C state, we measured the Br^+ yield as a function of pump beam power and found it to be linear as shown in Figure 5.2. An intense time-delayed 800 nm ($\sim 4 \times 10^{13}$ W/cm^2, ∼30 fs) laser pulse, with polarization orthogonal to the 400 nm pump, is used to ionize the dissociating bromine molecules to produce Br^+. We then detect the angular distribution of the resultant ions at different times during the dissociation as shown in Figure 5.1. Given that the dissociation is a prompt process, we therefore know how the electron density in the molecule changes as the molecule dissociates into

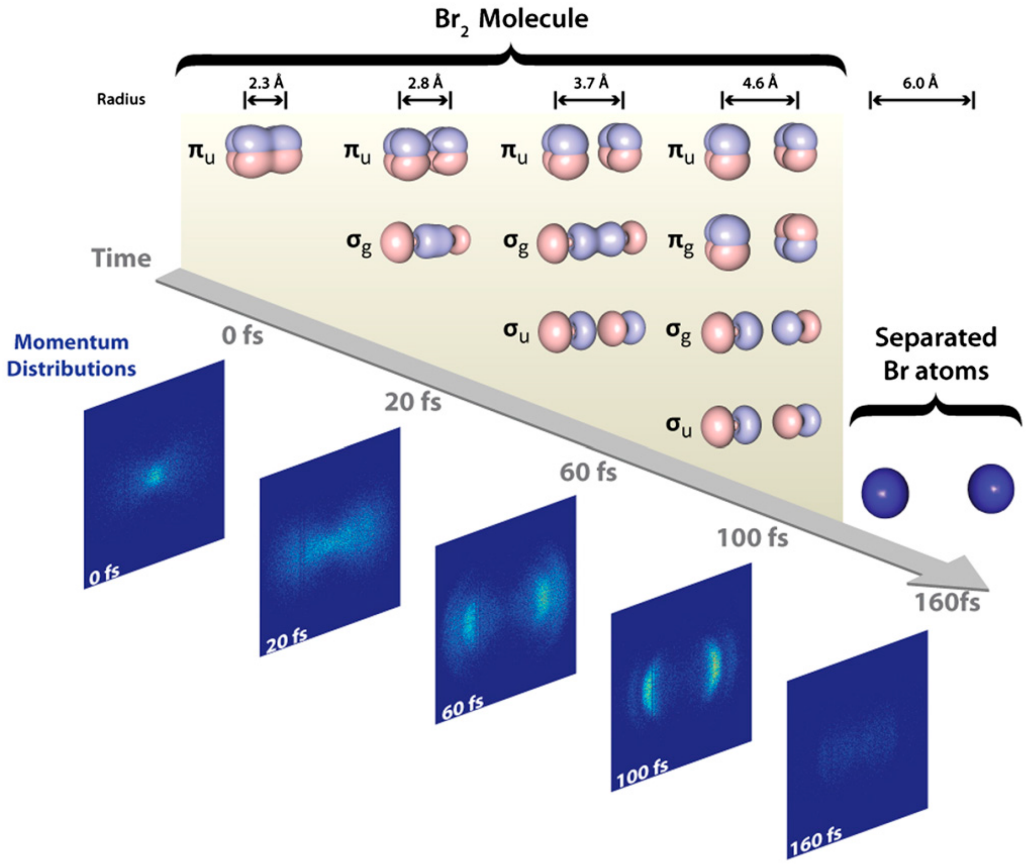

Figure 5.1: Calculated electron density (molecular orbitals) as a function of Br_2 internuclear separation and time after a 400 nm dissociating pulse causes the bond to rupture on the dissociative C neutral state. Note that contributions from all 10 electrons in the valence shells are included. Measured angular dependence of the Br^+ ion yield from strong-field ionization of the Br_2 molecule, as a function of time after the dissociating pulse. Both experiment and theory indicate that the electrons localize onto individual atoms on a time scale 140 fs after the dissociating pulse.

two atoms.

5.1.2 Power Dependence of Br^+ Yield

In order to confirm that the Br^+ ions observed in this experiment are indeed originating from strong field ionization of the dissociative C state, we measured the Br^+ yield as a function of pump beam power at a fixed pump-probe delay of 120 fs. The integrated Br^+ yield for KER <0.8 eV is shown in Figure 5.2. A linear dependence of the Br^+ yield on the power clearly shows that the

pump step of our experiment indeed involves a single photon process (i.e., absorbing only one 400 nm photon). The experiment was performed with only 5 μJ of pump energy, corresponding to a laser intensity of 2×10^{11} W/cm^2. This intensity is at least 5 times smaller than that used in the extreme ultraviolet photoionization probe studies of Br_2 dissociation performed previously [95,96]. Thus we believe that our experiments have a relatively low probability of complications resulting from multiphoton processes to other excited states in the Br_2 molecule.

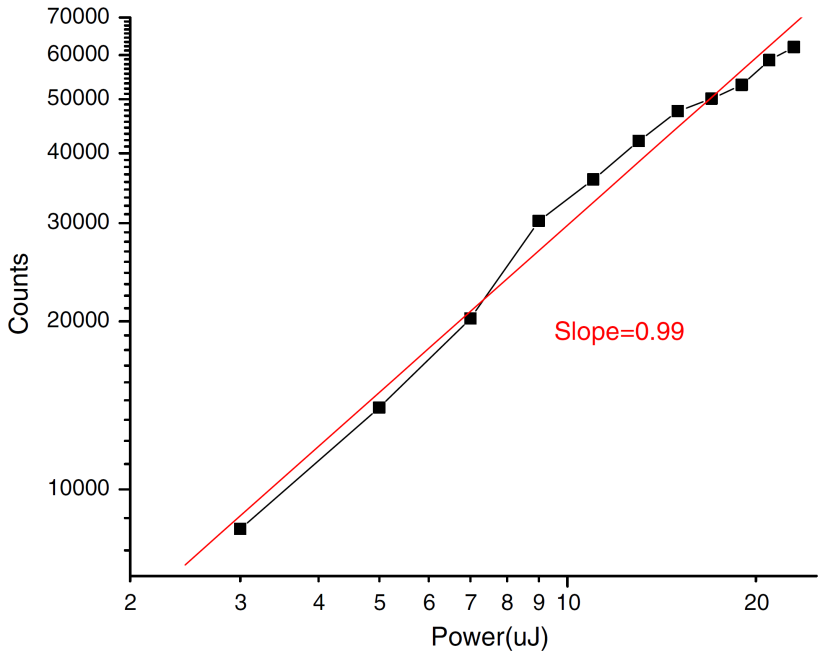

Figure 5.2: Power dependence of slow (i.e., KER < 0.8 eV) Br^+ yield. Black squares correspond to the experimental Br^+ count, as a function of pump (400 nm) power. The red line is a linear fit to data. The measured slope of 0.99 verifies that our dissociation signal is initiated by a single photon.

Figure 5.3 plots the total ion yield as a function of time delay between the 400 nm dissociating pulse and the 800 nm probe pulse. The total ion yield initially increases for time delays up to 30 fs, at which point it decreases slightly, followed by an increase at time delays around 100 fs. As we will show below by comparing detailed theory and experiment, the first peak corresponds to ionization of electrons from π orbitals, whereas second peak can be explained by additional ionization channels

opening up as different σ valence electrons are ionized. Finally, the ion yield drops quickly at time delays between $\sim$ 120 and 140 fs, limited by the time resolution in our experiment.

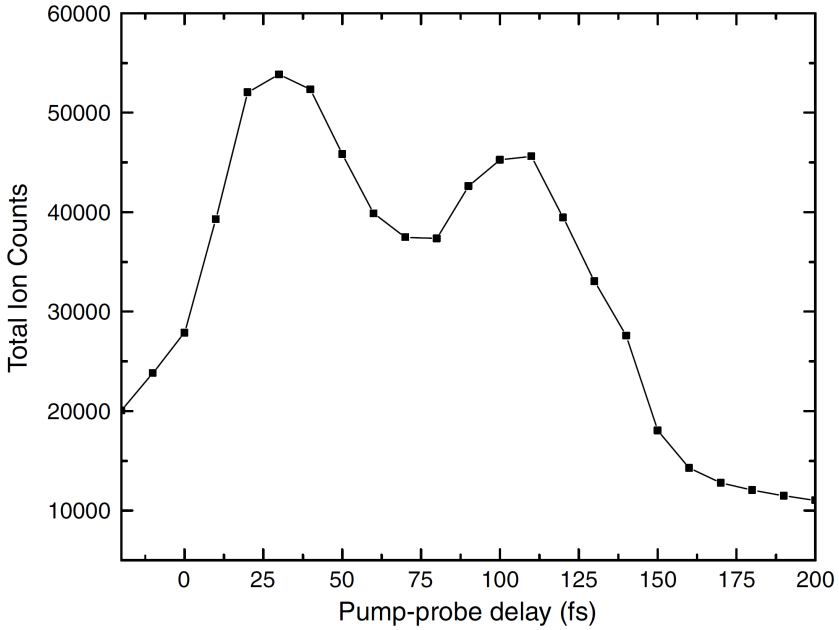

Figure 5.3: Experimental Br^+ total ion yield as a function of time delay between the 400 nm dissociating pulse and the 800 nm probe ionizing pulse. The first peak corresponds to ionization of electrons from π orbitals. The second peak can be explained by additional ionization channels opening from σ valence electrons.

5.2 Calculated and Experimental KER

To interpret the experimental data, the ionization rate from the dissociative C state of Br_2 was calculated as a function of internuclear distance by using the molecular strong-field approximation [97]. The results of these calculations can be plotted in terms of the final kinetic energy release (KER) of the fragments as a function of time delay. The calculated KER is in very good agreement with our experimental measurements as shown in Figure 5.4. We note that the characteristic features of the distributions are slightly shifted to longer time delays in the theoretical results, which may be attributed to the sensitive dependence of the conversion from distance to time delay on the specific form of the C-state potential energy curve.

The calculations of Figure 5.4 indicate that we are experimentally observing the entire valence shell of Br_2 (all ten electrons) evolving in time as the bond breaks, as shown in Figure 5.1. The electron configurations of the ground X and dissociative C states of Br_2 are $[core](1\sigma_g)^2(1\sigma_u^*)^2(2\sigma_g)^2(1\pi_u)^4(1\pi_g^*)^4(2\sigma_u^*)^0$ and $[core](1\sigma_g)^2(1\sigma_u^*)^2(2\sigma_g)^2(1\pi_u)^4(1\pi_g^*)^3(2\sigma_u^*)^1$, respectively. Removal of one electron from different orbitals of the C state of Br_2 leads to different electronic configurations of the cation. For example, strong-field ionization of the singly occupied molecular orbital ($2\sigma_u^*$) electron primarily produces $Br_2{}^+$ in its ground state X with electronic configuration: $[core](1\sigma_g)^2(1\sigma_u^*)^2(2\sigma_g)^2(1\pi_u)^4(1\pi_g^*)^3(2\sigma_u^*)^0$. This state, as well as certain excited states of bound character, will not produce Br^+ at short internuclear distances during the dissociation process. At short time delays (below 20 fs), slow Br^+ ions are instead generated predominantly by ionizing the inner valence orbital $1\pi_u$. After dissociating for about 20 fs, the atoms have gained enough kinetic energy such that ionization from $2\sigma_g$ and $2\sigma_u^*$ opens additional channels for the dissociation of $Br_2{}^+$. The additional channels that continue to open up also explain why the total ionization yield increases as a function of time delay. At long time delays, fast Br^+ ions originate primarily from ionizing $2\sigma_g$, with minor contributions from other orbitals. The peak around 60 fs in Figure 5.4 results from strong contributions of electron removal from $2\sigma_u$. Thus, we are able to identify the specific molecular orbitals that contribute primarily to the ionization and kinetic energy release signals up to a time delay of 140 $\pm$ 15 fs. This analysis indicates that the system still must be considered molecule-like and the electrons in the valence shell(s) of the system are still rearranging their configuration at these relatively long times (corresponding to internuclear separations larger than 5 Å). This finding is surprising because by then, according to calculations, the four valence orbitals in the Br_2 molecule are nearly degenerate and the electron probability density at the midpoint between the two nuclei is 10 orders of magnitude smaller than the peak maximum.

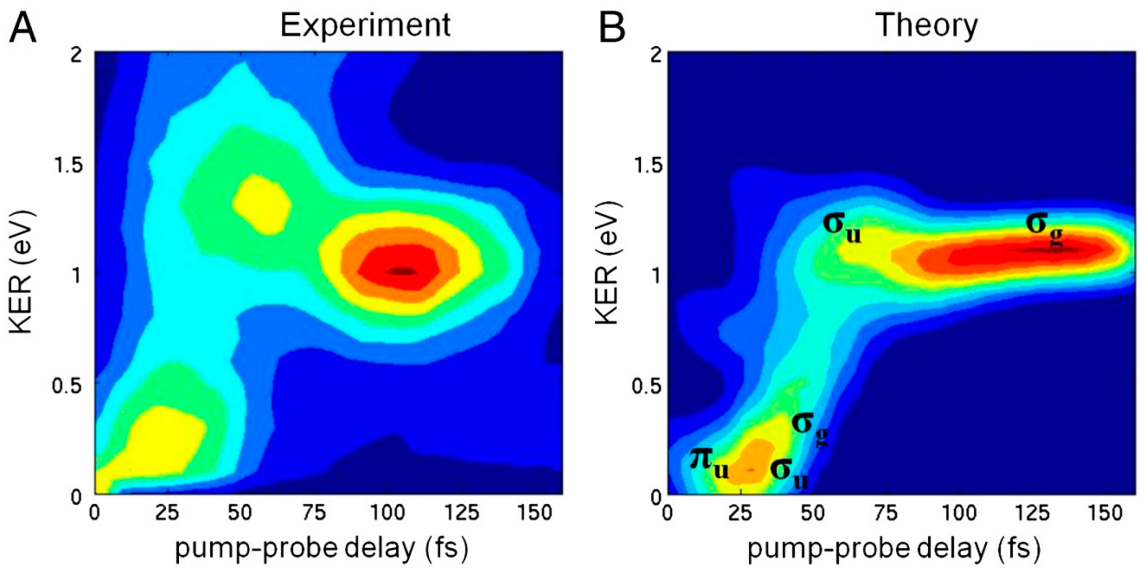

Figure 5.4: Experimental (A) and calculated (B) total KER of the Br^+ as a function of time after the dissociating pulse. At short time delays (below 20 fs), Br^+ ions are generated predominantly by ionizing the inner valence orbital $1\pi_u$ of the molecule. After dissociating for about 20 fs, the atoms have gained enough kinetic energy such that ionization from $2\sigma_g$ and $2\sigma_u^*$ opens additional channels for the dissociation of $Br_2{}^+$.

5.3 Angular Ion Distribution

To physically interpret our findings, we plot the experimental angular distribution of Br^+ as a function of time delay for both the slow Br^+ (Figure 5.5(A), kinetic energy release below 0.7 eV) and fast Br^+ (Figure 5.5(B), kinetic energy release above 0.7 eV). We fit the angular distribution to a simple $\cos^n(\theta)$ [θ is the angle between the molecular axis and probe (ionizing) laser polarization]. Because photoexcitation of the C state is a perpendicular transition [98], the observed angular distributions of Br^+ are convolutions of the Br_2 excited state molecule axis alignment [$\cos^2(\theta)$ distribution] and the angular dependence of the Br_2 ionization rates. Thus, the sign of $n-2$ (plus or minus) shows whether the ionization is peaked parallel (+) or perpendicular (−) to the laser polarization, reflecting ionization from specific molecular orbitals. At short time delays, slow Br^+ has an n below 2, indicating ionization from the π_u state, whereas for fast Br^+, the ionization

yield is highest along the molecular axis, indicating ionization predominantly from a σ state. These findings are in agreement with our calculations (Figure 5.1 and Figure 5.4). More importantly, we observe such molecular-specific features up to time delays of 140 fs. After this time, the ion angular distributions flatten and appear to resemble ionization from separated atoms; i.e., the distribution reflects only the initial excited state molecule axis alignment in Br_2.

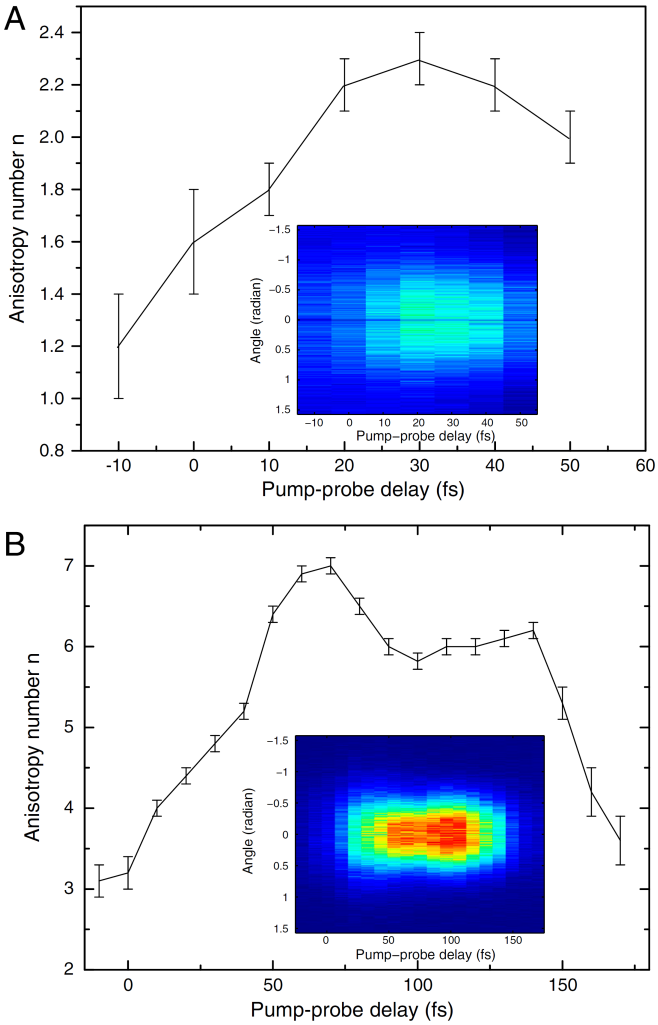

Figure 5.5: Angular distribution of Br^+ at different time delays after the dissociating pulse, for both the slow Br^+, (a) kinetic energy release below 0.7 eV, and fast Br^+, (b) kinetic energy release above 0.7 eV. At short delays slow Br^+ indicates ionization from the π_u state. Fast Br^+ is predominantly along the molecular axis and so mostly from a σ state

5.4 Laser Field Driven Dynamics

We also calculated the alignment dependence of the ionization rate, taking into account that in the experiment, the excited Br_2 are prepared with a $\cos^2(\theta)$ alignment of the molecular axis to the polarization direction. We believe that we are not inducing significant laser field driven electron dynamics, for several reasons. First, the most important point in discussing the possible role of strong-field effects is that, although our technique uses a relatively strong laser pulse as a probe of the molecular dynamics, our technique allows us to avoid strong-field effects in initiating the dynamics that we observe. Comparing our approach to TRPES, where the VUV probe pulse is capable of photoionizing even ground-state Br_2, in TRPES, a relatively intense pump pulse has to be used to obtain significant fractional population in the excited state. Thus, in TRPES, strong-field effects in the excitation step might explain the more rapid dissociation times observed in previous experiments (≈85 fs) [96]. In our experiment, an ion signal emerges only from the dissociating molecules and is thus background free. The fact that we see a precipitous drop in signal at long time and distance scales clearly shows that our signal discriminates against both the initial and the final state of dissociation, allowing us to observe the entire dissociation process that was initiated by a clearly perturbative, single-photon, excitation (as demonstrated in Figure 5.2). Moreover, our calculations agree well with the data, even without including laser induced modifications of the initial electronic state or charge resonance-enhanced ionization [99, 100]. Finally, the calculated kinetic energy releases and angular distributions do not change for a range of probe laser intensities (4-5 $\times$ 10^{13} W/cm^2) and for different ensembles of molecular orientations induced by the pump pulse.

In conclusion, we have demonstrated that we can image the electron density evolution of many electron states in the valence shell of a large diatomic molecular system up to time and distance scales at which the potential energy curves become nearly degenerate. We have shown that, because of the nonlinear interaction of an ultrashort intense laser pulse with the electrons, strong-field ionization can probe the electronic structure of a dissociating molecule even if the changes in

the potential energy surfaces are small. Our studies show that both the ionization rate and the angular dependence of the ionization yield still vary strongly for internuclear distances at least 2 Å beyond where previous studies using photoelectron spectroscopy identified an establishment of the atomic electronic structure in Br_2. We believe that the existence of such a molecular-like complex for large time and length scales is not restricted to Br_2 and should have broad implications for many fields such as photochemistry and reactive scattering dynamics. Interestingly, our observations and calculations are in good agreement with electron localization function calculations [101,102], which indicate delocalization of the electrons in the different orbitals until internuclear separations >5.0 Å for Br_2 in the excited C state. Thus, using strong-field ionization as a probe, we can follow electron dynamics in a bond over sufficiently long times to capture all the time scales during a chemical reaction.

Chapter 6

Deuterium[1]

High harmonic light sources make it possible to access attosecond timescales, thus opening up the prospect of manipulating electronic wave packets for steering molecular dynamics. However, two decades after the birth of attosecond physics, the concept of attosecond chemistry has not yet been realized; this is because excitation and manipulation of molecular orbitals requires precisely controlled attosecond waveforms in the deep ultraviolet (UV), which have not yet been synthesized. In this Chapter, we present a unique approach using attosecond vacuum UV (VUV) pulse-trains to coherently excite and control the outcome of a simple chemical reaction in a deuterium molecule in a non-Born-Oppenheimer regime. By controlling the interfering pathways of electron wave packets in the excited neutral and singly ionized molecule, we unambiguously show that we can switch the excited electronic state on attosecond timescales, coherently guide the nuclear wave packets to dictate the way a neutral molecule vibrates, and steer and manipulate the ionization and dissociation channels. Furthermore, through advanced theory, we succeed in rigorously modeling multiscale electron and nuclear quantum control in a molecule. The observed richness and complexity of the dynamics, even in this very simplest of molecules, presents intriguing new possibilities for bridging the gap between attosecond physics and attosecond chemistry.

[1] The results of this chapter are in part based on "P. Ranitovic, C. W. Hogle, P. Rivire, A. Palacios, X.-M. Tong, N. Toshima, A. Gonzlez-Castrillo, L. Martin, F. Martín, M. M. Murnane, and H. C. Kapteyn, Proceedings of the National Academy of Sciences **111**, 3, 912 (2014)" [23].

6.1 Coherent Control of Molecular Dynamics

The coherent manipulation of quantum systems on their natural timescales, as a means to control the evolution of a system, is an important goal for a broad range of science and technology, including chemical dynamics and quantum information science. In molecules, these timescales span from attosecond timescales characteristic of electronic dynamics, to femtosecond timescales characteristic of vibrations and dissociation, to picosecond timescales characteristic of rotations in molecules. With the advent of femtosecond lasers, observing the transition state in a chemical reaction [1], and controlling the reaction itself, became feasible. Precisely timed femtosecond pulse sequences can be used to selectively excite vibrations in a molecule, allow it to evolve, and finally excite or deexcite it into an electronic state not directly accessible from the ground state [103]. Alternatively, interferences between different quantum pathways that end up in the same final state can be used to control the outcome of a chemical reaction [76–78, 104–107].

In recent years, coherent high harmonic sources with bandwidths sufficient to generate either attosecond pulse trains or a single isolated attosecond pulses have been developed that are also perfectly synchronized to the driving femtosecond laser [108–110]. This new capability provides intriguing possibilities for coherently and simultaneously controlling both the electronic and nuclear dynamics in a molecule in regimes where the Born-Oppenheimer approximation is no longer valid, to select specific reaction pathways or products. We perform a coordinated experimental and theoretical study of dynamics of the simplest neutral molecule: deuterated hydrogen (D_2).

The hydrogen molecule, as the simplest possible neutral molecule that can be fully described theoretically, has been the prototype molecule for understanding fundamental processes that lie at the heart of quantum mechanics [111–114]. However, in such a small molecule, the coupled electron-nuclear dynamics are in the attosecond-to-few-femtosecond regime, whereas the electronically excited states lie in the VUV region of the spectrum. Because of the challenge of generating attosecond VUV pulses using traditional laser frequency doubling or tripling in nonlinear crystals, it has not been possible to date to explore the dynamics of an electronically excited hydrogen

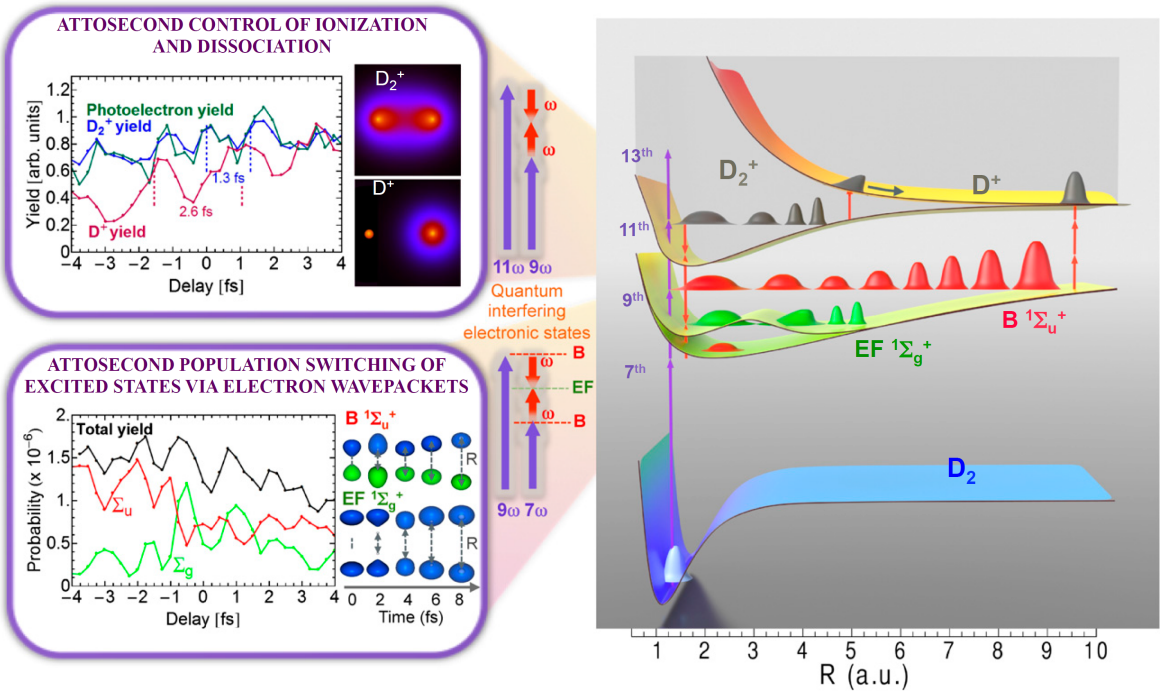

Figure 6.1: Attosecond control of the excitation and ionization pathways of D_2 on short timescales. (right) Simplified potential energy surfaces of the D_2 and D_2^+. The purple and red arrows represent the VUV harmonics and IR laser pulses used to coherently control the populations of the excited neutral and ion states in the Franck-Condon region through two-pathway quantum interference of electronic wave packets in B, B* (single photon) and EF (two photon) states. (Lower left inset) Calculated excitation probabilities into states of Σ_u and Σ_g symmetries of neutral H_2 (dominated, respectively, by the B and EF states) as a function of time delay. The blue lobes, plotted on the right of the panel, are sketches of the Σ_u and Σ_g orbitals representing the excited electron dynamics. Theoretical predictions show that the electronically excited populations can be switched between the even B and odd parity EF potentials on attosecond timescales, which can in turn control how the molecule vibrates. (Upper left inset) The experimental photoelectron, D_2^+ and D^+ yields modulate on full and half-cycle attosecond timescales, as the delay between the pump VUV + IR and probe IR pulses is scanned.

molecule. Exploiting attosecond physics, however, only a handful of time-resolved experiments have been performed on H_2 (D_2), focusing mainly on controlling dissociation through electron localization in electronically excited D_2^+ ions [69, 115–120]. Recently it was realized that IR femtosecond laser pulses, in combination with a phased locked comb of attosecond VUV harmonics, can be used to control the excitation and ionization yields in helium on attosecond timescales, by interfering electron wave packets [15, 72]. These experiments extended the Brumer-Shapiro [76–78, 104–107]

two-pathway interference coherent control concept to the attosecond temporal and VUV frequency domain. More recently, it was shown that by manipulating the individual amplitude of VUV harmonics, it is possible to induce full electromagnetic transparency in helium, by destructively interfering two electronic wave packets of the same amplitude and opposite phases [63]. Other recent work used shaped intense femtosecond laser pulses to manipulate populations by controlling the oscillating charge distribution in a potassium dimer [121].

Using attosecond scale VUV harmonics, we can coherently and simultaneously manipulate multistate electronic and multipotential-well nuclear wave packet dynamics to control the excitation, nuclear wave packet tunneling, and dissociation and ionization channels of the only electronically excited neutral molecule where full modeling of the coupled quantum dynamics is possible, H_2 (for practical reasons, we used deuterated hydrogen in this experiment). By combining attosecond pulse trains of VUV with two near-IR fields, together with strong-field control that exploits a combination of the two-pathway interference Brumer-Shapiro [76–78, 104–107] and pump-dump Tannor-Rice [103] approaches, we demonstrate that we can selectively steer the ionization, vibration, and dissociation of D_2 through different channels. Interferences between electronic wave packets (evolving on attosecond timescales) are used to control the population of different electronic states of the excited neutral molecule, which can be switched on attosecond timescales. Then, by optimally selecting the excitation wavelengths and time delays, we can control the vibrational motion, total excitation, ionization yield, and desired ionization and dissociation pathways. State-of-the-art quantum calculations, which have only recently become feasible, allowed for the interpretation of this very rich set of quantum dynamics, including both the nuclear motion and the coherently excited electronic state interferences. Thus, we succeed in both observing and rigorously modeling multiscale coherent quantum control in the time domain.

6.2 Phase-Locked VUV + IR Source

We note that our approach for control, using a combination of phase-locked VUV and IR fields, where the VUV field consists of an attosecond pulse train with a 10 fs pulse envelope, is ideal

for coherently exciting and manipulating electronic and vibrational states on attosecond time scales, while simultaneously retaining excellent spectral resolution necessary for state-selective attochemistry. Exciting electron dynamics in a molecule using a single, broad-bandwidth VUV attosecond pulse would simply excite many ionization/dissociation channels with little state selectivity, potentially masking the coherent electronic and nuclear quantum dynamics. For example, the bandwidth required to support an isolated 200 attosecond pulse around 15 eV is ∼5 eV. In contrast, the 10 fs VUV pulse train used here corresponds to a comb of VUV harmonics, each with a FWHM bandwidth of 183 meV, which can be tuned in the frequency domain [63] to coherently and selectively excite multiple electronic states.

Figure 6.1 illustrates our concept for attosecond coherent control of molecular dynamics. A neutral deuterium molecule is electronically excited and ionized by combined phase-locked VUV harmonics ($7\omega - 13\omega$) and ultrafast IR (ω) pump fields at a center laser wavelength of 784 nm. A second control IR pulse is time-delayed with respect to the combined VUV + IR fields. For simplicity, only the two most relevant electronically excited states of different parity in D_2 are shown in Figure 6.1. As we will explain in more detail below, interferences between electron wave packets excited by the combined VUV harmonics (i.e., 7ω, 9ω, and 11ω) and the IR field (ω) are used to manipulate the ionization and excitation probabilities of different electronic states of the excited neutral molecule. To modulate the total electronic excitation in the neutral molecules on attosecond timescales, we use two-pathway quantum interference of electronic wave packets excited by $7\omega + \omega$ and $9\omega - \omega$. Simultaneously, to modulate the total ionization yield on attosecond timescales, we use two-pathway quantum interference of electronic wave packets excited by $9\omega + \omega$ and $11\omega - \omega$ as the main mechanism. Finally, by tuning the VUV excitation wavelengths, we achieve other degrees of coherent control of coupled electron-nuclear wave packet dynamics, including vibration, ionization, and tunneling. First, we show how the population of two electronic states can be switched (i.e., between EF and B) on attosecond timescales (Figure 6.1, Lower Left). Second, we show that by tuning the energy of the VUV harmonic comb, we can excite and control the population of different electronic and vibrational states, which in turn dictates how the neutral

molecule vibrates and ionizes. Third, by exciting D_2 using tunable two-color VUV and IR fields, and then probing the dynamics using a second IR pulse, we can control tunneling of nuclear wavepackets in the EF potential of a neutrally excited D_2.

The seventh and ninth harmonics coherently excite the molecule from its ground state, creating two nuclear wave packets in the same, odd-parity (i.e., B $^1\Sigma_u^+$) potential energy surface of D_2. When a small portion of the driving IR field (at an intensity of 3×10^{11} W/cm^2) copropagates with the VUV harmonics, we can also simultaneously populate the optically forbidden, even-parity (i.e., EF $^1\Sigma_g^+$) potential energy surface through two-photon (i.e., $7\omega + \omega$, $9\omega - \omega$) absorption processes. A second, time-delayed, and stronger IR (ω) pulse (at an intensity of 4×10^{12} W/cm^2) is then used in two different ways. First, on short attosecond timescales, the delayed IR field interferes with the IR field that copropagates with the VUV harmonics, and serves as a knob to control the excitation and ionization processes on attosecond timescales in the Franck-Condon region, by means of electron wave packet interferometry. Second, on long femtosecond timescales, the delayed IR field serves as a femtosecond knob to control the dissociation process by selectively ionizing the molecule at some optimal time after excitation. All of the pulses (VUV attosecond pulse trains and two IR fields) were linearly polarized in the same direction. The VUV pulse duration was 5-10 fs, and the IR pulse durations were 30 fs. By changing the pressure in the gas-filled capillary, we can fine-tune the exact photon energies of the VUV harmonics while keeping the IR wavelength constant. This capability is key for uncovering the control mechanisms.

We first examine the attosecond control pathways at early times, before the onset of large-period vibrational wavepacket dynamics. Figure 6.1, Upper Left plots the experimental photoelectron, D_2^+ , and D^+ yields when the pump (VUV + IR) and the control (IR) pulses were overlapped in time, as a function of the time delay between them. Very rapid, suboptical-cycle modulations in the photoelectron and D_2^+ yields result from the combination of optical interferences (two IR pulses) and quantum interferences of electronic wavepackets (i.e., $9\omega + \omega$ and $11\omega - \omega$ interfering pathways), as the phase of the control IR pulse changes relative to the pump VUV + IR pulse. Half-cycle periodicity suggests that the two-pathway quantum interferences play an important role

in this particular case [81]. The deep, full-cycle modulation of the dissociative D^+ yield is simply a result of the optical interferences between the pump and control IR pulses (both 30 fs long) that lead to bond-softening of the ground state of D_2 and ionization of the D_2^* excited states ~10 fs after the pump pulse. Because the dissociation by bond-softening occurs after the VUV pulse is gone, this signal provides a reference point of the absolute phase in between the two IR pulses at each time delay, and allows us to precisely know the phase of the quantum interferences relative to the laser field.

6.3 Theoretical Calculations

Theoretical calculations (Figure 6.1, Lower Left) show that the electronic population in the excited states also oscillates, with the same half-cycle periodicity. Moreover, theoretically, we can remove the parity degeneracy in the total excitation yield and see that the populations in the gerade and ungerade B and EF states are out of phase. Thus, a two-pathway quantum interference of the electron wave packets driven by the lower two harmonics and the delayed IR field (i.e., $7\omega + \omega$ vs. $9\omega - \omega$, Figure 6.1, Lower Left) can be used as an ultrafast population switch between even (EF) and odd parity (B) potentials; this demonstrates that the interference of electronic wavepackets can be used to switch and steer the electronically excited states on attosecond time scales, allowing simultaneous control of the electronic and vibrational excitation of an excited neutral D_2^* molecule. Thus, we demonstrate how combined attosecond VUV and IR femtosecond fields can be used as a unique tool to coherently control chemical reactions on the fastest timescales.

It is worth noting that though there are other possible interfering pathways responsible for the excitation and the ionization yield modulations, they are significantly less likely because they require more photons. For example, the interference of electronic wave packets excited by $7\omega + 3\omega$ and $11\omega - \omega$ is possible. In this case, the total ionization probability is controlled by coupling the lower vibrational states of the B potential excited by the seventh harmonic, with the continuum electron wave packets created by the 11th harmonic. Though this channel competes with the state excited by the ninth harmonic, it requires absorption of four photons, and is thus much less probable

compared with the pathway requiring absorption of two photons (one VUV and one IR).

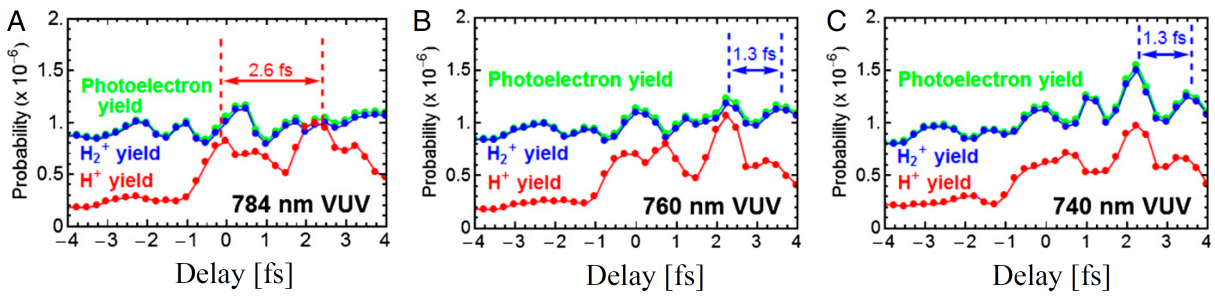

Figure 6.2: Theory of attoseocond VUV coherent control of H_2 ionization/dissociation channels. (A-C) As the central energy of the VUV frequency comb is blue-shifted from an effective driving laser wavelength of 784 nm to 740 nm, the total ionization yield switches to half-cycle periodicity due to different electronic wavepacket interferences, thus demonstrating attosecond coherent control over the interfering electron wave packets and ionizing pathways in molecules.

Because we solve the full 3D time-dependent Schrdinger equation (TDSE) for H_2 exposed to a combined VUV and IR fields, we can theoretically examine the attosecond control mechanisms by fine-tuning the photon energy of the VUV pulse. The TDSE is numerically solved by expanding the time dependent wave function in a large basis of Born-Oppenheimer molecular states, which are obtained by diagonalization of the electronic and nuclear Hamiltonians of H_2. The method includes all electronic and nuclear degrees of freedom and, therefore, accounts for electron correlation and the coupling between the electronic and nuclear motions. Time evolution starting from the ground state induces transitions between the Born-Oppenheimer states through laser-molecule and potential couplings. To make these complex calculations tractable, in the simulation we used IR and VUV pulses of 7.75 fs total duration. Although these pulses were shorter than the ones used experimentally (30 fs and 5-10 fs, respectively), a direct comparison between the theory and the experiment can still be made during the time-delay interval when the pump and probe pulses overlap. The theoretical results are shown in Figure 6.2, and capture the main experimental observationsthat the total yields modulate on attosecond timescales, and that the periodicity and the amplitudes of the oscillations strongly depend on the exact central energy of the VUV pulse. Here, we keep the IR laser wavelength constant while blue-shifting the VUV central wavelength as

although the higher harmonics were generated by 784 nm, 770 nm, and 760 nm laser wavelengths shown, respectively, in Figure 6.2. Not surprisingly, the modulation of the total ionization yield strongly depends on the exact energy of the VUV harmonics because the phases and the amplitudes of the interfering electron wave packets strongly depend on the laser-modified electronic structure of the molecule [3]. In the case of H_2, as the central energy of the VUV beam blue-shifts from harmonics of 784 nm to harmonics of 740 nm, the ninth harmonic does not excite the B state in the Franck-Condon region, but accesses higher electronic states. In this regime the Born-Oppenheimer approximation breaks down, because the evolution of the nuclear wavepackets in the B and EF potentials is on the same timescale as the duration of the attosecond VUV pulse train (Figure 6.1, Lower Left) and can influence the electron wave packet interference process as well. These results thus demonstrate that we can precisely control which electronic states are excited by the tunable VUV harmonics, and show how these states can be switched on attosecond timescales.

6.4 Multiscale Quantum Control of Electronic and Nuclear Dynamics

To show experimentally how tunable attosecond VUV pulse trains can be used to precisely control the excitation probabilities of different electronic and vibrational states, and how to steer ionization and dissociation in D_2^*, we delay the control IR field relative to the VUV + IR pump field on femtosecond timescales. Figure 6.3 illustrates several possible ionization and dissociation pathways and plots the energies of the three different attosecond VUV harmonic combs we used to coherently and simultaneously control electronic and vibrational excitation, as well as nuclear wave packet tunneling in the EF potential. The combined $7\omega + \omega$, $9\omega - \omega$, and 9ω fields coherently populate the EF $^1\Sigma_g^+$ and B $^1\Sigma_u^+$ states, respectively. These nuclear wave packets oscillate with periods that depend on the exact energy of the VUV harmonics, and can couple the ground state to different vibronic bands of the B and EF potentials. The probe IR pulse can then ionize and dissociate D_2^* through different channels as the electronically excited neutral molecule vibrates. Here we focus only on three channels that leave the most visible signature in the kinetic energy release (KER) spectrum of D^+, which we label as two-step B, one-step B, and two-step EF (Figure

6.3). In the two-step B case, shown in Figure 6.3(A), the nuclear wave packet launched in the B state by the ninth harmonic is first probed in the inner classical turning point of the B potential energy curve by absorption of two IR photons, thus ionizing the Rydberg electron from the B potential and launching a second nuclear wave packet in the $1s\sigma_g$ state of D_2^+ . When the nuclear wave packet reaches the outer classical turning point of the $1s\sigma_g$ potential energy curve (after $\sim$ 10 fs), absorption of another IR photon, from the same probe IR pulse, leads to an efficient coupling of the bound $1s\sigma_g$ and the dissociative $2p\sigma_u$ states of the ion, thus leading to dissociation into D + D^+ by a total absorption of 2 + 1 (i.e., three IR photons; Figure 6.3(A)). Through this two-step channel, the molecule dissociates with a kinetic energy release of $\sim$0.7 - 0.9 eV, typical for a bond softening process.

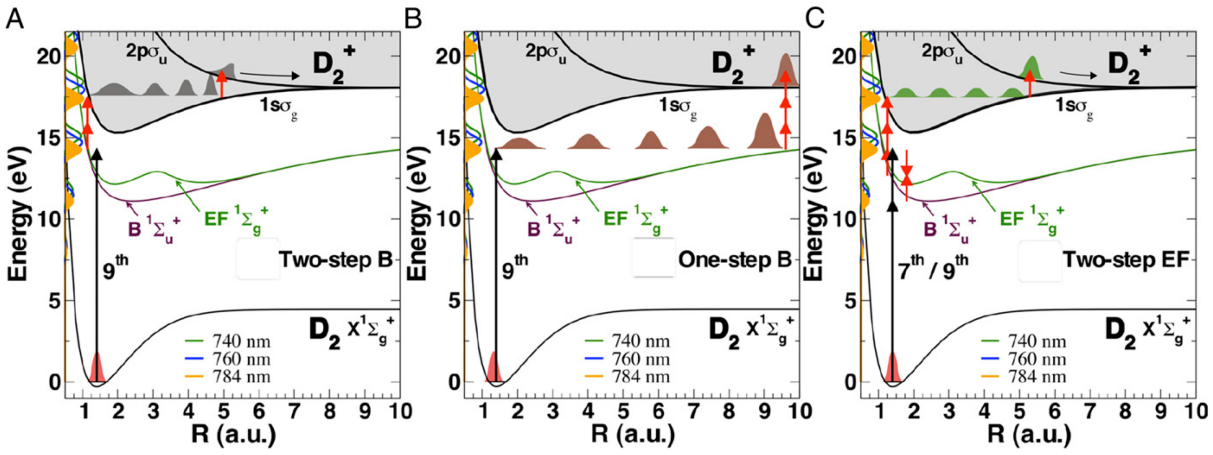

Figure 6.3: Combined coherent control of electronic and nuclear wavepacket dynamics on longer timescales. (a) Two-step B mechanism (D^+ high kinetic energy). (b) One-step B mechanism (D^+ low kinetic energy). (c) Two-step EF mechanism (D^+ high kinetic energy). We also show the tuning range of the VUV harmonics on the y axis (effective driving laser wavelengths of 784 nm, 760 nm, and 740 nm).

In the one-step B case, shown in Figure 6.3(B), the neutral D_2^* molecule first stretches to internuclear distances well beyond 9 a.u., which results in an increase of the effective ionization potential. At the instant the nuclear wave packet reaches the outer classical turning point of the B potential, the ionization of the molecule requires absorption of three IR photons. Through this

channel, the nuclear wave packet is directly coupled to the $2p\sigma_u$ dissociative continuum and the molecule dissociates with lower KER compared with the two-step B case. Due to the absorption of an extra IR photon at the outer turning point, a modulation of the ionization probability is expected as the excited molecule vibrates in the B potential. Finally, in the two-step EF case, shown in Figure 6.3(C), the nuclear wave packet launched by two-photon absorption ($7\omega + \omega$ and $9\omega - \omega$) is probed in the inner classical turning point of the EF potential energy curve by absorption of three IR photons, which generates a nuclear wave packet in the $1s\sigma_g$ potential, but with smaller probability compared with the two-step B case because the probability of observing this channel corresponds to a sequential absorption of 3 + 1 IR photons.

6.5 Nuclear Wavepacket Dynamics

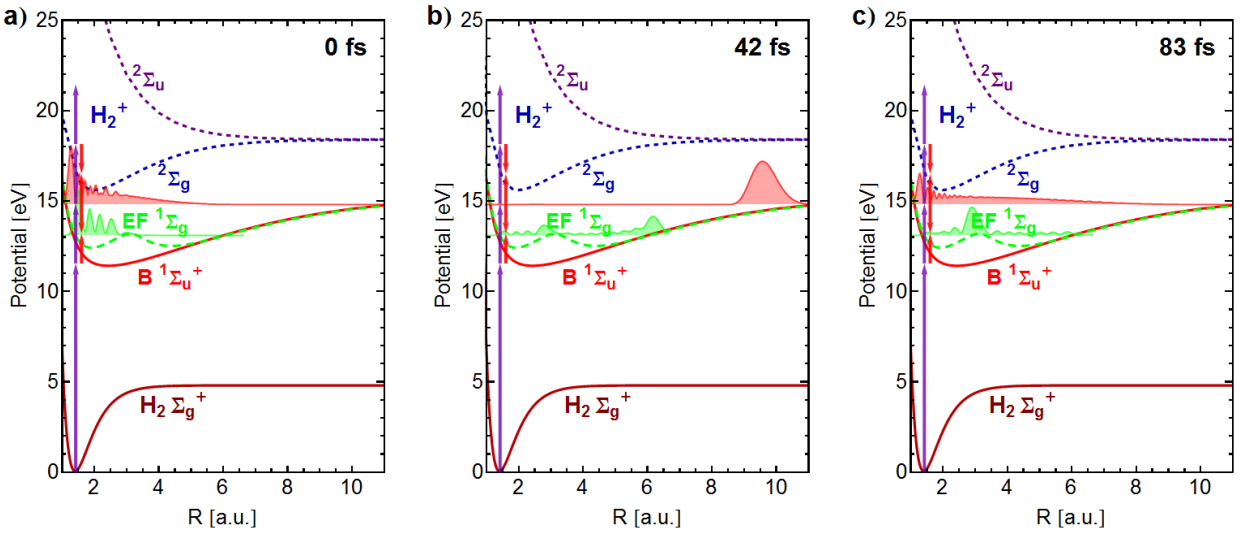

Figure 6.4: Theoretical calculations for the relevant potential energy curves show are coherent nuclear wavepacket as proceeds through approximated one oscillation in the B potential. Also shown is the wavepacket in the EF double well potential. Part (a) shows the initial excitation from the VUV harmonics. After ~45 fs the wavepacket in the B potential hits a clear outer turning point, as shown in part (b). After ~83 fs the wavepacket returns to the Franck-Condon region, as shown in part (c). This same oscillation is clearly shown in the experimental results.

Figure 6.4 shows the evolution of a calculated coherently excited nuclear wavepacket as it is populated in and the evolves along the B potential. Because of the ability to capture elec-

tronic and nuclear information in coincidence we can understand how shifting the pump wavelength changes the nuclear vibrations. Also shown in the same figure is the theoretical calculation for the wavepacket in the EF potential.

6.5.1 Fourier Analysis

Figure 6.5 validates the rich opportunities for state-selective, coherent excitation of multiple nuclear wavepacket dynamics of neutrally excited D_2, as well as a possibility of controlling bond breaking and dissociation through the pathways illustrated in Figure 6.3. Figure 6.5(A) plots the experimental D^+ KER as a function of the pump-probe delay, whereas Figure 6.5(D) plots the corresponding 2D Fourier transform (FT). One can clearly see oscillation periods of ∼83 fs and ∼58 fs at a D^+ KER of 0.7 - 0.9 eV, corresponding to the vibrational wave packets in the B and EF states, respectively, that are obtained through the two-step B and two-step EF mechanisms. The larger probability of the one-step B channel vs. the two-step EF channel (Figure 6.5(D)), confirms the three vs. four IR photon absorption mechanisms. Moreover, Figure 6.5(A) shows that the two-step B channel (high KER) has a larger probability than the one-step B channel (low KER), due to a lower effective ionization potential of the excited molecule at shorter internuclear separation. Figure 6.5(A) also shows that the two-step B and the one-step B channels are dephased, because the nuclear wave packet is probed at different times in those channels; this allows for steering of a desired dissociative route by precisely timing the second IR laser pulse as the neutral molecule vibrates.

As seen in Figure 6.1, to reach the outer turning point of the double-well EF potential and the vibrational period of ∼58 fs, the nuclear wave packet needs to tunnel through the potential barrier, which decreases the probability of observing the EF nuclear wave packet dynamics. The calculations nicely confirm the observed periodicities of these multiple nuclear wave packet dynamics in D_2 (Figure 6.5(G) and (H)). To model the dynamics of D_2 on femtosecond timescales, we first solved the TDSE to calculate the excitation probabilities, and then propagated the corresponding nuclear wave packets in the given D_2^* potentials (see the SI Text for more detail on how the

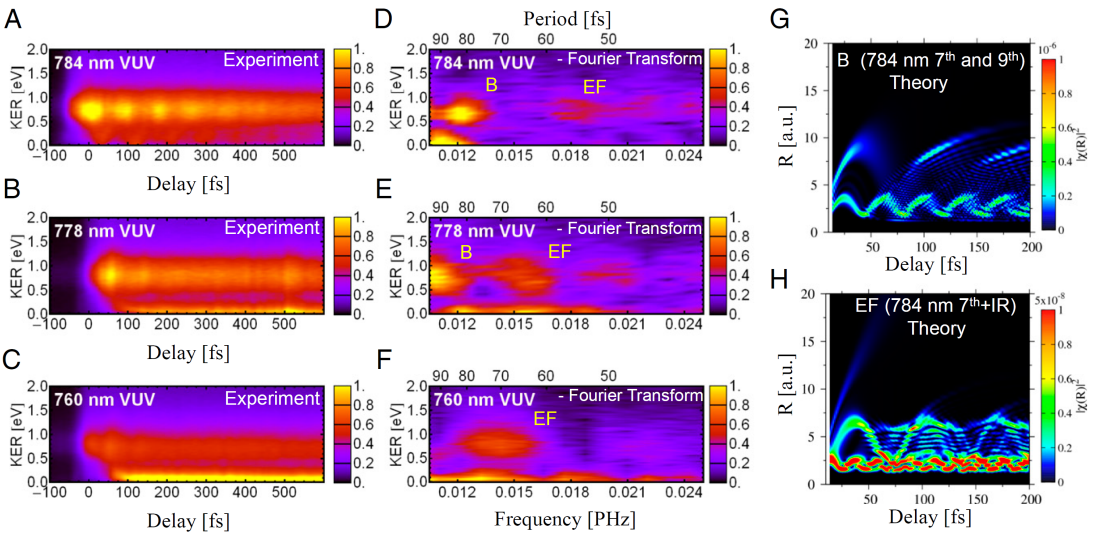

Figure 6.5: Controlling the dissociation channels by tuning the photon energy and through nuclear wave packet dynamics. (AC) D^+ kinetic energy release resulting from dissociation using three different VUV frequency combs that can be tuned to excite different D_2^* electronic and vibrational states. (DF) Corresponding 2D Fourier transforms of the D^+ kinetic energy releases. (G) Calculated free evolution of the nuclear wave packets generated by the combined VUV + IR pulses in the B potential energy surface. (H) The same for the EF potential energy surface.

calculations were done). For example, Figure 6.5(G) clearly shows how the EF nuclear wave packet starts reflecting and tunneling through the inner barrier at about R = 3 a.u. and 10 fs after the excitation. We also see that the nuclear wave packet tunnels with ∼20% probability compared with the main wave packet motion occurring in the inner well of the EF double-potential well. Moreover, the other striking feature of this calculation starts at ∼45 fs, when the nuclear wave packet in the inner well tunnels through the inner barrier for the second time and meets the outer-well nuclear wave packet on its way back from the outer classical turning point. The interference of the different nuclear wave packets is clearly visible from 45 fs onward. As the time evolves, multiple reflections/tunneling events from both sides of the inner barrier and the interferences of the nuclear wave packet in the EF potential are responsible for the fast decoherence of the EF nuclear wave packet.

Finally, by blue-shifting the VUV harmonic wavelengths to effective driving wavelengths of

778 nm and 760 nm (while keeping the IR wavelength fixed at 784 nm), we can control the relative population of the different neutrally excited states of D_2. Figure 6.5(B) and (C) show the KER spectra as a function of pump–probe time delay, and Figure 6.5(E) and (F) plot the corresponding 2D Fourier transforms. Two striking features are apparent. First, by slightly increasing the energies of the seventh and ninth harmonics, the vibration periods in the B and EF potentials simultaneously increase due to excitation to higher vibrational levels in the Franck-Condon region. Second, the relative strength of the one-step EF channel increases compared with the two-step B channel. The latter feature can be explained as follows. As seen in Figure 6.1 and Figure 6.3(C), simultaneous absorption of $7\omega + \omega$ and $9\omega - \omega$ creates a nuclear wave packet that can tunnel through the inner potential barrier (located at R = 3.5 a.u.) of the double-well EF potential. By slightly increasing the energy of the seventh harmonic, the tunneling process becomes more probable, thus increasing the nuclear wave packet density that vibrates with longer periods; this increases the relative visibility of the two-step EF channel with respect to the two-step B channel. For an effective driving wavelength of 760 nm, higher vibration levels of the EF potential are excited, allowing the nuclear wave packet to propagate freely above the inner barrier, moving along the EF potential energy curve with a vibrational period that is now close to that observed in the B state.

6.5.2 Visualization of Wavepacket Coherence

Figures 6.6 and 6.7 show experimental results combined with theoretical simulations. Shown in each Figure are momentum distribution at different times combined with the overall KER spectrum. One can recreate the nuclear wavepacket motion in a much complete view of the process because of the ability to filter on counts coming from the dissociation channel. Additionally, with theoretical simulations we can see the evolution of the coherent wavepacket as it is initially populated in the Franck-Condon region, oscillates to a larger internuclear distance turning point, and comes back again. In this way, we accurately can produce a movie of the experimental and simulated nuclear dynamics.

Finally, the two-step B channel also disappears when excited by 760 nm VUV harmonics,

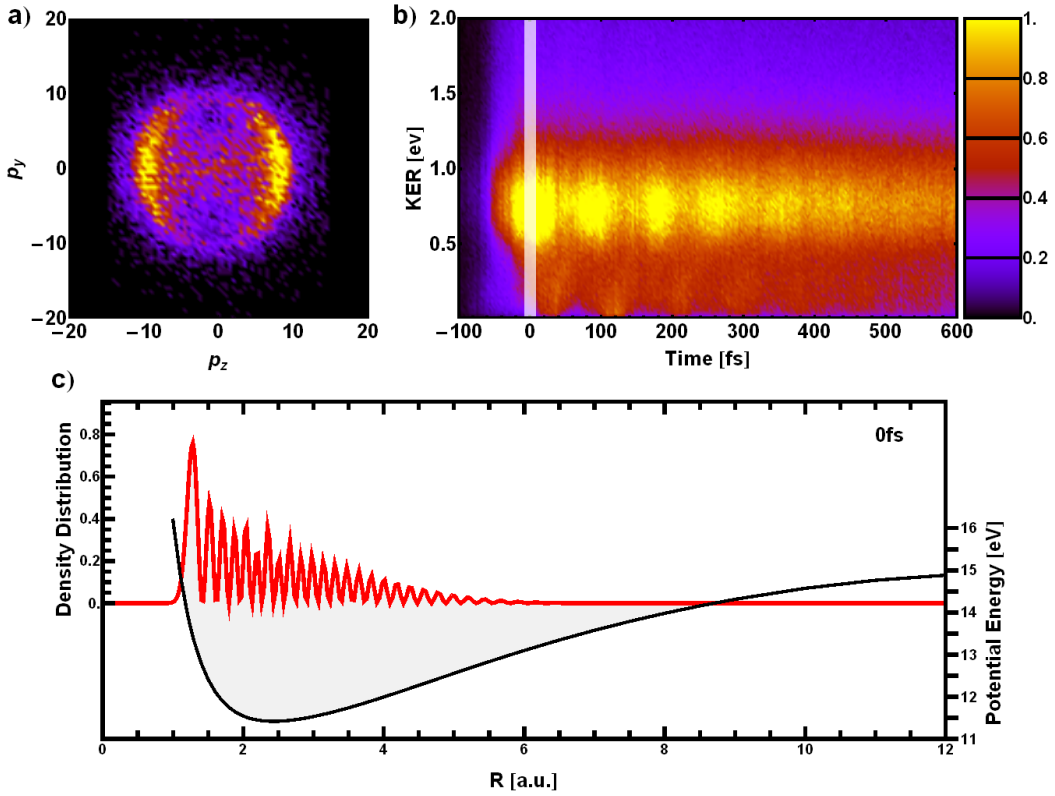

Figure 6.6: Upper left: Direct $D_2{}^+$ ion momenta shows a definite dissociation energy and a preferential to ionize along laser polarization. Upper right: KER for the scan highlighting the region around 0fs. Bottom: Theoretical simulation for wavepacket in the B potential. At 0fs, the placement of the wavepacket is due to the Franck-Condon region and the high KER results from the small internuclear distance.

because the coupling of the ground and B states dramatically decreases in the Franck-Condon region. In this case, the ninth harmonic excites higher electronic states. Thus, we show how tunable attosecond VUV radiation can be used to precisely control excitation of different electronic and vibrational states.

6.6 Electron Wavepacket Interferences

Figure 6.8 is an extended version of Figure 6.1 and shows in more detail ground and excited states of a deuterated hydrogen molecule (D_2 is the same as H_2). We also show the photoelectron, D^+, and $D_2{}^+$ yields, as well as kinetic energies of the electrons and the D^+ ions, for two different

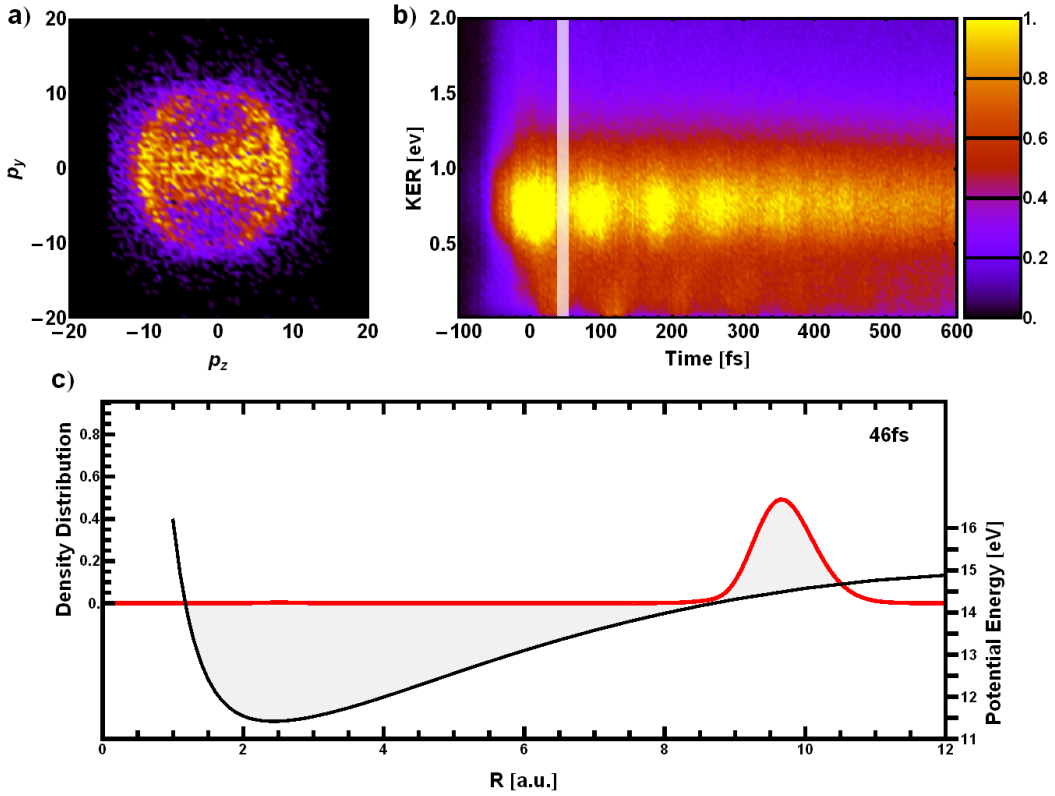

Figure 6.7: Upper left: Direct D_2^+ ion momenta shows a definite dissociation energy and a preferential to ionize along laser polarization. Upper right: KER for the scan highlighting the region around 46fs. Bottom: Theoretical simulation for wavepacket in the B potential. At 46fs, the wavepacket has traveled to a turning point with larger internuclear distance. This results in a lower KER but the wavepacket remain coherent.

central wavelengths of the VUV frequency comb. The wavelength (photon energy) of the VUV harmonics was fine-tuned while keeping the driving and probing IR wavelengths unchanged by adjusting the Xe pressure (and thus the HHG phase-matching) in the gas-filled waveguide. As the Xe pressure in the HHG waveguide was increased from 5 to 20 torr, the photoelectron energies that result from ionizing Ar by the VUV HHG comb also increased because it is possible to phase-match at slightly higher photon energies. This ability to fine-tune VUV photon energies allows us to distinguish between various excitation and control mechanisms.

Figure 6.8(E) shows how this phase-matching approach allows for fine control of the periodicity of the e^-/D_2^+ yields that changes from full to half-optical cycle duration of the IR laser

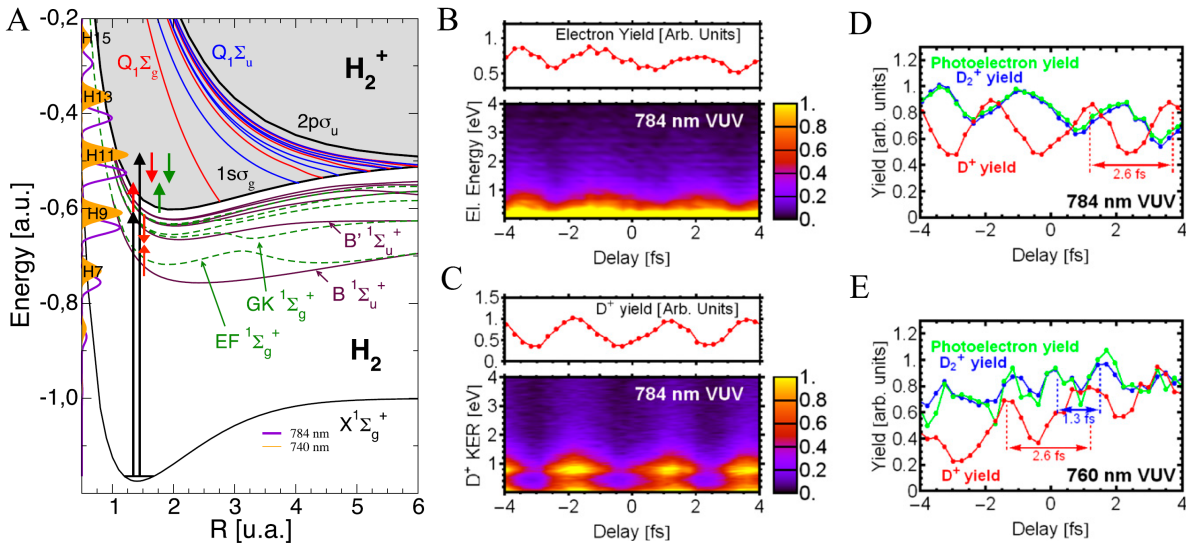

Figure 6.8: a) Detailed potential energy surfaces (PES) of the H_2 neutral and the H_2^+ ground and excited states (identical to those of D_2 and D_2^+). The red and green arrows represent driving and probing IR pulses, respectively. b) The photoelectron yield modulation results from the laser-induced interference of the electron wave packets created by the attosecond VUV frequency comb. The IR laser wavelength was 784 nm, while the VUV photons were 7ω, 9ω, 11ω, etc.. c) The D^+ dissociative yield modulation results from the intensity modulation of the interfering driving and probing IR pulses. d) A comparison of the D^+/e^- yields reveals that the ionization and dissociative dynamics are out of phase. e) By increasing the energy of the VUV photons, we change the electron-yield modulation period from full to half-optical-cycle periodicity.

field, as the harmonic energies were blue-shifted. We also see from Figure 6.8 that the periodicity of the D^+ yield does not depend on the VUV photon energy; this is expected because the excited molecule was ionized in the combined field of the two IR pump and probe pulses, which determines the periodicity observed in the ion yield. Thus, the phase of the D^+ oscillation provides a reference for the instantaneous value of the total electric field that drives the dissociation of the bound $1s\sigma_g$ nuclear wave packet, as shown in the high kinetic energy release channel, as well as the dissociation through the low KER channel. Though the high KER channel originates from a bond-softening process, which is routinely observed in many strong-field processes, the low KER channel originates from direct dissociation of D_2 as the highly excited Rydberg states were ionized at larger internuclear separations by the tail of the two IR pulses.

In conclusion, we present a powerful approach for using tunable VUV and IR attosecond pulse trains to coherently excite and control an outcome of a simple chemical reaction in a D_2 molecule. The interference of electronic wave packets excited by multicolor VUV and IR fields can be used to control excitation and ionization on attosecond timescales while maintaining good energy resolution and state selectivity. Selective bond-breaking is achieved by controlling the excitation wavelength as well as the time delay between the pump and probe pulses. We also observe and control the nuclear wave packet tunneling in the double-well EF potential. This demonstrates broad and unique capabilities for doing attosecond chemistry.

Chapter 7

Nitrous Oxide[1]

In this Chapter we discuss the ability to coherently control the dissociation pathway of N_2O. Such control of using laser light to not only direct molecular dynamics, but to extend the control to chemical reactions would be of tremendous impact. In the extreme ultraviolet (XUV) and soft x-ray regions of the spectrum, light-matter interaction is dominated by photoionization. In molecular systems, the sudden removal of an electron will initiate ultrafast electronic and nuclear dynamics in the residual molecular ion. A particularly interesting aspect of these dynamics is the correlated motions of electrons and nuclei, an understanding of which lies at the heart of chemistry. Here we use a few-femtosecond high harmonic pulse and a weak infrared (IR) laser pulse to initiate and probe the explosion of a triatomic N_2O^+ molecular ion in real time, in a regime dominated by coupled electron-electron and electron-nuclear dynamics. We also show that the branching ratio of bond breaking can be altered in the presence of the laser field.

7.1 Coherent Control of N_2O Dissociation

Recent advances in generating ultrafast soft x-ray pulses using high harmonic generation (HHG) [31], combined with advanced molecular imaging techniques [122], now make it possible to explore photoionization-driven [123] electron and nuclear dynamics in atoms [32, 124] and diatomic molecules [14, 68, 125] in real time for the first time. Owing to their greater mass, nuclear dynamics usually occur on much slower timescales than electron dynamics, and in the well-known

[1] The results of this chapter are in part based on "X. Zhou, P. Ranitovic, C. W. Hogle, J. H. D. Eland, H. C. Kapteyn, and M. M. Murnane, Proceedings of the National Academy of Sciences **8**, 3, 232 (2012)" [168].

Born-Oppenheimer approximation, electron and nuclear dynamics can be considered decoupled. However, for highly excited molecules, nuclear motion on strongly repulsive adiabatic potential energy surfaces can be very fast, so that electron and nuclear dynamics can occur on comparable timescales and be strongly coupled [95, 126–130]. For example, previous work has shown that autoionization and pre-dissociation are competing decay channels for super-excited neutral molecules (including valence singly excited Rydberg states [95, 126] and core-excited states [127]). However, such ultrafast non-Born-Oppenheimer dynamics on femtosecond timescales are largely unexplored in the case of molecular ions, where electron-electron correlation can also be important, owing to the lack of ultrashort XUV pulses.

7.1.1 Coulomb Explosion of N_2O

We probe and control the Coulomb explosion of a triatomic N_2O molecule after being ionized by a few-femtosecond XUV high harmonic pulse. N_2O is a simple linear triatomic molecule with an asymmetric bond. By ionizing/exciting N_2O with a few-femtosecond XUV pulse, we create a highly excited N_2O^{+*} state near the double ionization threshold (with continuous energy structure both below and above the double ionization threshold). The resultant decay dynamics of these excited molecular ions include two competing processes: (1) ultrafast dissociation into ion-neutral fragments with only one singly charged component; and (2) autoionization of super-excited states (that is, emission of a second electron) resulting in an N_2O^{2+} dication, which subsequently Coulomb explodes into two singly charged fragments, corresponding to breaking the N–N or N–O bond (that is, $N_2O^{2+} \rightarrow N_2{}^+ + O^+$ or $N_2O^{2+} \rightarrow N^+ + NO^+$). This competition between dissociation and autoionization has been suggested as the reason for the low double ionization quantum yield (ratio between double ionization and single ionization) of small molecular ions above the double ionization threshold [131].

We also show that the presence of a moderately intense linearly polarized infrared field can interrupt the neutral-ion dissociation channel and strongly enhance the double ionization yield, because the excited N_2O^{+*} cation can easily lose a second electron in the laser field. Furthermore,

the short duration of the double ionization enhancement transient, when the XUV and IR field are overlapped in time, reveals the timescale of ultrafast dissociation. Finally, with the addition of the IR field, breaking of the N–O bond can be enhanced more compared with breaking of the N–N bond, indicating the presence of laser-induced nonadiabatic multielectron dynamics. Our results thus demonstrate optical control [78, 132] of fragmentation products in highly excited molecular ions for the first time, in a regime dominated by coupled electron–electron and electron–nuclear dynamics.

The N_2O molecules from the supersonic jet are excited with sub-10 fs XUV pulses centred at a photon energy of 43 eV, which is above the 35.5 eV double ionization threshold of N_2O. This photon energy is close to the wavelength of the He(II) lamp (40.8 eV), allowing us to compare our data with previous work [128]. In contrast to our previous studies of ionization dynamics in N_2 and O_2 diatomics [14, 68], there is no long-lived metastable N_2O^{2+} that can survive the flight time to reach the detector ($\sim$10 μs); because of a shallow potential well in the Franck–Condon region. (The lifetime of metastable N_2O^{2+} has been determined to be less than 400 ns [133]). Because the threshold for three-body dissociation into two charged atomic ions is barely accessible with our 43 eV photon energy [134], double ionization mainly results in two two-body Coulomb explosion pathways:

$$\begin{aligned} &\text{Channel 1: } N_2O^{2+} \rightarrow {N_2}^+ + O^+ \\ &\text{Channel 2: } N_2O^{2+} \rightarrow N^+ + NO^+ \end{aligned} \tag{7.1}$$

7.1.2 Photoion-Photoion Coincidence

The recorded photoion-photoion coincidence (PIPICO) spectrum when N_2O is irradiated with the XUV pulse alone is shown in Figure 7.1(a). A momentum conservation filter between the two charged fragments is used to extract the counts corresponding to these two distinct Coulomb exploding channels from the background. In Figure 7.1(b),(c), we plot the filtered PIPICO spectrum of channels (1) and (2). The branching ratio between these two Coulomb explosion pathways is

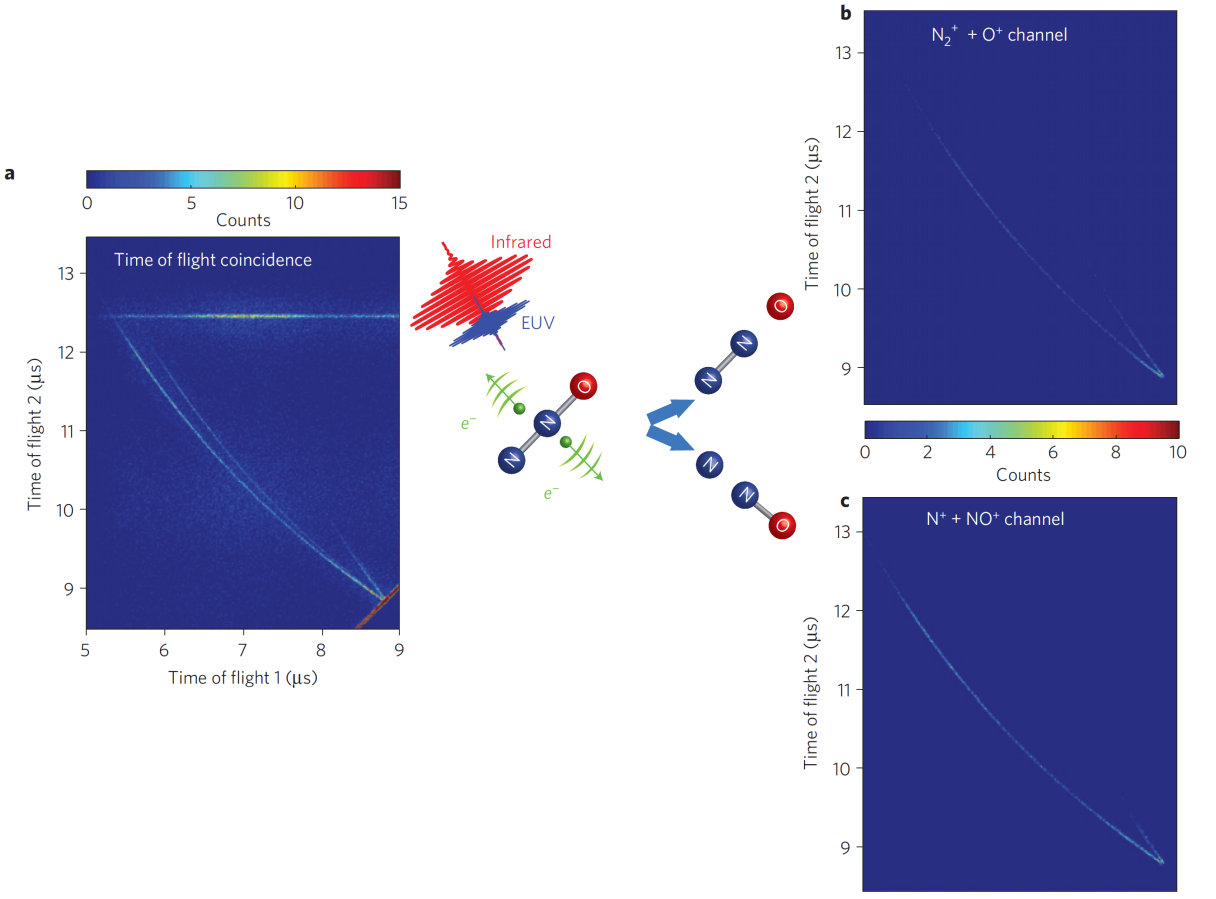

Figure 7.1: Illustration of double ionization of N_2O and subsequent two-body fragmentation. (a) PIPICO spectrum of N_2O^{2+} fragmentation using XUV pulse alone. (b) PIPICO spectrum filtered using momentum conservation for the fragmentation channel $N_2O^{2+} \rightarrow N_2^+ + O^+$. (c) PIPICO spectrum filtered for the fragmentation channel $N_2O^{2+} \rightarrow N^+ + NO^+$.

approximately 1 to 2.6, which agrees with previous studies using He(II) lamps and synchrotron radiation at similar photon energies. This ratio has been explained as the result of competition between the two fragmentation pathways on the potential energy surfaces of the first few N_2O^{2+} electronic states [135, 136].

Using a moderately intense infrared laser pulse (IR) to irradiate N_2O simultaneously with the XUV pulse, it is possible to probe the very fast nuclear dynamics initiated by the XUV pulse, and to control the branching ratio of channels (1) and (2). Figure 7.2(a) plots the ion yield for the two charge separation channels in the presence of both XUV and IR laser fields, as a function of

time delay between them. For the IR field, a 100 μJ pulse was focused to an intensity of $\sim 6 \times 10^{12}$ W/cm^2, ensuring that no N_2O^+ counts are observed from the IR field alone. When the IR pulse arrives before the XUV pulse, the relative yield between channels (1) and (2) is approximately the same as for XUV radiation alone, because the low intensity of our IR pulse does not excite the molecule. When the IR and XUV pulse coincide temporally, the yields of both channels are enhanced. The time-dependent yields of Figure 7.2 are fit with a convolution of a Gaussian function and an exponential function. The best fit corresponds to the convolution of a Gaussian function with a full-width at half-maximum (FWHM) of 41 fs, and an exponential function with decay constant of 15 fs and 19 fs for channels (1) and (2), respectively. Although the FWHM of the Gaussian function is longer than the exponential decay, the asymmetric shape of the trace can be clearly seen. The Gaussian pulse duration is only slightly shorter than the convolution of the 40 fs IR and 10 fs XUV pulses, indicating that only a few IR photons are involved in modulating the yield of the two-step sequential double ionization process.

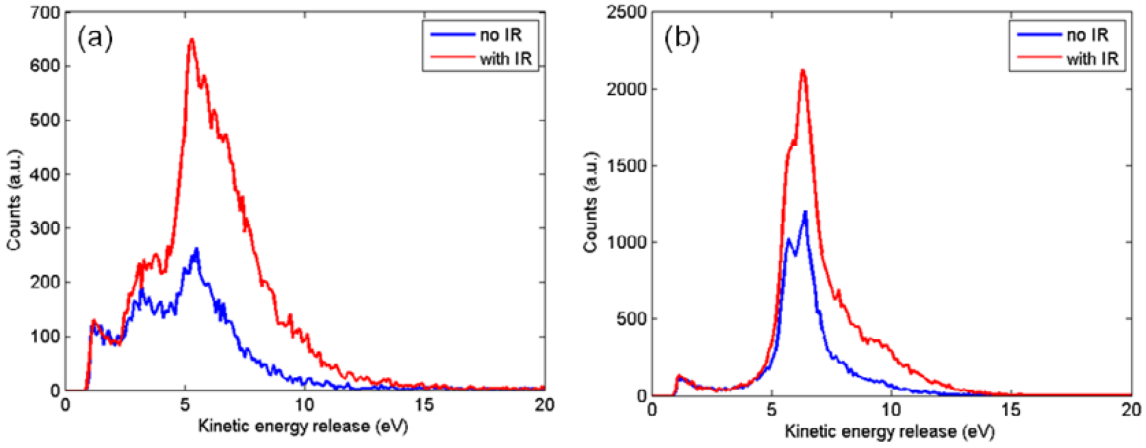

Figure 7.2: KER of the Coulomb explosion channel $N_2O^{2+} \rightarrow N_2^+ + O^+$ (left) and $N_2O^{2+} \rightarrow N^+ + NO^+$ (right) (effusive jet target). The enhancement is larger for the N–O bond-breaking channel, and consistent with the supersonic jet data.

7.1.3 Electronic configurations

The electronic configuration of the ground state of N_2O is $(1\sigma^2 2\sigma^2 3\sigma^2)(4\sigma^2 5\sigma^2)(6\sigma^2 1\pi^4 7\sigma^2 2\pi^4)$. The first three core-level molecular orbitals correspond to the 1s orbitals of the three constituent atoms. The $(4\sigma^2 5\sigma^2)(6\sigma^2 1\pi^4 7\sigma^2 2\pi^4)$ molecular orbitals are delocalized inner- and outer-valence electronic configurations respectively. Photoelectron spectroscopy and dipole (e,2e) spectroscopy studies can easily identify the four outer-valence ionized states $X^2\Pi(2\pi^{-1})$, $A^2\Sigma^+(7\sigma^{-1})$, $B^2\Pi(\pi^{-1})$ and $C^2\Sigma^+(6\sigma^{-1})$ as discrete sharp peaks, with corresponding binding energies of 12.9, 16.4, 18.2 and 20.1 eV, respectively [137]. However, for inner-valence ionization with binding energies between 20 and 40 eV, the photoelectron spectrum is broad, and it is no longer possible to associate a cation state with a one-hole configuration, which corresponds to removal of one electron from a neutral configuration with other electrons unaffected, in a one-to-one fashion. Generally speaking, the molecular orbital picture breaks down owing to electron-correlation-mediated mixing of inner-valence one-hole configurations ($4\sigma^{-1}$ and $5\sigma^{-1}$) and outer-valence shake-up two-hole-one-particle configurations [138,139], with two outer valence holes and another excited electron in the previous unoccupied molecular orbital, as shown in Figure 7.3(a). The intensity of the main lines ($4\sigma^{-1}$ and $5\sigma^{-1}$ with binding energies of 38 and 40 eV, respectively) redistributes to many lines corresponding to satellite states, and it is not possible to distinguish between them. The broad photoelectron spectrum between 30 and 40 eV (taken from previous photoelectron measurements [137]) is illustrated in Figure 7.3(b). Theoretical calculations have been able to reproduce the general features of these photoelectron and (e,2e) spectroscopy data [138,139], and also show that non-Rydberg type doubly excited electronic configurations give rise to most of these satellite lines. These excited states are major channels contributing to the IR field enhancement of the double ionization yield.

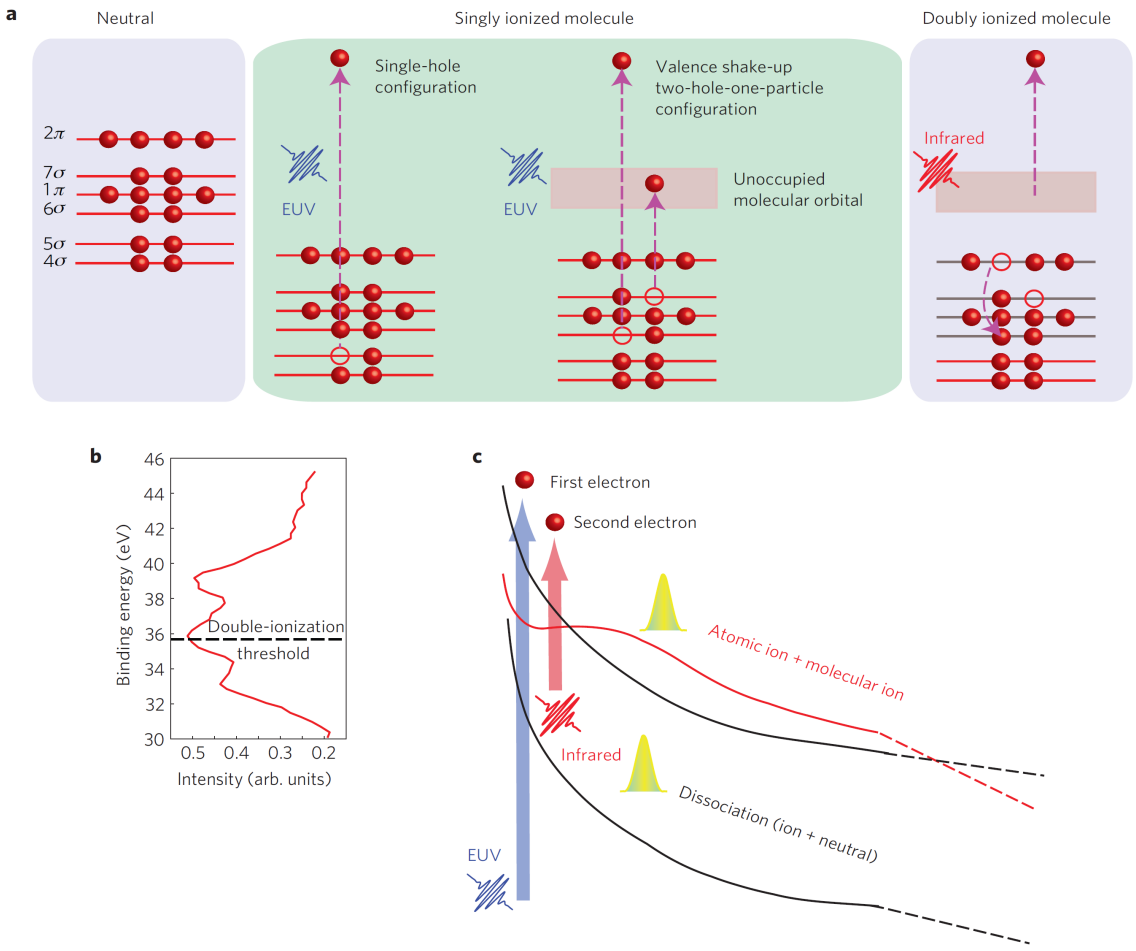

Figure 7.3: Illustration of the coupled electronnuclear ionization dynamics. (a) An illustration of possible electronic configuration changes during ionization of N_2O^{+*} in the presence of XUV and IR fields, involving multiple electron transitions. (b) Continuous electron spectrum of the inner-valence ionizing states measured at 60 eV photon energy. Reproduced from [137]. (c) Schematic representation of the N_2O^{+*} cation (black) and dication (red) potential energy curve along one bond stretch direction. The two major competing decay pathways of N_2O^{+*} are also labelled.

7.1.4 Ionization Yield and KER

The exponential decay of the ion yield signals in Figure 7.4(a) shows that IR field enhances double ionization through a two-step sequential process during which the molecule is first ionized by the XUV pulse, and the resulting cation N_2O^+ state is then further ionized by the IR pulse. This conclusion is supported by the fact that instantaneous IR and XUV (two photon) process

such as IR-assisted shake-off and knock-out of the second electron have small cross sections [43], and the densely distributed N_2O^{+*} potential energy surfaces provide many possible intermediate resonances. As mentioned in the main text, all of the N_2O^{2+} cations fragment into two ions before they can reach the detector. Therefore, the enhancement of the double ionization yield must come from the interaction of the IR pulse with intermediate states such as an excited neutral (N_2O^{**}) or cation state (N_2O^{+*}).

For doubly-excited neutral states above the double ionization threshold, subsequent dissociation and autoionization are both possible. Dissociation into two neutral atoms has been observed in fluorescence experiments for small molecules [140]. However, since our excitation photon energy is well above the first ionization threshold, the cross section for creating doubly-excited neutrals is small [141].

7.2 Dissociation Mechanisms

We can divide excited N_2O^{+*} states into two classes. The first class are molecular Rydberg states with a high n Rydberg electron and a vibrationally or electronically excited core. However these states follow similar potential energy surfaces to the lower lying states of N_2O^{2+} and converge to the same dissociation limits [142]. Moreover, Rydberg electrons can be easily ionized by the IR field, therefore any enhancement from these molecular Rydberg states should persist longer, at least for a few hundred femtoseconds. Therefore, Rydberg type N_2O^{+*} states are not a major contribution to the enhancement in double ionization near time zero. However, together with the doubly-excited neutrals, they could be responsible for the enhancement of double ionization at longer time delays after the transient at time zero, (which is a relatively small contribution to our data). The second class of N_2O^{+*} states are non-Rydberg type electronically excited states. From our data and theoretical calculations, these states are major contributors to the IR enhancement of the double ionization yield.

There are two major competing decay processes for XUV excited N_2O^{+*} states, as illustrated in Figure 7.3(c): molecular autoionization by ejecting a second electron ($N_2O^{+*} \rightarrow N_2O^{2+} + e^-$)

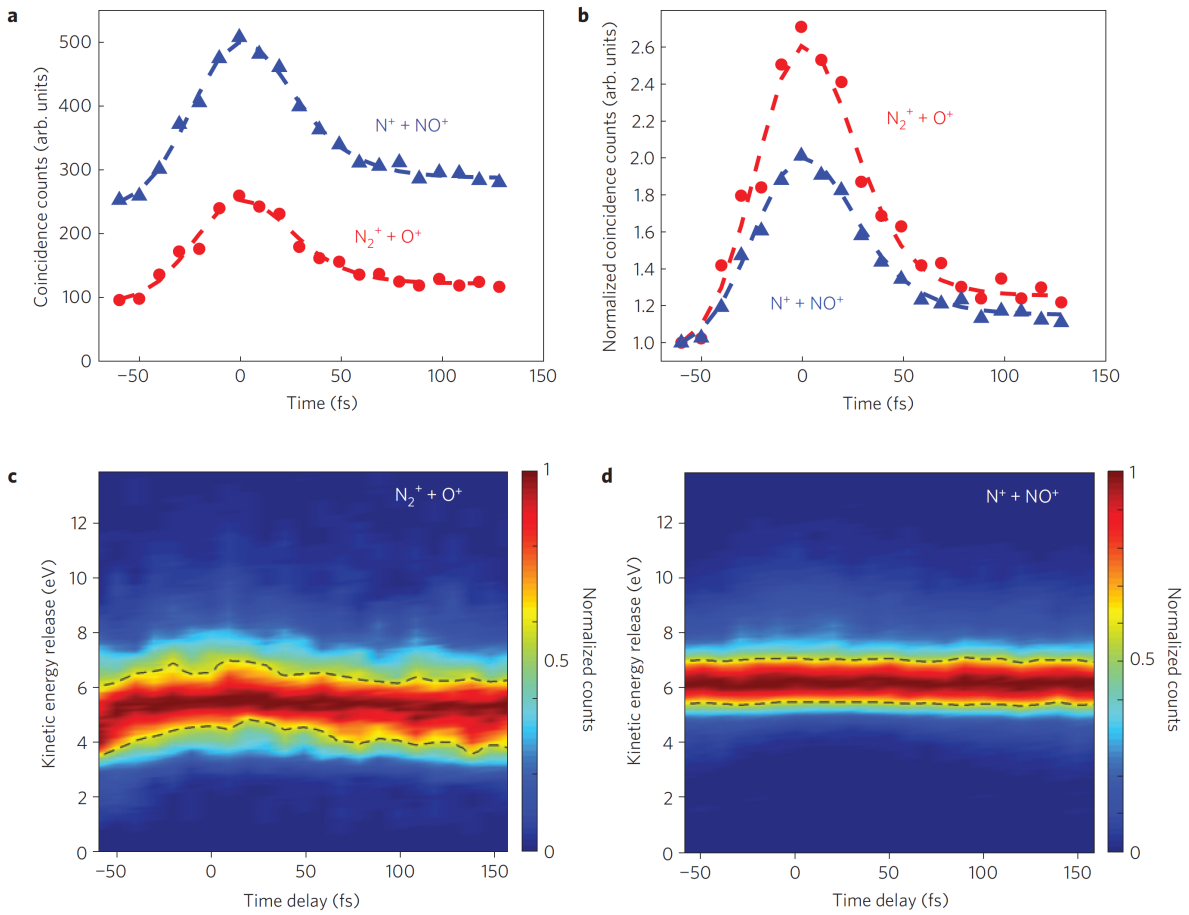

Figure 7.4: Time-dependent ionization yield and kinetic energy release of Coulomb explosion fragments. (a) Ionization yield as a function of time delay for the two double ionization channels along with a fit to a convolution of a Gaussian function and an exponential decay function. (b) The time-dependent ionization yield for both channels shown in (a) are normalized to the yield at -60 fs (IR before XUV), illustrating the different enhancements of the two channels. (c,d) Kinetic energy release as function of time delay between the XUV and IR for channels $N_2O^{2+} \rightarrow N_2^+ + O^+$ and $N_2O^{2+} \rightarrow N^+ + NO^+$ respectively. The dashed black contour line is to guide the eye to make the KER change for $N_2O^{2+} \rightarrow N_2^+ + O^+$ channel more visible.

accompanied by Coulomb explosion, or dissociation of the ion into a neutral fragment and a singly charged ion. Autoionization of N_2O^{+*} to low-lying electronic states of the doubly ionized molecule can only happen if the molecule is excited by photon energies above the double photoionization threshold (35.5 eV). N_2O^{+*} provides an interesting scenario because a portion of the XUV-excited state is above the double photoionization threshold of 35.5 eV and forms a super-excited molecular

ion, as shown in Figure 7.3(b). This situation is impossible for atoms and many small molecules, such as N_2, H_2O or CO. However, it is much more common in weakly-bound dimers, because the distribution of two holes on different atomic or molecular sites in dimers lowers the double ionization threshold. This can result in an autoionizing process called inter-molecular Coulomb decay (ICD), which is an extremely efficient process with decay times between a few femtoseconds and a few hundred femtoseconds [129, 130]. The inner-valence ionized cation states of dimer molecules are usually well above the dication potential energy surface, which makes ICD the dominant decay process. This will be discussed further in Chapter 8.

For super-excited N_2O^{+*}, the timescale of molecular autoionization ($N_2O^{+*} \rightarrow N_2O^{2+} + e^-$) varies with the electronic configurations. Non-Rydberg type electronically doubly excited configurations usually autoionize in a few femtoseconds [143]. However, in contrast to ICD, the dense adiabatic potential energy surfaces (calculated using the Born-Oppenheimer approximation) of these N_2O^{+*} are strongly repulsive, and can quickly drop below the potential energy surfaces of the lower lying dication states, thus reducing the probability of autoionization. If the rates of nuclear dissociation into a neutral fragment and a singly charged ion are comparable to the average electronic decay rates, competition between dissociation and autoionization is possible, as illustrated in Figure 7.3(c). The large number of potential energy surface intersections and fast nuclear motion lead to extreme non-Born-Oppenheimer dynamics, and prevent theoretical treatments such as a diabatic representation of strong non-adiabatic coupling at a conical intersection between two adiabatic potential energy surfaces.

The addition of a weak IR field can couple the excited molecular cation state to other states or dication continuum states via single or multiphoton transitions. For excited states below the double ionization threshold, normally energetically forbidden double ionization is made possible in the presence of an IR field. For excited states above the double ionization threshold, the branching ratio between autoionization and dissociation can be altered [144]. Because of the strong electron correlation in this region, the IR induced ionization process represents a laser-induced multielectron process, which from an energetic point of view is preferred over direct ionization of the most loosely-

bound electron. A schematic of this ionization process involving multiple electrons is illustrated in Figure 7.3(a).

In the Born-Oppenheimer approximation, autoionization is instantaneous (or at least much faster compared with nuclear motion), and all excited states above the double ionization threshold should autoionize. In this case, the enhancement of double ionization would result from the promotion of N_2O^{+*} population from below to above threshold. However, considering that the area of the photoelectron spectrum below the double ionization threshold is less than that above, as shown in Figure 7.3(b), this mechanism cannot explain the $\times 2$ enhancement in double ion yield we observe. Therefore, for the first time, we use a time-resolved measurement to reveal the competition between dissociation and autoionization in a highly excited molecular ion, and the breakdown of the Born-Oppenheimer approximation.

The 20 fs decay time of the double ionization enhancement transient indicates the timescale of ultrafast dissociation in excited N_2O^{+*} states. During this time, electronic excitation is converted into kinetic energy of the fragments through complicated electron-nuclear dynamics, which can be thought of as hopping between different adiabatic potential energy surfaces. At a certain point in this ultrafast dissociation process, the IR intensity used becomes less effective in ionizing the second electron owing to the increasing ionization potential [82]. Furthermore, the competition between autoionization and dissociation suggests that the cross-section and timescale for dissociation and autoionization must be comparable.

7.3 Selective Bond Breaking

It is also interesting to compare the dynamics of the two bond-breaking channels of N_2O^{2+} (that is, breaking the N–N bond or breaking the N–O bond), which might shed light on the laser-induced nonadiabatic multielectron dynamics. First, we notice in Figure 7.4(a) that the relative enhancements of the two bond-breaking channels by the IR laser are different. To emphasize this, we normalize the time-dependent yield of each channel by the yield in the presence of the XUV pulse alone, as shown in Figure 7.4(b). With the addition of the IR pulse, the less dominant channel

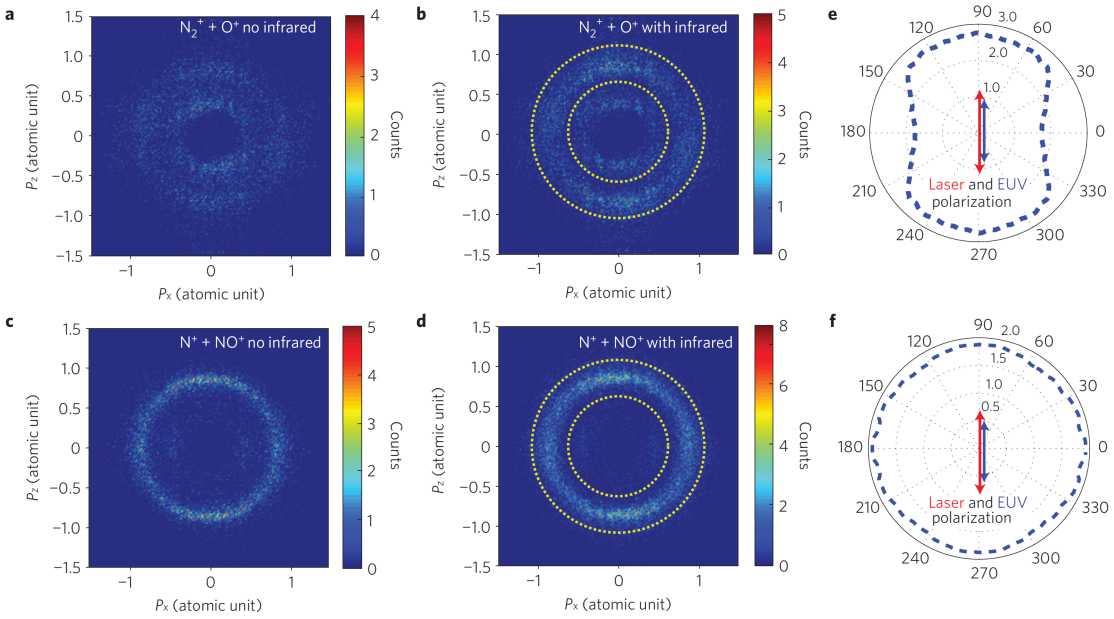

Figure 7.5: Momentum distribution of the Coulomb explosion fragments. (a,b) For the N_2^+ ion from Coulomb explosion with the IR pulse well before the XUV pulse (a), and with the two pulses temporally overlapped (b). (c,d) Similar to a and b, but for the NO^+ ion. The outer momentum ring structure from molecular double ionization is separated by dashed yellow lines from the time delayed autoionization in (b) and (d). The ratio of the integrated outer-momentum ring (direct double ionization) of N_2^+ in (b) and (a) are plotted in (e), and the ratio of the integrated outer-momentum ring (direct double ionization) of NO^+ in (d) and (c) are plotted in (f). The red and blue arrows in (e) and (f) show the direction of the laser and XUV polarization. These data are taken with an effusive jet.

(breaking the N–O bond) is enhanced more (∼2.6 times) compared with breaking the N–N bond (∼2 times). Therefore, the relative difference between the two channels is smaller in the presence of the IR field. Selective bond breaking is an interesting topic, which has been studied both in the context of single-photon weak-field ionization of core [145] and inner-valence levels [146], as well as in the context of multiphoton intense-field ionization [78,132]. Here, control is achieved by combining these two approaches through a transient intermediate resonance in a highly excited short-lived N_2O^{+*} state. Previous photoelectron-photoion coincidence studies [146] show that dissociation of highly excited N_2O^{+*} states in the binding energy region between 30 and 40 eV has a strong preference for the N–N bond-breaking channel, resulting in $N^+ + NO$ or $N + NO^+$ fragments. Therefore, it

is surprising that we observe a large enhancement in N–O bond breaking in the presence of the IR field, which is probably a signature of laser-induced multielectron dynamics. Nonresonant light dressing of the molecular potential could also play a role. In the absence of advanced theory, it is difficult to understand the detailed mechanism for how the IR field preferentially enhances one bond-breaking channel.

As the IR laser field interrupts the dissociation of N_2O^{+*} and promotes it to an N_2O^{2+} dication state, there should be a corresponding change in the kinetic energy release (KER, sum of the kinetic energy of the two fragments) of the fragments due to the difference in the potential energy surfaces of N_2O^{+*} and N_2O^{2+}. Figure 7.4(c),(d) plots the KER of both channels as a function of XUV-IR relative time delay, where the KER counts are normalized to the maximum for each time delay to show the shift of the KER more clearly. The KER peak for breaking the N–O bond is broader than the KER for breaking the N–N bond. The KER are centered at 5 and 6 eV respectively, which agrees with previous work [135]. At time zero, we observe a slight shift towards higher KER for breaking the N–O bond, whereas the KER for the N–N bond-breaking channel does not change. However, the observed KER changes for both channels are very small compared with what was observed previously for diatomic molecules [14, 68, 125]. The most likely explanation is that for triatomic molecules in a strongly-coupled non-Born-Oppenheimer regime, any further energy can be efficiently transferred into internal excitation of the molecular fragment species, instead of into kinetic energy of the fragments.

7.4 Angular Distribution of N_2O^{2+} fragments

Figure 7.5(a)-(d) plots the angular distribution of the ion fragments both with and without the IR field, for both bond-breaking channels. The angular distribution of the ion fragments is related to the symmetry of the initial and final electronic orbitals, and can show signatures of electronic configuration interaction. These data were taken using the effusive jet with much longer data acquisition times, at two fixed time delays between XUV and IR pulses, namely when the IR pulse arrives 200 fs before the XUV pulse, and when both pulses are overlapped in time. The former is

equivalent to irradiation by the XUV pulse alone. In the momentum distribution after excitation by the XUV pulse alone, the anisotropy in the angular distribution is clearly visible. The anisotropy of ion fragments from double ionization is not trivial to understand, because two electrons are involved [147]. Focusing on the IR enhancement of direct molecular double photoionization, Figure 7.5(e),(f) plots the angle-dependent IR enhancement of double photoionization by integrating the counts in the outer momentum ring along different angles. The enhancement of the $N^+ + NO^+$ channel is almost isotropic whereas the enhancement of the $N_2{}^+ + O^+$ channel favours the direction of the laser polarization.

As shown in Figure 7.5, for both channels there are two separate momentum rings. The outer momentum ring in Figure 7.5 corresponds to the major KER peak in Figure 7.2, while the inner momentum ring in Figure 7.5 corresponds to the low KER peak shown in Figure 7.2. Although a full four-body (two electrons plus two ion fragments) momentum map is not possible with our count rates, we can still assign the small momentum ring counts as due to time-delayed autoionization, and the larger momentum ring as molecular double ionization, according to previous studies on CO and H_2O [125, 148].

7.5 Autoionization Pathway

In the case of time-delayed autoionization, some of the dissociating potential energy surfaces of N_2O^{+*} will end up above the dissociation limit of the dication. In this case, the excited atomic or molecular species such as N^*, O^*, $N_2{}^*$ and NO^*, will proceed to autoionize. For N_2O, the presence of time-delayed atomic autoionization has been confirmed by the atomic-like autoionization lines of N^* and O^* atomic species presented in previous photoion-photoelectron-photoelectron triple coincidence measurements [128]. However, $N_2{}^*$ and NO^* autoionization have not been isolated this way because of the broad autoionization lines. Time-delayed autoionization processes can even happen for excitation below the double ionization threshold, as low as 34 eV [128]. Using an effusive jet, we have more counts with low KER than for the case of supersonic jet data for both channels, which is probably due to the increased statistics and a slight red shift of the XUV spectrum

(about 0.5eV), which could increase time-delayed autoionization. Apparently autoionization of O^* or $N_2{}^*$ is more prominent than autoionization of N^* or NO^*. The angular distribution of the small momentum ring related to N^* or NO^* autoionization channel is oriented perpendicular to the laser polarization direction, while the orientation of the O^* or $N_2{}^*$ autoionization channels and direct double ionization channels are along the direction of the laser polarization.

Past work has shown that atomic autoionization is the dominant double ionization mechanism for O_2 even above the double ionization threshold. A time-resolved XUV pump IR probe experiment confirmed that autoionization of O^* does not happen until a few hundred femtoseconds after the XUV pulse [68]. However, the time delayed autoionization is not our focus in this paper and it is minor channel for the enhanced double ionization of N_2O by IR: when the IR pulse is applied near time zero, the autoionization channels remain almost unchanged, while the direct molecular double ionization channels are strongly enhanced, which is obvious in the energy-dependent KER enhancement shown in Figure 7.2.

To fully understand the observed dynamic evolution of N_2O^{+*}, with or without the presence of the IR field, will require more advanced theory. However, the strong electron–electron and electron–nuclear coupling make reliable quantum chemistry calculations very challenging. Further experiments using shorter duration XUV and IR pulses could measure these timescales more precisely. With photoelectron or photoelectron-photoion coincidence measurements, it should be possible to extract valuable information about laser-induced electronic reorganization from the angular distribution of electrons.

In summary, few-femtosecond XUV pulses can produce highly-excited inner-valence ionized N_2O^{+*} molecular ions which rapidly dissociate or autoionize in $\sim$20 fs. Using moderate intensity IR fields, surprisingly it is possible to enhance and to change the branching ratios for selectively breaking the N–N or N–O bond. The short timescale over which enhancement is possible reveals the competition between fast dissociation and autoionization processes in N_2O^{+*}, and highlights the role of non-Born-Oppenheimer strongly-coupled dynamics. The ability to control the branching ratio for bond breaking provides evidence of laser-induced multielectron processes. The observed

competition between dissociation and emission of a second electron is relevant to many physical processes with strongly coupled electron and nuclear dynamics.

Chapter 8

Complex Systems

Because of COLTRIMS's ability to measure the momenta of both electrons and ions in coincidence, much of the previous work has focused on atomic and diatomic experiments where the complete system can be best be theoretically modeled [14, 23, 42, 43, 63, 68, 82]. Applying similar techniques to larger and more complicated molecules allows for the exploration into a wider area of physical chemistry. As discussed in Chapter 7, even a triatomic system can provide many, often unexpected, complexities. Both molecules examined here, ethylene and ozone, have enormous impact on better understanding important processes like the chemical reaction responsible for vision and allowing for more accurate atmospheric models relating to climate change as well as many other applications. Additionally, the argon dimer, while a diatomic system, provides a useful system to study because of the weak bonding and simpler electronic structure.

8.1 C_2D_4 isomerization

The molecule rhodopsin has long been known to be the primary photochemical receptor responsible for the process that allows for vision [149]. Nonradiative relaxation through a conical intersection allows for the ultrafast transfer of light into chemical energy but the details of the process are not well understood [150]. This process is both extremely efficient with its energy conversion as well as its response time, having dynamics on ultrafast timescales. The isomerization of the all-trans form in rhodopsin was identified as the main photochemical event in vision, involving a conical intersection between the potential energy surfaces of the ground and excited electronic

states [151, 152]. A conical intersection is the non-adiabatic coupling between two potential energy surfaces. At the these intersections, the Born-Oppenheimer approximation breaks down and the electronic and nuclear changes are highly coupled. As with other experiments previously discussed, the nature of these dynamics presents a challenging experimental environment where probing the exciting state necessary to access a conical intersection requires precise spectral control but we must still have time resolution to probe the reacting molecule which changes on an ultrafast timescale.

The photoisomerization of retinal rhodopsin can be effectively modeled by the twist and stretch of a carbon double bond [153]. The simplest molecule with a carbon double bond is ethylene (C_2H_4), yet even this "simple" molecule presents numerous experimental and theoretical complexities. Ethylene's first absorption band is centered at 165 nm [154] making the 5th harmonic of the Ti:sapphire laser an ideal pump for this system. This band is dominated by a $\pi \rightarrow \pi^*$ transition where in this excited state the lowest potential energy configuration is no longer planar [155, 156]. Using nomenclature from Mulliken, this is the V state (for valence) and is shown schematically in Figure 8.1.

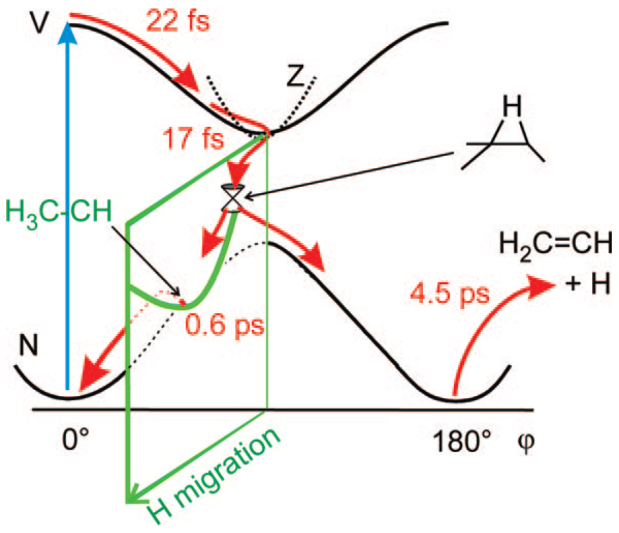

Figure 8.1: Potentials and dynamics of C_2H_4 adapted from [157], indicating also hydrogen migration (perpendicular to the drawing plane) and the displacement of the conical intersection. ϕ is the C-C torsion angle.

Some calculations predict that one of the major pathways in which the molecule relaxes to the ground state is through an ethylidene configuration ($HCCH_3$), where one of the hydrogen atoms has migrated across the carbon-carbon bond [157]. This provides an additional coordinate for relaxation down to the ground state. The ethylidene configuration is predicted to be followed by a H_2 stretch leading to the elimination of neutral or ionized molecular hydrogen [154, 158–161]. Because of this, understanding the asymmetric dissociations of ethylene is an incredibly important part to better understand this type of conical intersection.

We use a pump-probe geometry with VUV photons as a pump pulse and a delayed IR pulse to probe. With experimental conditions similar to what was discussed in Chapter 6 we know we have signals from 7th, 9th, and 11th harmonic energies. We also believe that the phase matching condition and reflectivity of the mirrors allow for the 5th harmonic as well. We also allow a small intensity of the high harmonic driving IR intensity to copropagate. This driving IR field is locked in phase to the high harmonics and provides a reference for the probing IR field. Having established this a technique on simpler systems [23], we wish to show the ability to induce and control the outcome of a chemical reaction on an attosecond timescale. We focus mainly on the dissociation pathways involving $D_2{}^+$, $C_2D_2{}^+$ and $C_2D_4{}^+$, however as shown in Figure 8.2, many other ions are present.

Figure 8.2 shows the time-of-flight spectrum for C_2D_4 irradiated by a VUV pulse train and IR pulse temporally overlapped. As expected with a strong-field IR pulse as well as with low order harmonics, a primary signals come from the singly ionized parent ion, $C_2D_4{}^+$. There is also a strong $C_2D_2{}^+$ signal, but which is sensitive to the VUV pulse.

Additionally, there is a detectable $C_2D_4 \rightarrow C_2D_2 + D_2{}^+ + e^-$ pathway less probable than $C_2D_4 \rightarrow C_2D_2{}^+ + D_2 + e^-$. The experiment was performed with the effusive gas jet. An unexpected result was the presence of the ethylene dimer (C_4D_8) which presents an exciting system to test with future experiments. With the effusive gas jet the ethylene molecules are emitted with more thermal energy than with the supersonic jet. Typically the atoms or molecules must lose most of this thermal energy to allow for a measurable level of dimers to be present.

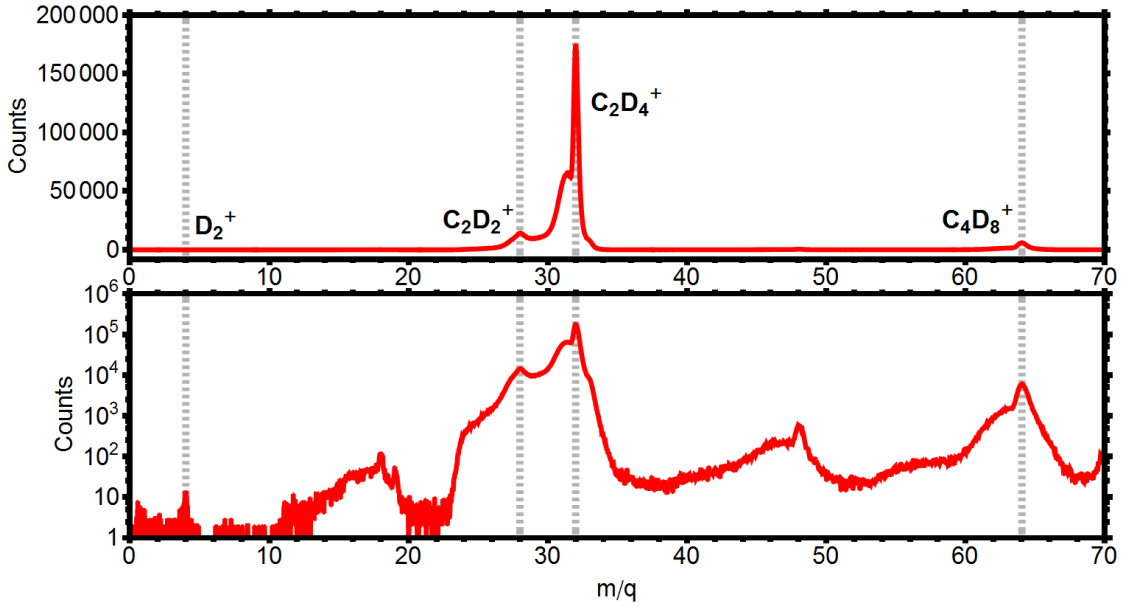

Figure 8.2: C_2D_4 time-of-flight spectrum, plotted on both linear and logarithmic scales. The parent ion undergoes many different fragmentation pathways. The single ionization ($C_2D_4^+$) allows for comparison against the dissociation pathways ($C_2D_2^+$ and D_2^+).

Experiments were performed with both femtosecond and suboptical cycle resolution. Figure 8.3 shows the ionization yields for the $C_2D_4^+$, $C_2D_2^+$, D_2^+ ions a function of pump-probe delay. The $C_2D_2^+$ and D_2^+ yields show enhancement with IR overlap; the $C_2D_4^+$ peaks 40 fs later. Previous studies have seen a maximum fragmentation yield attributed to ethylidene isomerization later at approximately 80 fs and model the isomerization time at approximately 50 fs [154, 159]. The $C_2D_2^+$ enhancement at 40 fs is reproduced by scans with a larger step size. This enhancement of the $C_2D_2^+$ yield is believed to take place after the D migration allowing for the elimination of D_2. This measurement could be improved with a shorter probing pulse envelope; however, there is a clear response before what has been previously measured in association with the isomerization [159].

Figure 8.4 shows a zoomed in view of the ion yields at four different regions near pump-probe overlap. While each ion yield appears to oscillate with the same full optical cycle oscillation the yields do not oscillate in phase with one another. The difference in the enhancement of each ionization channel cannot be simply explained by the instantaneous strength of the electric field

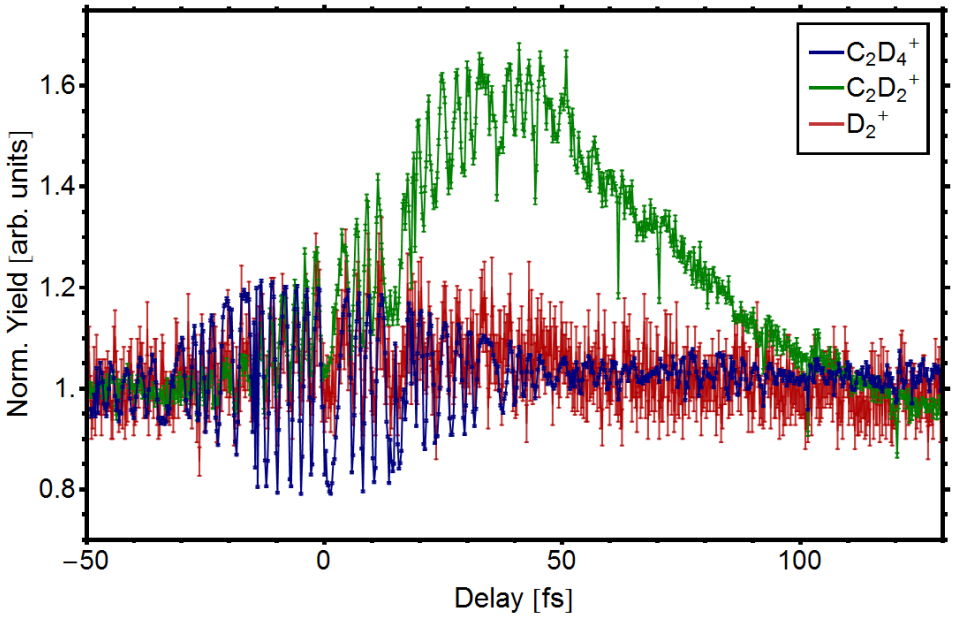

Figure 8.3: Pump-probe spectrum of C_2D_4 fragmentation yields. Positive delays refer to the VUV pulse train preceding the IR pulse. The ionization yield is enhanced around 0 fs for $C_2D_4{}^+$ and $D_2{}^+$ but the enhancement of $C_2D_2{}^+$ is delayed ∼40 fs. The attosecond scale resolution is shown above as the yields oscillate with a full optical cycle periodicity.

due to the IR pulse. Figure 8.4 also shows sinusoidal fits for the experimental yields, each plotted with the same amplitude. The fits clearly show a shift of the phase of the $C_2D_2{}^+$ and $D_2{}^+$ yields relative to $C_2D_4{}^+$ over the region where the pulses are overlapped.

The delay between the $C_2D_2{}^+$ and $C_2D_4{}^+$ changes from 90 attoseconds to 370 attoseconds. The interferometric stability limits the ability to see how the transition occurs over the scan but the change is definite. Further theoretical simulations must be done to fully understand how this difference in ionization yield relates to the changing molecular structure. This level of analysis over measuring yields on femtosecond timescales moves closer to the factors for inducing and controlling this and similar reactions.

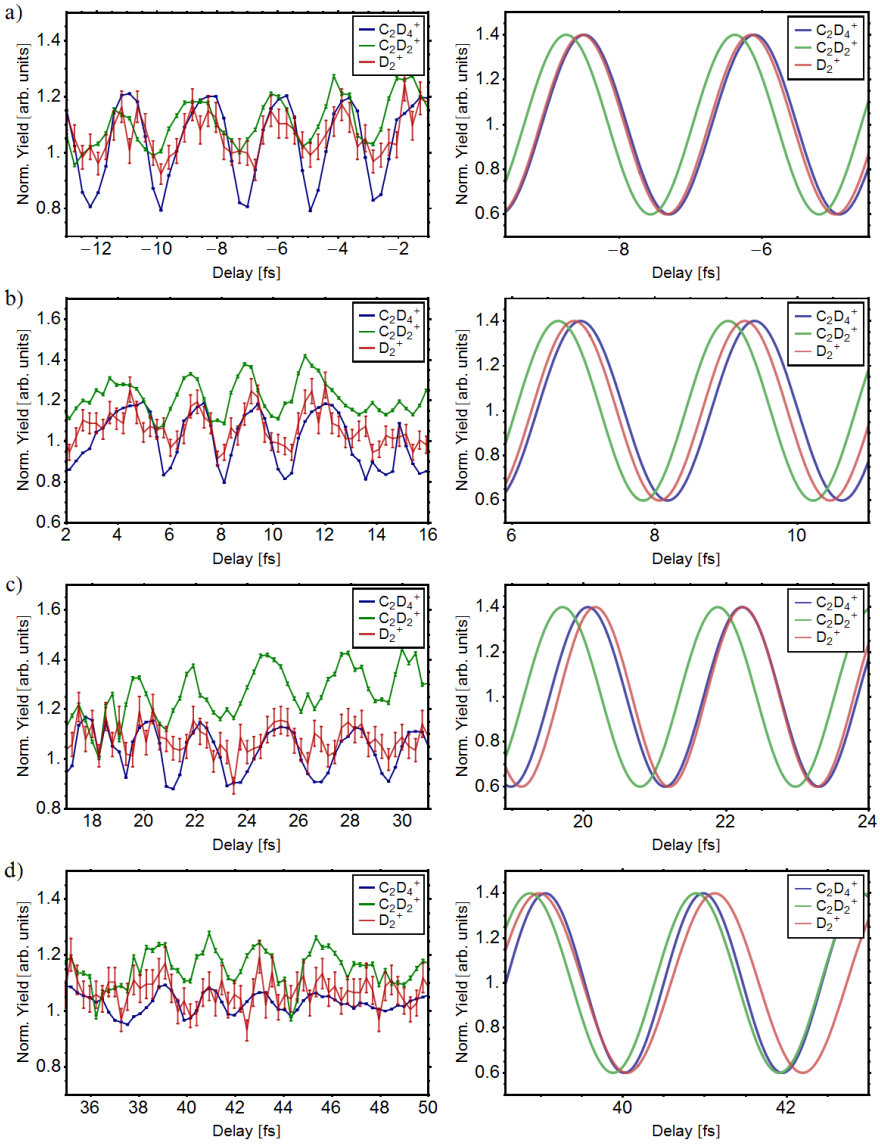

Figure 8.4: Fits for four different overlap regions of C_2D_4 fragments. A sinusoidal fit was performed in four different regions relative to pump-probe time zero. These fits are plotted on the right side for each region with normalized amplitude. The experimental yields have been shifted here for comparison purposes.

8.2 Argon dimer Inter-Coulombic Decay

Noble gas dimers are bound by a weak van der Waals potential which results in a substantially larger internuclear separation than with covalently bound diatomics. Therefore, while having some molecular-like properties, the electrons remain more centered at each nucleus. Photoionization of

dimers with both XUV and strong-field ionization should probe the electronic properties in such a way to see both localized structure as well as shared electronic behavior. Complete understanding of intramolecular charge transfer remains a challenge [162], and systems like argon dimer, which exhibit related processes in a simplified structure. The inner valence states will be ionized with a high harmonic photon of sufficient energy and the strong-field will look primarily at the outer-most shared electrons. As discussed in Chapter 5, changing internuclear spacing dramatically affects the kinetic energy release (KER) which provides information about the changing molecular orbitals. The simplified bonding of dimers makes them a preferable system to study similar electronic structure changes.

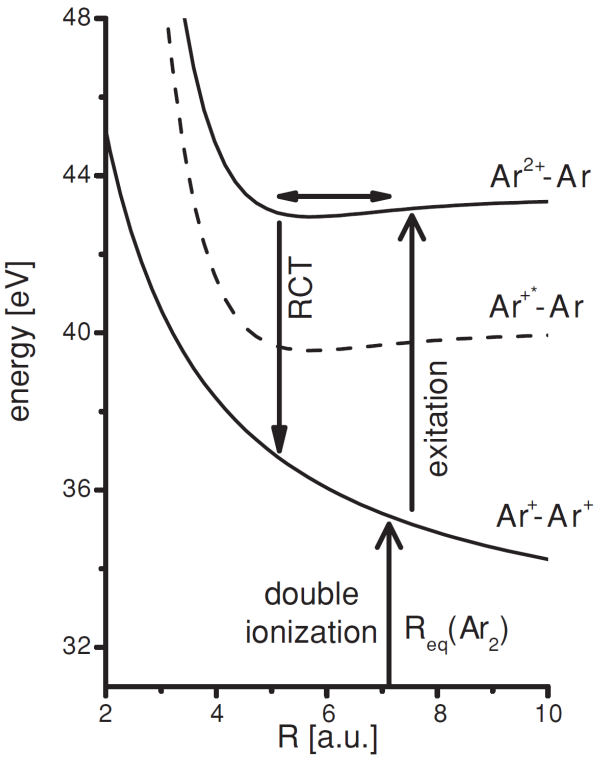

Figure 8.5: Adapted from [163], schematic potential energy curves of $Ar_2{}^{2+}$ and $Ar_2{}^{+}$ showing double ionization with a single 36 eV photon and then excitation by strong field IR. The presence of the IR should affect the localization of the ionization. RCT indicates a radiative charge transfer that becomes more efficient at small internuclear distances.

A 36 eV XUV photon is an ideal tool to access the double ionization of Ar dimers and then

the following Coulomb explosion. It is above the double ionization potential of the argon dimer (35.3 eV) but below the double ionization of atomic argon (43.4 eV). The experiment must be set up in such a way that focuses on dynamics from the dimer while filtering out counts due to background atomic argon. As discussed in Chapter 7, Coulomb explosion provides an excellent way to filter through ion-ion coincidences. Additionally, Coulomb explosion gives information through the KER being inversely proportional to the internuclear spacing to a good approximation. True ion-ion coincidences exclude any influence from atomic argon ionization.

Cederbaum et al. predicted the decay of excited atoms and molecules through a process they called interatomic Coulombic decay (ICD) [164]. The process involves an excited ion with a close neighbour; this was originally applied to molecular clusters but dimers provide a simpler system. The excited ion can relax by transferring its excitation energy to this neighbour, causing that neighbour to emit a lower energy electron. Similar to an Auger decay process, ICD typically occurs on the order of femtoseconds which is much faster than radiative decay processes [165, 166]. ICD differs from Auger decay because the energy transfer must involve a neighboring atom or molecule.

Because of the weak bonding and high internuclear spacing in a dimer, the excitation can be site specific and separated from the nuclear dynamics. This causes an expectation to find a Coulomb explosion KER after double ionization that corresponds to the equilibrium internuclear separation of a neutral Ar_2 dimer. Previous work has found that in addition to this channel there are Ar^+ ions with a higher kinetic energy release [163]. In order to explain this increase in energy the dimer must move towards a much smaller internuclear spacing. The process is proposed where the dimer is initially doubly ionized at a single site (Ar^{2+}-Ar) or put into a one-site singly charged excited state (Ar^{+*}-Ar), which then may decay by ICD [164, 165, 167].

Figure 8.6 shows the time-of-flight spectrum for the supersonic gas jet seeded with argon and pumped by 36 eV XUV photons with IR temporally overlapped. This provides an indication of some of the experimental difficulties as the concentration of the dimer compared to atomic argon in the jet makes it difficult to achieve good signal-to-noise. Even with a clear source and dissociation channel photoion-photoion coincidence experiments require long integration times [14, 68]. In this

experiment, the rarity of Ar_2 causes a decrease in the signal by additional orders of magnitude compared to similar previous Coulomb explosion experiments [14, 168].

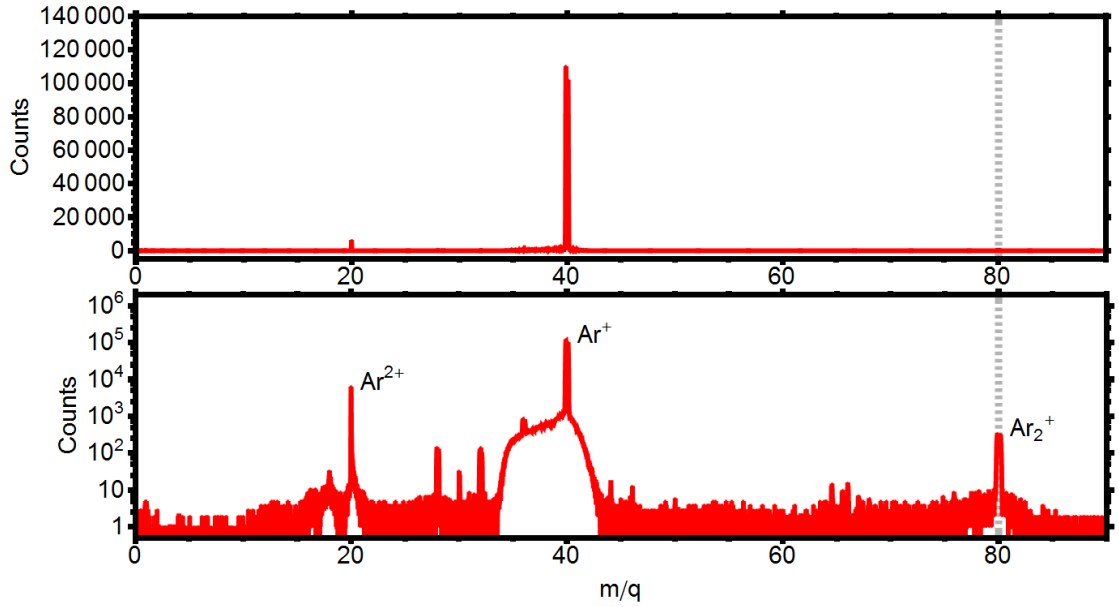

Figure 8.6: Time-of-flight spectrum for argon in the supersonic gas jet probed with 36 eV XUV photons and IR. The signal will be dominated by Ar^+ as well as include a clear indicator of the Ar^{2+} ion. Visible on a semi-log plot is the $Ar_2{}^+$. The small concentration of Ar_2 in the jet causes an experimental challenge. Also visible in the plot are peaks due to a small concentration of H_2O, N_2, and O_2 present due to a small amount of atmosphere present from the input to the gas jet.

Figure 8.7 shows a photoion-photoion coincidence plot for argon dimer counts. Because Ar is much more prevalent than Ar_2 there is a high frequency of false coincidences. There will be many events with a Ar^+ count arriving at the detector first and an second Ar^+ count arriving later due to multiple ionization events in different parts of the gas jet or ionization in the background gas. The double ionization of an argon dimer will result in two positively charged nuclei in close proximity. The Coulomb force on the two ions will cause them to have large repulsive velocities. This Coulomb explosion has a definite center of mass and the particles will show a conservation of momentum. Because of this true coincidence counts have a time-of-flight relationship where if one ion has an initial momentum in the $+z$ direction then the other ion will have momentum in the

$-z$ direction. Center of mass and conversation of momentum provide two features that allow for filtering on coincidence counts.

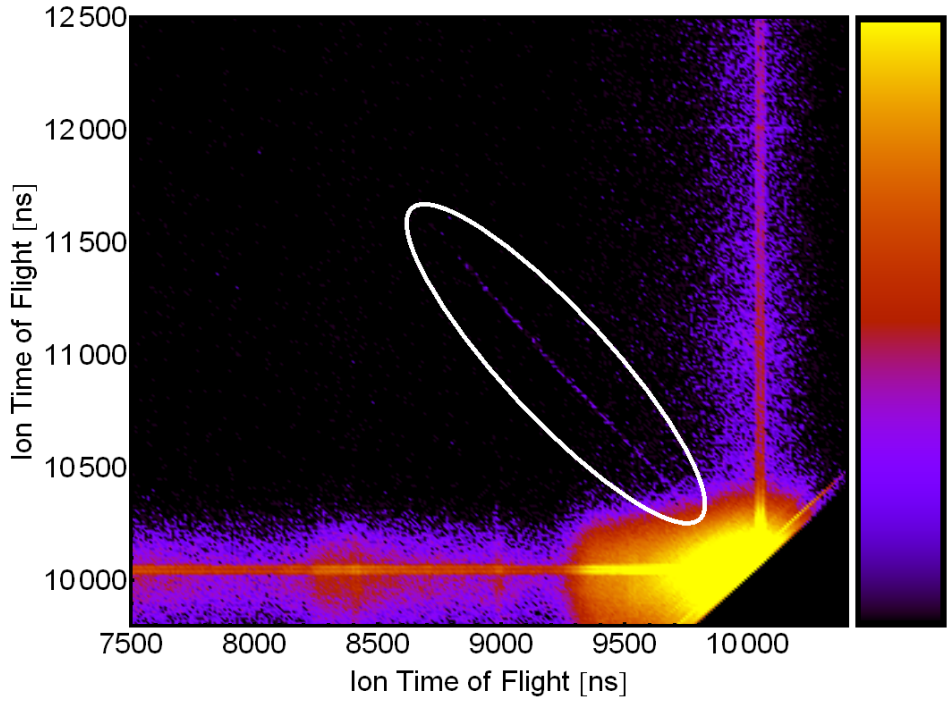

Figure 8.7: Coincidence counts are highlighted within the white oval. Conservation of momentum between each Ar^+ ion from the same original dimer allows for filtering. Plot density shown on a logarithmic scale.

Figure 8.8 shows the KER for the photoion-photoion coincidence channel shown in Figure 8.7. There is a clear KER peak at 3.8 eV that is consistent with previous results [163, 169]. This KER peak shows enhancement when IR is overlapped with the XUV and this enhancement continues for positive delays. Ar dimer has an equilibrium internuclear distance of approximately 7.13 Å [170]. The KER calculated for this distance is 3.82 eV and matches the experimental results exactly [163]. This 3.8 eV Coulomb explosion channel comes from creating single ionization on both argon nuclei on the same dimer.

Figure 8.9 is the KER at 50 fs and clearly shows the peaks at 3.8 eV and around 5 eV, labeled (a) and (b), respectively. A direct two-site double ionization of Ar_2 is unable to explain this higher

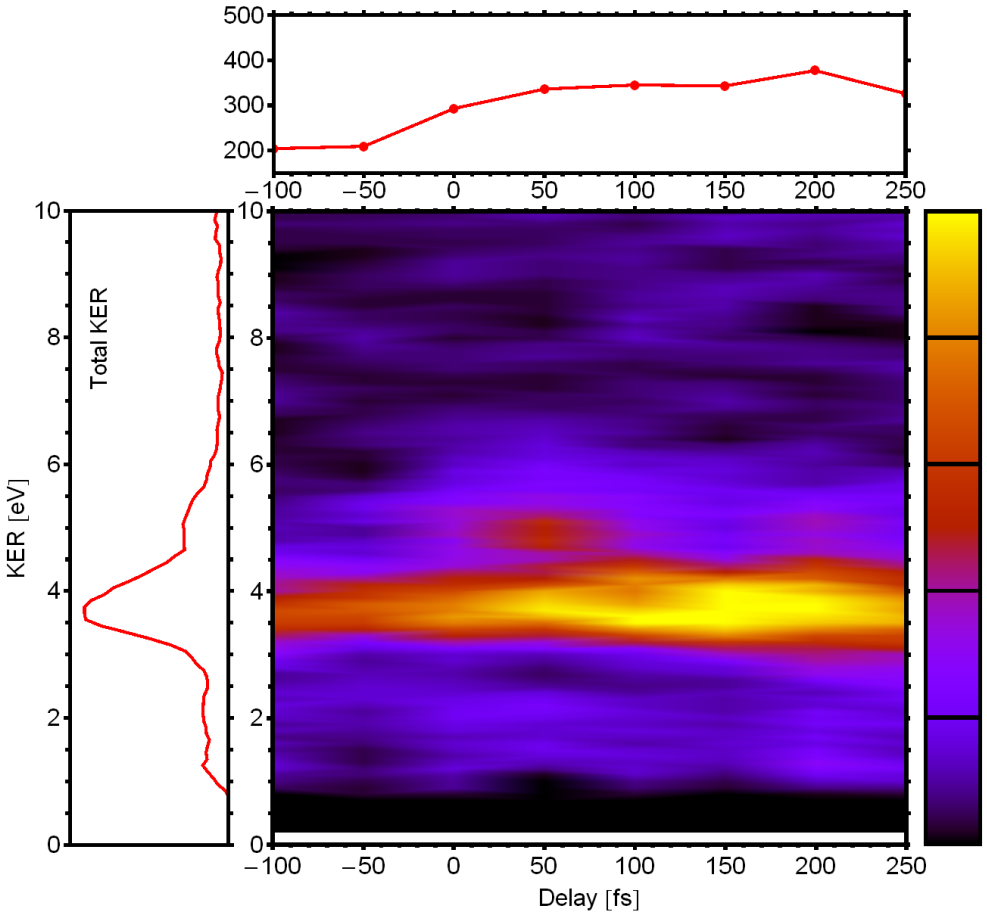

Figure 8.8: Time resolved kinetic energy release of $Ar^+ + Ar^+$ coincidence channel from $Ar_2{}^{2+}$. KER of ∼4 eV is consistent with previous results [163,169]. The left panel shows total KER counts integrated over the scan and the upper panels shows total counts versus delay.

KER peak (b). It requires an internuclear distance smaller than the equilibrium separation. The ionization of each atom in the dimer will result in a Coulomb explosion at the equilibrium distance. If a single atom of the dimer is doubly ionized there are two possible mechanisms that will allow for Coulomb explosion [163]. One mechanism is through a virtual photon which will happen at the equilibrium internuclear spacing and will appear at the 3.8 eV peak. The higher KER peak can be explained by a single site double ionization channel. A 36 eV photon with the IR is enough to put a single argon atom about its double ionization threshold (43.4 eV).This radiative mechanism has a considerable probability to happen even at large internuclear separation. Its rate follows an

inverse power law as a function of the internuclear separation R [171]. The dimer decreases the internuclear spacing in order to relax and allow for ICD.

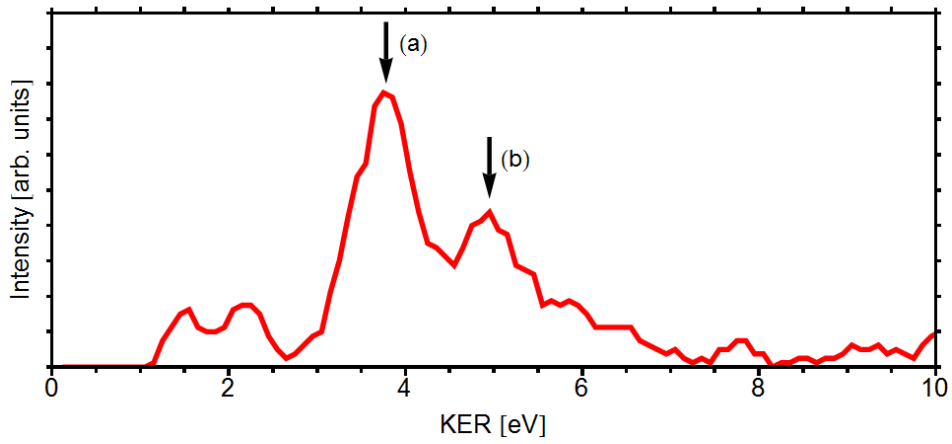

Figure 8.9: Kinetic energy release of $Ar^+ + Ar^+$ coincidence channel at 50 fs. The KER peaks at 3.8 eV, labeled peak (a), and 5 eV, labeld peak (b), are consistent with previous results [163, 169]. While

8.3 Laser-Induced Ultrafast dynamics of Ozone Double Photoionization

Ozone is of tremendous importance in the Earth's upper atmosphere and its dynamics are significant in atmospheric modeling. Being very absorptive in parts of ultraviolet spectrum a relatively small amount is responsible the protection against DNA damage from solar radiation [172,173]. Parts of the dissociation dynamics and possible reformation of ozone are not well known and the improved understanding has many implications related to climate change [174].

By irradiating ozone molecules with few-femtosecond XUV pulses and probing the fragmentation pathways, we find that the excess energy is rapidly and efficiently transferred into internal excitation of the triatomic molecule similar to the discussion in Chapter 7. Using a high energy photon to access the double cation of ozone, we probe the excited state using a strong field IR pulse. Photon energies at 43 eV put ozone well about its double ionization threshold (∼34 eV). Figure 8.10 shows a schematic of exciting ozone to a doubly ionized state and the expected KER.

Figure 8.11 shows the ion time-of-flight spectrum for an ozone sample. Part of the experimen-

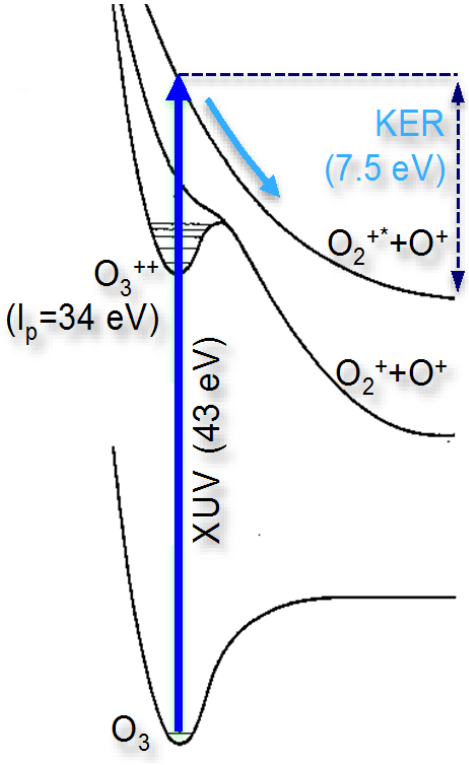

Figure 8.10: Schematic of exciting ozone to a doubly excited state with a single 43 eV photon and probing with IR. Figure adapted from [175].

tal difficulty is producing a clean ozone source with enough pressure to seed a jet in COLTRIMS. Once created, ozone will naturally degrade, with a half life on the order of hours, and the process is catalyzed with interaction with metals such as copper. Creating a pure sample of ozone is important to distinguish the presence of O_2 from the dissociation process compared to that from background O_2 due to the atmospheric contamination as well as natural degradation. Some background N_2 and O_2 is visible in the figure.

The preparation process for ozone make it better suited for the effusive gas jet. Because ozone naturally degrades creating a stable sample with the greatest concentration of O_3 to O_2 required improvements with the preparation and deliver to the gas jet. Once generated, ozone on the porous surface in a silica gel "trap". Figure 8.12 shows the ozone trap when fully charged. A high concentration of color is indicated by the blue color (where ozone is less absorptive). Dry ice

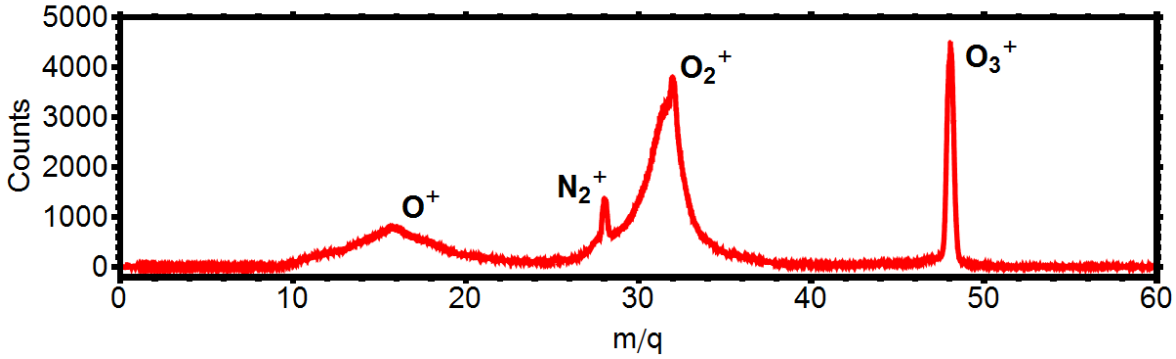

Figure 8.11: Time-of-flight spectrum for a typical data set with ozone sent through the effusive jet. The relative size of the $O_3{}^+$ peak shows it to be a clean sample but the distribution of the O^+ and O^{2+} peaks indicate they originate from dissociation pathways.

was used to control the vapor pressure as well as prevent possible spontaneous combustion. Even with a carrier gas used to seed the supersonic jet, the necessary decay time before the jet would result in a significant level of degeneration.

We found it necessary to evacuate the device to 10 mtorr or lower to remove an appreciable background signal, although the data still contain a significant amount of background caused by residual atmosphere in the device. Because of the background, compared to pure targets that are easier to prepare, relying on photoelectron is challenging without a coincidence photoion to indicate the photoelectron's source.

Figure 8.13 shows the advantage COLTRIMS presents in being able to filter O_3 from background signals. Even with an ideal ozone source there will still be a measurable concentration of molecular oxygen (O_2) present in the gas jet. Using coincidence techniques we can distinguish O^+ fragments that originate from O_3 rather than O_2. Using a 43 eV photon as a probe causing the molecule to reach a double ionizing state it will result in Coulomb explosion and force the molecule to a clear $O_2{}^+ + O^+$ signal. Additionally, this photon energy excites an auto-ionizing state in O_2 resulting in a $O^+ + O^+$ coincidence channel [14]. Because the information of the molecular oxygen Coulomb explosion is taken simultaneously and well known it is an excellent calibration for better understanding the ozone Coulomb explosion.

Figure 8.12: Photograph of the ozone trap. Silica gel provides a porous surface and provides a means to trap generated ozone. The dark blue color indicates a high concentration. The trap is stored with dry ice to produce a lower vapor pressure as well as to prevent spontaneous combustion.

By comparing the O_3^+ and O_2^+ ion fragmentation yields and their kinetic energies as a function of time delay between the XUV pump and IR probe, we find that the triatomic ozone molecule shows an ability to absorb any excess energy internally rather than emerging as kinetic energy released by the Coulomb exploding fragments as observed in other triatomic molecules [168]. This internal conversion of energy in a triatomic molecule before explosion is very different from the case of diatomic molecular oxygen [14] which we can record simultaneously with the ozone

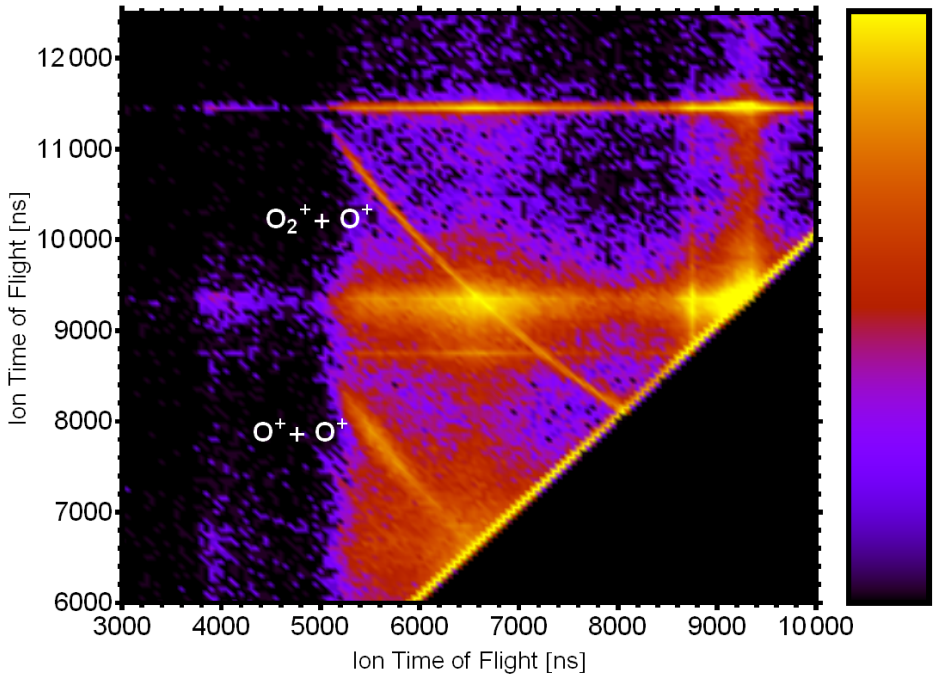

Figure 8.13: Photoion-Photoion coincidence (PIPICO) spectrum showing both $O_2^+ + O^+$ and $O^+ + O^+$ coincidence channels. Both channels can be filtered using conservation of momentum and center of mass filters. Plot density is on a logarithmic scale.

dissociation.

In addition to probing the double ionization we attempted to observe dynamics in the main absorption band in the UV, the Hartley band. On the blue side of this band, at wavelengths shorter than 243 nm, some O_2 dissociation products are created with a large amount of internal energy [174, 176]. Characterization of this process is important to a thorough understanding of these atmospherically relevant conical intersection dynamics. These dynamics would be probed by negative time delays in the above scans, using three photon absorption to pump to the Hartley band, and probing the states with an XUV photon (providing a clear photoelectron signal). These dynamics happen quickly and are difficult to capture with a 30 fs pulse. Additionally, the IR pulse pumps to other dissociating channels. Future improvements using a ultrafast 3ω harmonic of the IR should allow for resolution of these dynamics.

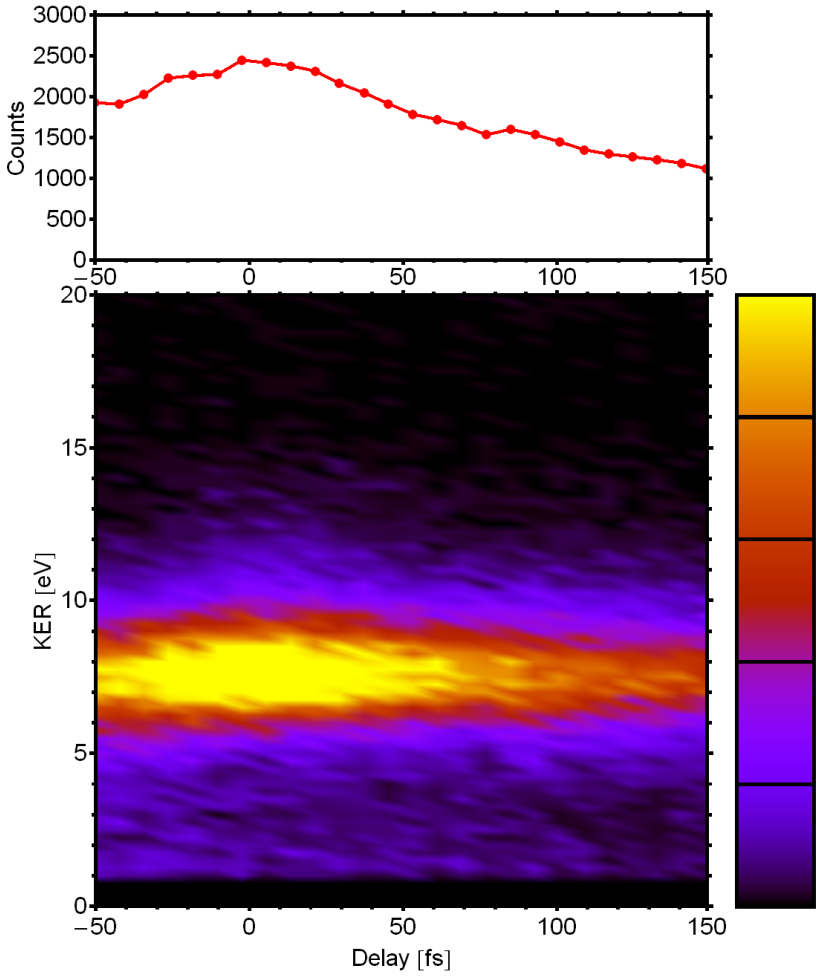

Figure 8.14: Time resolved kinetic energy release of ozone. KER of ∼7.5eV is consistent with our expected results [175].

Chapter 9

Conclusion

In conclusion, this thesis describes the the advancement in understanding of XUV induced atomic and molecular dynamics including the visualization of the dissociation process, the interaction of nuclear and electronic wavepackets and optically controlling ionizing pathways. It demonstrates important progress in the field of atomic and molecular physics, but also calls for a better understanding of known systems and push towards the more complex.

With argon, the understanding of ionizing pathway was better understood including theoretical support. The ability to induce full electro-magnetic transparency in an atom was demonstrated with helium. In diatomic systems the dissociation of bromine helped probe the fundamental time scales of the changing orbital structure in such a process and hydrogen provided a simple system for the interaction of nuclear and electronic dynamics in the non-Born-Oppenheimer regime. With N_2O the ability to optically affect the dissociation process of a triatomic molecule demonstrated a new degree of coherent control.

This work can also be extended to a broad range of systems as demonstrated by the results with more complicated systems. The argon dimer presents a simpler electronic structure, and ozone provides a chance to provide a great deal of understanding to the chemical processes in the upper atmosphere. Ethylene shows many complex dynamics and has the potential for a great deal of future work. While these more complex systems present a challenge different than atomic or diatomic targets, it is only with the ability to resolve attosecond scale electronic and nuclear dynamics that such processes will be well understood. Ultimately it will require further advancement in not only

the high harmonic source and detection but through sample preparation that will allow for new systems.

Bibliography

[1] A. H. Zewail. Femtochemistry: Atomic-scale dynamics of the chemical bond using ultrafast lasers (nobel lecture). Angewandte Chemie International Edition, 39(15):2586–2631, 2000.

[2] T. Popmintchev, M.-C. Chen, D. Popmintchev, P. Arpin, S. Brown, G. Ališauskas, S.and Andriukaitis, T. Balčiunas, O. D. Mcke, A. Pugzlys, A. Baltuška, B. Shim, S. E. Schrauth, A. Gaeta, C. Hernndez-Garca, L. Plaja, A. Becker, A. Jaron-Becker, M. M. Murnane, and H. C. Kapteyn. Bright coherent ultrahigh harmonics in the keV x-ray regime from mid-infrared femtosecond lasers. Science, 336(6086):1287–1291, 2012.

[3] R. Dörner, V. Mergel, O. Jagutzki, L. Spielberger, J. Ullrich, R. Moshammer, and H. Schmidt-Böcking. Cold target recoil ion momentum spectroscopy: a momentum microscope to view atomic collision dynamics. Physics Reports, 330(23):95 – 192, 2000.

[4] R. Moshammer, M. Unverzagt, W. Schmitt, J. Ullrich, and H. Schmidt-Böcking. A 4π recoil-ion electron momentum analyzer: a high-resolution microscope for the investigation of the dynamics of atomic, molecular and nuclear reactions. Nuclear Instruments and Methods in Physics Research Section B: Beam Interactions with Materials and Atoms, 108(4):425 – 445, 1996.

[5] E. Gagnon, A. S. Sandhu, A. Paul, K. Hagen, A. Czasch, T. Jahnke, P. Ranitovic, C. L. Cocke, B. Walker, M. M. Murnane, and H. C. Kapteyn. Time-resolved momentum imaging system for molecular dynamics studies using a tabletop ultrafast extreme-ultraviolet light source. Review of Scientific Instruments, 79(6), 2008.

[6] Tenio Popmintchev. Tunable Ultrafast Coherent Light in the Soft and Hard X-ray Regions of the Spectrum: Phase Matching of Extreme High-Order Harmonic Generation. PhD thesis, Univerisity of Colorado - Boulder, 2009.

[7] A. L'Huillier, K. J. Schafer, and K. C. Kulander. Theoretical aspects of intense field harmonic generation. Journal of Physics B: Atomic, Molecular and Optical Physics, 24(15):3315, 1991.

[8] M. Lewenstein, Ph. Balcou, M. Yu. Ivanov, A. L'Huillier, and P. B. Corkum. Theory of high-harmonic generation by low-frequency laser fields. Phys. Rev. A, 49:2117–2132, Mar 1994.

[9] P. B. Corkum. Plasma perspective on strong field multiphoton ionization. Phys. Rev. Lett., 71:1994–1997, Sep 1993.

[10] A. H. Zewail. Laser femtochemistry. Science, 242(4886):1645–1653, 1988.

[11] A. Stolow, A. E. Bragg, and D. M. Neumark. Femtosecond time-resolved photoelectron spectroscopy. Chemical Reviews, 104(4):1719–1758, 2004. PMID: 15080710.

[12] O. Geßner, A. M. D. Lee, J. P. Shaffer, H. Reisler, S. V. Levchenko, A. I. Krylov, Jonathan G. Underwood, H. Shi, A. L. L. East, D. M. Wardlaw, E. t. H. Chrysostom, C. C. Hayden, and Albert Stolow. Femtosecond multidimensional imaging of a molecular dissociation. Science, 311(5758):219–222, 2006.

[13] M. H. Kim, L. Shen, H. Tao, T. J. Martinez, and A. G. Suits. Conformationally controlled chemistry: Excited-state dynamics dictate ground-state reaction. Science, 315(5818):1561–1565, 2007.

[14] E. Gagnon, P. Ranitovic, X.-M. Tong, C. L. Cocke, M. M. Murnane, H. C. Kapteyn, and A. S. Sandhu. Soft x-ray-driven femtosecond molecular dynamics. Science, 317(5843):1374–1378, 2007.

[15] P. Ranitovic, X.-M. Tong, B. Gramkow, S. De, B. DePaola, K. P. Singh, W. Cao, M. Magrakvelidze, D. Ray, I. Bocharova, H. Mashiko, A. Sandhu, E. Gagnon, M. M. Murnane, H. C. Kapteyn, I. Litvinyuk, and C. L. Cocke. IR-assisted ionization of helium by attosecond extreme ultraviolet radiation. New Journal of Phys., 12:013008, Jan 2010.

[16] P. F. Moulton. Spectroscopic and laser characteristics of ti:al2o3. J. Opt. Soc. Am. B, 3(1):125–133, Jan 1986.

[17] D. E. Spence, P. N. Kean, and W. Sibbett. 60-fsec pulse generation from a self-mode-locked Ti:sapphire laser. Opt. Lett., 16(1):42–44, Jan 1991.

[18] D. Strickland and G. Mourou. Compression of amplified chirped optical pulses. Optics Communications, 56(3):219 – 221, 1985.

[19] S. Backus, J. Peatross, C. P. Huang, M. M. Murnane, and H. C. Kapteyn. Ti:sapphire amplifier producing millijoule-level, 21-fs pulses at 1 kHz. Opt. Lett., 20(19):2000–2002, Oct 1995.

[20] D. M. Gaudiosi, E. Gagnon, A. L. Lytle, J. L. Fiore, E. A. Gibson, S. Kane, J. Squier, M. M. Murnane, H. C. Kapteyn, R. Jimenez, and S. Backus. Multi-kilohertz repetition rate Ti:sapphire amplifier based on down-chirped pulse amplification. Opt. Express, 14(20):9277–9283, Oct 2006.

[21] X. Zhang, E. Schneider, G. Taft, H. C. Kapteyn, M. M. Murnane, and S. Backus. Multi-microjoule, MHz repetition rate Ti:sapphire ultrafast regenerative amplifier system. Opt. Express, 20(7):7015–7021, Mar 2012.

[22] Daisy Raymondson. Tabletop Coherent Diffractive Microscopy with Soft X-Ray Illumination from High Harmonic Generation at 29 nm and 13.5 nm. PhD thesis, Univerisity of Colorado - Boulder, 2010.

[23] Predrag Ranitovic, Craig W. Hogle, Paula Rivire, Alicia Palacios, Xiao-Ming Tong, Nobuyuki Toshima, Alberto Gonzlez-Castrillo, Leigh Martin, Fernando Martn, Margaret M. Murnane, and Henry Kapteyn. Attosecond vacuum uv coherent control of molecular dynamics. Proceedings of the National Academy of Sciences, 111(3):912–917, 2014.

[24] E. Turgut, C. La-o vorakiat, J. M. Shaw, P. Grychtol, H. T. Nembach, D. Rudolf, R. Adam, M. Aeschlimann, C. M. Schneider, T. J. Silva, M. M. Murnane, H. C. Kapteyn, and S. Mathias. Controlling the competition between optically induced ultrafast spin-flip scattering and spin transport in magnetic multilayers. Phys. Rev. Lett., 110:197201, May 2013.

[25] D. D. Hickstein, P. Ranitovic, S. Witte, X.-M. Tong, Y. Huismans, P. Arpin, X. Zhou, K. E. Keister, C. W. Hogle, B. Zhang, C. Ding, P. Johnsson, N. Toshima, M. J. J. Vrakking, M. M. Murnane, and H. C. Kapteyn. Direct visualization of laser-driven electron multiple scattering and tunneling distance in strong-field ionization. Phys. Rev. Lett., 109:073004, Aug 2012.

[26] Q. Li, K. Hoogeboom-Pot, D. Nardi, M. M. Murnane, H. C. Kapteyn, M. E. Siemens, E. H. Anderson, O. Hellwig, E. Dobisz, B. Gurney, R. Yang, and K. A. Nelson. Generation and control of ultrashort-wavelength two-dimensional surface acoustic waves at nanoscale interfaces. Phys. Rev. B, 85:195431, May 2012.

[27] S. Backus, C. G. Durfee, M. M. Murnane, and H. C. Kapteyn. High power ultrafast lasers. Review of Scientific Instruments, 69(3):1207–1223, 1998.

[28] D. M. Gaudiosi, A. L. Lytle, P. Kohl, M. M. Murnane, H. C. Kapteyn, and S. Backus. 11-W average power Ti:sapphire amplifier system using down chirped pulse amplification. Opt. Lett., 29(22):2665–2667, Nov 2004.

[29] I. Walmsley, L. Waxer, and C. Dorrer. The role of dispersion in ultrafast optics. Review of Scientific Instruments, 72(1):1–29, 2001.

[30] A. L. Lytle, X. Zhang, R. L. Sandberg, O. Cohen, H. C. Kapteyn, and M. M. Murnane. Quasi-phase matching and characterization of high-order harmonic generation in hollow waveguides using counterpropagating light. Opt. Express, 16(9):6544–6566, Apr 2008.

[31] T. Popmintchev, M.-C. Chen, P. Arpin, M. M. Murnane, and H. C. Kapteyn. The attosecond nonlinear optics of bright coherent X-ray generation. Nat. Photon., 4:822–832, Dec 2010.

[32] M. Drescher, M. Hentschel, R. Kienberger, M. Uiberacker, V. Yakovlev, A. Scrinzi, Th. Westerwalbesloh, U. Kleineberg, U. Heinzmann, and F. Krausz. Time-resolved atomic inner-shell spectroscopy. Nature, 419, Oct 2002.

[33] R. López-Martens, K. Varjú, P. Johnsson, J. Mauritsson, Y. Mairesse, P. Salières, M. B. Gaarde, K. J. Schafer, A. Persson, S. Svanberg, C. Wahlström, and A. L'Huillier. Amplitude and phase control of attosecond light pulses. Phys. Rev. Lett., 94:033001, Jan 2005.

[34] L. H. Haber, B. Doughty, and S. R. Leone. Continuum phase shifts and partial cross sections for photoionization from excited states of atomic helium measured by high-order harmonic optical pump-probe velocity map imaging. Phys. Rev. A, 79:031401, Mar 2009.

[35] L. V. Keldysh. Ionization in the field of a strong electromagnetic wave. Soviet Physics JETP, 20:1307–1314, May 1965.

[36] Luis Miaja Avila. Laser-Assisted Dynamics on Metallic Surfaces using Ultrafast X-Rays. PhD thesis, Univerisity of Colorado - Boulder, 2009.

[37] M. V. Ammosov, N. B. Delone, and V. P. Krainov. Tunnel ionization of complex atoms and of atomic ions in an alternating electromagnetic field. Soviet Physics - JETP, 64(6):1191–1194, 1986.

[38] J. L. Krause, K. J. Schafer, and K. C. Kulander. High-order harmonic generation from atoms and ions in the high intensity regime. Phys. Rev. Lett., 68:3535–3538, Jun 1992.

[39] Ph. Balcou and A. L'Huillier. Phase-matching effects in strong-field harmonic generation. Phys. Rev. A, 47:1447–1459, Feb 1993.

[40] A. Rundquist, C. G. Durfee, Z. Chang, C. Herne, S. Backus, M. M. Murnane, and H. C. Kapteyn. Phase-matched generation of coherent soft X-rays. Science, 280(5368):1412–1415, 1998.

[41] C. G. Durfee, A. R. Rundquist, S. Backus, C. Herne, M. M. Murnane, and H. C. Kapteyn. Phase matching of high-order harmonics in hollow waveguides. Phys. Rev. Lett., 83:2187–2190, Sep 1999.

[42] Etienne Gagnon. Femtosecond molecular dynamics driven by extreme ultra violet radiation. PhD thesis, Univerisity of Colorado - Boulder, 2008.

[43] P. Ranitovic, X. M. Tong, C. W. Hogle, X. Zhou, Y. Liu, N. Toshima, M. M. Murnane, and H. C. Kapteyn. Laser-enabled auger decay in rare-gas atoms. Phys. Rev. Lett., 106:053002, Jan 2011.

[44] X. M. Tong, P. Ranitovic, C. W. Hogle, M. M. Murnane, H. C. Kapteyn, and N. Toshima. Theory and experiment on laser-enabled inner-valence auger decay of rare-gas atoms. Phys. Rev. A, 84:013405, Jul 2011.

[45] J. M. Schins, P. Breger, P. Agostini, R. C. Constantinescu, H. G. Muller, G. Grillon, A. Antonetti, and A. Mysyrowicz. Observation of laser-assisted auger decay in argon. Phys. Rev. Lett., 73:2180–2183, Oct 1994.

[46] L. Miaja-Avila, C. Lei, M. Aeschlimann, J. L. Gland, M. M. Murnane, H. C. Kapteyn, and G. Saathoff. Laser-assisted photoelectric effect from surfaces. Phys. Rev. Lett., 97:113604, Sep 2006.

[47] L. Miaja-Avila, G. Saathoff, S. Mathias, J. Yin, C. La-o vorakiat, M. Bauer, M. Aeschlimann, M. M. Murnane, and H. C. Kapteyn. Direct measurement of core-level relaxation dynamics on a surface-adsorbate system. Phys. Rev. Lett., 101:046101, Jul 2008.

[48] Th. Mercouris, Y. Komninos, and C. A. Nicolaides. Time-resolved hyperfast processes of strongly correlated electrons during the coherent excitation and decay of multiply excited and inner-hole excited states. Phys. Rev. A, 76:033417, Sep 2007.

[49] C.-H. Zhang and U. Thumm. Laser-assisted photoemission from adsorbate-covered metal surfaces: Time-resolved core-hole relaxation dynamics from sideband profiles. Phys. Rev. A, 80:032902, Sep 2009.

[50] C. Buth and K. J. Schafer. Theory of Auger decay by laser-dressed atoms. Phys. Rev. A, 80:033410, Sep 2009.

[51] Y.-C. Chiang, P. V. Demekhin, A. I. Kuleff, S. Scheit, and L. S. Cederbaum. Linewidth and lifetime of atomic levels and the time evolution of spectra and coincidence spectra. Phys. Rev. A, 81:032511, Mar 2010.

[52] T. Shimizu, T. Sekikawa, T. Kanai, S. Watanabe, and M. Itoh. Time-resolved auger decay in CsBr using high harmonics. Phys. Rev. Lett., 91:017401, Jul 2003.

[53] X. M. Tong and N. Toshima. Controlling atomic structures and photoabsorption processes by an infrared laser. Phys. Rev. A, 81:063403, Jun 2010.

[54] J. A. R. Samson. Proportionality of electron-impact ionization to double photoionization. Phys. Rev. Lett., 65:2861–2864, Dec 1990.

[55] X. M. Tong, K. Hino, and N. Toshima. Phase-dependent atomic ionization in few-cycle intense laser fields. Phys. Rev. A, 74:031405, Sep 2006.

[56] X.-M. Tong and S.-I. Chu. Theoretical study of multiple high-order harmonic generation by intense ultrashort pulsed laser fields: A new generalized pseudospectral time-dependent method. Chemical Physics, 217(23):119 – 130, 1997. Dynamics of Driven Quantum Systems.

[57] X.-M. Tong and N. Toshima. Infrared-laser-assisted photoionization of helium by coherent extreme ultraviolet light. Phys. Rev. A, 81:043429, Apr 2010.

[58] X.-M. Tong and S.-I. Chu. Density-functional theory with optimized effective potential and self-interaction correction for ground states and autoionizing resonances. Phys. Rev. A, 55:3406–3416, May 1997.

[59] R. P. Madden, D. L. Ederer, and K. Codling. Resonances in the photo-ionization continuum of Ar (20-150 eV). Phys. Rev., 177:136–151, Jan 1969.

[60] K.-H. Schartner, B. Möbus, P. Lenz, H. Schmoranzer, and M. Wildberger. Observation of resonances in the Ar 3s photoionization cross section. Phys. Rev. Lett., 61:2744–2747, Dec 1988.

[61] X. M. Tong and C. D. Lin. Empirical formula for static field ionization rates of atoms and molecules by lasers in the barrier-suppression regime. Journal of Physics B: Atomic, Molecular and Optical Physics, 38(15):2593, 2005.

[62] R.D. Cowan. The Theory of Atomic Structure and Spectra. Los Alamos series in basic and applied sciences. University of California Press, 1981.

[63] P. Ranitovic, X. M. Tong, C. W. Hogle, X. Zhou, Y. Liu, N. Toshima, M. M. Murnane, and H. C. Kapteyn. Controlling the XUV transparency of helium using two-pathway quantum interference. Phys. Rev. Lett., 106:193008, May 2011.

[64] R. Haight. Electron dynamics at surfaces. Surface Science Reports, 21(8):275 – 325, 1995.

[65] T. E. Glover, R. W. Schoenlein, A. H. Chin, and C. V. Shank. Observation of laser assisted photoelectric effect and femtosecond high order harmonic radiation. Phys. Rev. Lett., 76:2468–2471, Apr 1996.

[66] C. La-O-Vorakiat, M. Siemens, M. M. Murnane, H. C. Kapteyn, S. Mathias, M. Aeschlimann, P. Grychtol, R. Adam, C. M. Schneider, J. M. Shaw, H. Nembach, and T. J. Silva. Ultrafast demagnetization dynamics at the M edges of magnetic elements observed using a tabletop high-harmonic soft x-ray source. Phys. Rev. Lett., 103:257402, Dec 2009.

[67] S. Baker, J. S. Robinson, C. A. Haworth, H. Teng, R. A. Smith, C. C. Chirilă, M. Lein, J. W. G. Tisch, and J. P. Marangos. Probing proton dynamics in molecules on an attosecond time scale. Science, 312(5772):424–427, 2006.

[68] A. S. Sandhu, E. Gagnon, R. Santra, V. Sharma, W. Li, P. Ho, P. Ranitovic, C. L. Cocke, M. M. Murnane, and H. C. Kapteyn. Observing the creation of electronic feshbach resonances in soft x-ray induced O_2 dissociation. Science, 322(5904):1081–1085, 2008.

[69] K. P. Singh, F. He, P. Ranitovic, W. Cao, S. De, D. Ray, S. Chen, U. Thumm, A. Becker, M. M. Murnane, H. C. Kapteyn, I. V. Litvinyuk, and C. L. Cocke. Control of electron localization in deuterium molecular ions using an attosecond pulse train and a many-cycle infrared pulse. Phys. Rev. Lett., 104:023001, Jan 2010.

[70] U. Eichmann, T. Nubbemeyer, H. Rottke, and W. Sandner. Acceleration of neutral atoms in strong short-pulse laser fields. Nature, 461, Oct 2009.

[71] F. Mauger, C. Chandre, and T. Uzer. Recollisions and correlated double ionization with circularly polarized light. Phys. Rev. Lett., 105:083002, Aug 2010.

[72] P. Johnsson, J. Mauritsson, T. Remetter, A. L'Huillier, and K. J. Schafer. Attosecond control of ionization by wave-packet interference. Phys. Rev. Lett., 99:233001, Dec 2007.

[73] X. M. Tong, P. Ranitovic, C. L. Cocke, and N. Toshima. Mechanisms of infrared-laser-assisted atomic ionization by attosecond pulses. Phys. Rev. A, 81:021404, Feb 2010.

[74] P. Rivière, O. Uhden, U. Saalmann, and J. M. Rost. Strong field dynamics with ultrashort electron wave packet replicas. New Journal of Physics, 11(5):053011, 2009.

[75] P. Brumer and M. Shapiro. Coherence chemistry: controlling chemical reactions [with lasers]. Accounts of Chemical Research, 22(12):407–413, 1989.

[76] S. M. Park, S.-P. Lu, and R. J. Gordon. Coherent laser control of the resonance-enhanced multiphoton ionization of HCl. The Journal of Chemical Physics, 94(12):8622–8624, 1991.

[77] D. Meshulach and Y. Silberberg. Coherent quantum control of two-photon transitions by a femtosecond laser pulse. Nature, 396, Nov 1998.

[78] R. J. Levis, G. M. Menkir, and H. Rabitz. Selective bond dissociation and rearrangement with optimally tailored, strong-field laser pulses. Science, 292(5517):709–713, 2001.

[79] R. Teets, J. Eckstein, and T. W. Hänsch. Coherent two-photon excitation by multiple light pulses. Phys. Rev. Lett., 38:760–764, Apr 1977.

[80] S. E. Harris. Electromagnetically induced transparency. Phys. Today, 50:36–42, Jul 1997.

[81] V. Blanchet, C. Nicole, M.-A. Bouchene, and B. Girard. Temporal coherent control in two-photon transitions: From optical interferences to quantum interferences. Phys. Rev. Lett., 78:2716–2719, Apr 1997.

[82] W. Li, A. A. Jaroń-Becker, C. W. Hogle, V. Sharma, X. Zhou, A. Becker, H. C. Kapteyn, and M. M. Murnane. Visualizing electron rearrangement in space and time during the transition from a molecule to atoms. Proceedings of the National Academy of Sciences, 107(47):20219–20222, 2010.

[83] W. Li, X. Zhou, R. Lock, S. Patchkovskii, A. Stolow, H. C. Kapteyn, and M. M. Murnane. Time-resolved dynamics in N_2O_4 probed using high harmonic generation. Science, 322(5905):1207–1211, 2008.

[84] X. Zhou, R. Lock, W. Li, N. Wagner, M. M. Murnane, and H. C. Kapteyn. Molecular recollision interferometry in high harmonic generation. Phys. Rev. Lett., 100:073902, Feb 2008.

[85] J. Itatani, J. Levesque, D. Zeidler, H. Niikura, H. Pepin, J. C. Kieffer, P. B. Corkum, and D. M. Villeneuve. Tomographic imaging of molecular orbitals. Nature, 432:867–871, Dec 2004.

[86] N. Dudovich, O. Smirnova, J. Levesque, Y. Mairesse, M. Yu. Ivanov, D. M. Villeneuve, and P. B. Corkum. Measuring and controlling the birth of attosecond XUV pulses. Nat. Phys., 2:781–786, Nov 2006.

[87] H. J. Worner, J. B. Bertrand, D. V. Kartashov, P. B. Corkum, and D. M. Villeneuve. Following a chemical reaction using high-harmonic interferometry. Nature, 466:604–607, July 2010.

[88] A. Jaroń-Becker, A. Becker, and F. H. M. Faisal. Dependence of strong-field photoelectron angular distributions on molecular orientation. Journal of Physics B: Atomic, Molecular and Optical Physics, 36(21):L375, 2003.

[89] A. Jaroń-Becker, A. Becker, and F. H. M. Faisal. Ionization of N_2, O_2 and linear carbon clusters in a strong laser pulse. Phys. Rev. A, 69:023410, Feb 2004.

[90] C.D. Lin and X.-M. Tong. Dependence of tunneling ionization and harmonic generation on the structure of molecules by short intense laser pulses. Journal of Photochemistry and Photobiology A: Chemistry, 182(3):213 – 219, 2006. Proceedings of 7th International Symposium on Photoreaction Control and Photofunctional Materials.

[91] D. Pavičić, K. F. Lee, D. M. Rayner, P. B. Corkum, and D. M. Villeneuve. Direct measurement of the angular dependence of ionization for N_2, O_2, and CO_2 in intense laser fields. Phys. Rev. Lett., 98:243001, Jun 2007.

[92] I. Thomann, R. Lock, V. Sharma, E. Gagnon, S. T. Pratt, H. C. Kapteyn, M. M. Murnane, and W. Li. Direct measurement of the angular dependence of the single-photon ionization of aligned N_2 and CO_2. The Journal of Physical Chemistry A, 112(39):9382–9386, 2008. PMID: 18693716.

[93] X. M. Tong, Z. X. Zhao, and C. D. Lin. Theory of molecular tunneling ionization. Phys. Rev. A, 66:033402, Sep 2002.

[94] C. Z. Bisgaard, O. J. Clarkin, G. Wu, A. M. D. Lee, O. Geßner, C. C. Hayden, and A. Stolow. Time-resolved molecular frame dynamics of fixed-in-space CS_2 molecules. Science, 323(5920):1464–1468, 2009.

[95] D. Strasser, L. H. Haber, B. Doughty, and S. R. Leone. Ultrafast predissociation of superexcited nitrogen molecules. Molecular Physics, 106(2-4):275–280, 2008.

[96] Ph. Wernet, M. Odelius, K. Godehusen, J. Gaudin, O. Schwarzkopf, and W. Eberhardt. Real-time evolution of the valence electronic structure in a dissociating molecule. Phys. Rev. Lett., 103:013001, Jun 2009.

[97] J. Muth-Böhm, A. Becker, and F. H. M. Faisal. Suppressed molecular ionization for a class of diatomics in intense femtosecond laser fields. Phys. Rev. Lett., 85:2280–2283, Sep 2000.

[98] M. J. Cooper, E. Wrede, A. J. Orr-Ewing, and M. N. R. Ashfold. Ion imaging studies of the $Br(^2P_j)$ atomic products resulting from Br_2 photolysis in the wavelength range 260-580 nm. J. Chem. Soc., Faraday Trans., 94:2901–2907, 1998.

[99] T. Seideman, M. Yu. Ivanov, and P. B. Corkum. Role of electron localization in intense-field molecular ionization. Phys. Rev. Lett., 75:2819–2822, Oct 1995.

[100] T. Zuo and A. D. Bandrauk. Charge-resonance-enhanced ionization of diatomic molecular ions by intense lasers. Phys. Rev. A, 52:R2511–R2514, Oct 1995.

[101] A. D. Becke and K. E. Edgecombe. A simple measure of electron localization in atomic and molecular systems. The Journal of Chemical Physics, 92(9):5397–5403, 1990.

[102] A. Savin, B. Silvi, and F. Coionna. Topological analysis of the electron localization function applied to delocalized bonds. Canadian Journal of Chemistry, 74(6):1088–1096, 1996.

[103] D. J. Tannor and S. A. Rice. Control of selectivity of chemical reaction via control of wave packet evolution. The Journal of Chemical Physics, 83(10):5013–5018, 1985.

[104] P. Brumer and M. Shapiro. Control of unimolecular reactions using coherent light. Chemical Physics Letters, 126(6):541–546, 1986.

[105] P. Brumer and M. Shapiro. Laser control of molecular processes. Annual Review of Physical Chemistry, 43(1):257–282, 1992. PMID: 18397166.

[106] L. Zhu, V. Kleiman, X. Li, S. P. Lu, K. Trentelman, and R. J. Gordon. Coherent laser control of the product distribution obtained in the photoexcitation of HI. Science, 270(5233):77–80, 1995.

[107] R. J. Glauber. The quantum theory of optical coherence. Phys. Rev., 130:2529–2539, Jun 1963.

[108] Z. Chang, A. Rundquist, H. Wang, M. M. Murnane, and H. C. Kapteyn. Generation of coherent soft X-rays at 2.7 nm using high harmonics. Phys. Rev. Lett., 79:2967–2970, Oct 1997.

[109] T. Brabec and F. Krausz. Intense few-cycle laser fields: Frontiers of nonlinear optics. Rev. Mod. Phys., 72:545–591, Apr 2000.

[110] P. M. Paul, E. S. Toma, P. Breger, G. Mullot, F. Aug, Ph. Balcou, H. G. Muller, and P. Agostini. Observation of a train of attosecond pulses from high harmonic generation. Science, 292(5522):1689–1692, 2001.

[111] S. E. Canton, E. Plésiat, J. D. Bozek, B. S. Rude, P. Decleva, and F. Martín. Direct observation of Youngs double-slit interferences in vibrationally resolved photoionization of diatomic molecules. Proceedings of the National Academy of Sciences, 2011.

[112] F. Martín, J. Fernández, T. Havermeier, L. Foucar, Th. Weber, K. Kreidi, M. Schöffler, L. Schmidt, T. Jahnke, O. Jagutzki, A. Czasch, E. P. Benis, T. Osipov, A. L. Landers, A. Belkacem, M. H. Prior, H. Schmidt-Böcking, C. L. Cocke, and R. Dörner. Single photon-induced symmetry breaking of H_2 dissociation. Science, 315(5812):629–633, 2007.

[113] D. Akoury, K. Kreidi, T. Jahnke, Th. Weber, A. Staudte, M. Schöffler, N. Neumann, J. Titze, L. Ph. H. Schmidt, A. Czasch, O. Jagutzki, R. A. Costa Fraga, R. E. Grisenti, R. Dez Muiño, N. A. Cherepkov, S. K. Semenov, P. Ranitovic, C. L. Cocke, T. Osipov, H. Adaniya, J. C. Thompson, M. H. Prior, A. Belkacem, A. L. Landers, H. Schmidt-Böcking, and R. Dörner. The simplest double slit: Interference and entanglement in double photoionization of H_2. Science, 318(5852):949–952, 2007.

[114] W. Vanroose, F. Martín, T. N. Rescigno, and C. W. McCurdy. Complete photo-induced breakup of the H_2 molecule as a probe of molecular electron correlation. Science, 310(5755):1787–1789, 2005.

[115] F. Kelkensberg, W. Siu, J. F. Pérez-Torres, F. Morales, G. Gademann, A. Rouzée, P. Johnsson, M. Lucchini, F. Calegari, J. L. Sanz-Vicario, F. Martín, and M. J. J. Vrakking. Attosecond control in photoionization of hydrogen molecules. Phys. Rev. Lett., 107:043002, Jul 2011.

[116] Y. Furukawa, Y. Nabekawa, T. Okino, S. Saugout, K. Yamanouchi, and K. Midorikawa. Nonlinear fourier-transform spectroscopy of D_2 using high-order harmonic radiation. Phys. Rev. A, 82:013421, Jul 2010.

[117] F. Kelkensberg, C. Lefebvre, W. Siu, O. Ghafur, T. T. Nguyen-Dang, O. Atabek, A. Keller, V. Serov, P. Johnsson, M. Swoboda, T. Remetter, A. L'Huillier, S. Zherebtsov, G. Sansone, E. Benedetti, F. Ferrari, M. Nisoli, F. Lépine, M. F. Kling, and M. J. J. Vrakking. Molecular dissociative ionization and wave-packet dynamics studied using two-color XUV and IR pump-probe spectroscopy. Phys. Rev. Lett., 103:123005, Sep 2009.

[118] Th. Ergler, A. Rudenko, B. Feuerstein, K. Zrost, C. D. Schröter, R. Moshammer, and J. Ullrich. Spatiotemporal imaging of ultrafast molecular motion: Collapse and revival of the D_2^+ nuclear wave packet. Phys. Rev. Lett., 97:193001, Nov 2006.

[119] Th. Ergler, B. Feuerstein, A. Rudenko, K. Zrost, C. D. Schröter, R. Moshammer, and J. Ullrich. Quantum-phase resolved mapping of ground-state vibrational D_2 wave packets via selective depletion in intense laser pulses. Phys. Rev. Lett., 97:103004, Sep 2006.

[120] G. Sansone, F. Kelkensberg, J. F. Perez-Torres, F. Morales, M. F. Kling, W. Siu, O. Ghafur, P. Johnsson, M. Swoboda, E. Benedetti, F. Ferrari, F. Lepine, J. L. Sanz-Vicario, S. Zherebtsov, I. Znakovskaya, A. LHuillier, M. Yu. Ivanov, M. Nisoli, F. Martin, and M. J. J. Vrakking. Electron localization following attosecond molecular photoionization. Nature, 465:763–766, Jun 2010.

[121] T. Bayer, H. Braun, C. Sarpe, R. Siemering, P. von den Hoff, R. de Vivie-Riedle, T. Baumert, and M. Wollenhaupt. Charge oscillation controlled molecular excitation. Phys. Rev. Lett., 110:123003, Mar 2013.

[122] J. Ullrich, R. Moshammer, R. Dörner, O. Jagutzki, V. Mergel, H. Schmidt-Böcking, and L. Spielberger. Recoil-ion momentum spectroscopy. Journal of Physics B: Atomic, Molecular and Optical Physics, 30(13):2917, 1997.

[123] U. Becker and D. A. Shirley. VUV and Soft X-Ray Photoionization. Interdisciplinary Contributions to Archaeology. Springer, 1996.

[124] M. Uiberacker, Th. Uphues, M. Schultze, A. J. Verhoef, V. Yakovlev, M. F. Kling, J. Rauschenberger, N. M. Kabachnik, H. Schroder, M. Lezius, K. L. Kompa, H.-G. Muller, M. J. J. Vrakking, S. Hendel, U. Kleineberg, U. Heinzmann, M. Drescher, and F. Krausz. Attosecond real-time observation of electron tunnelling in atoms. Nature, 446:627–632, Apr 2007.

[125] W. Cao, S. De, K. P. Singh, S. Chen, M. S. Schöffler, A. S. Alnaser, I. A. Bocharova, G. Laurent, D. Ray, S. Zherebtsov, M. F. Kling, I. Ben-Itzhak, I. V. Litvinyuk, A. Belkacem, T. Osipov, T. Rescigno, and C. L. Cocke. Dynamic modification of the fragmentation of CO^{q+} excited states generated with high-order harmonics. Phys. Rev. A, 82:043410, Oct 2010.

[126] Yoshihiko H. Spectroscopy and dynamics of molecular superexcited states. aspects of primary processes of radiation chemistry. Radiation Physics and Chemistry, 67(34):187 – 198, 2003. 10th Tihany Symposium on Radiation Chemistry.

[127] I. Hjelte, M .N. Piancastelli, R. F. Fink, O. Björneholm, M. Bässler, R. Feifel, A. Giertz, H. Wang, K. Wiesner, A. Ausmees, C. Miron, S.L. Sorensen, and S. Svensson. Evidence for ultra-fast dissociation of molecular water from resonant Auger spectroscopy. Chemical Physics Letters, 334(13):151 – 158, 2001.

[128] J. H. D. Eland. Dynamics of Double Photoionization in Molecules and Atoms, pages 103–151. John Wiley & Sons, Inc., 2009.

[129] S. Scheit, L. S. Cederbaum, and H.-D. Meyer. Time-dependent interplay between electron emission and fragmentation in the interatomic Coulombic decay. The Journal of Chemical Physics, 118(5):2092–2107, 2003.

[130] N. Sisourat, N. V. Kryzhevoi, P. Kolorenc, S. Scheit, T. Jahnke, and L. S. Cederbaum. Ultralong-range energy transfer by interatomic Coulombic decay in an extreme quantum system. Nat. Phys., 6:508–511, Jul 2010.

[131] J.H.D. Eland. Double photoionisation spectra of methane, ammonia and water. Chemical Physics, 323(23):391 – 396, 2006.

[132] C. Daniel, J. Full, L. González, C. Lupulescu, J. Manz, A. Merli, S. Vajda, and L. Wöste. Deciphering the reaction dynamics underlying optimal control laser fields. Science, 299(5606):536–539, 2003.

[133] T. A. Field and J.H.D. Eland. Lifetimes of metastable molecular doubly charged ions. Chemical Physics Letters, 211(45):436 – 442, 1993.

[134] S. Hsieh and J. H. D. Eland. Reaction dynamics of three-body dissociations in triatomic molecules from single-photon double ionization studied by a time- and position-sensitive coincidence method. Journal of Physics B: Atomic, Molecular and Optical Physics, 30(20):4515, 1997.

[135] S. D. Price, J. H. D. Eland, P. G. Fournier, J. Fournier, and P. Millie. Electronic states and decay mechanisms of the N_2O^{2+} dication. The Journal of Chemical Physics, 88(3):1511–1515, 1988.

[136] N. Levasseur and P. Millié. Potential energy surfaces of the low-lying states of N_2O^{++} and photodissociation mechanisms. The Journal of Chemical Physics, 92(5):2974–2983, 1990.

[137] D.M.P. Holland, M.A. Macdonald, and M.A. Hayes. A photoelectron study of the inner valence molecular orbitals of N_2O. Chemical Physics, 142(2):291 – 300, 1990.

[138] W. Domcke, L.S. Cederbaum, J. Schirmer, W. von Niessen, C.E. Brion, and K.H. Tan. Experimental and theoretical investigation of the complete valence shell ionization spectra of CO_2 N_2O. Chemical Physics, 40(12):171 – 183, 1979.

[139] M. Ehara, S. Yasuda, and H. Nakatsuji. Fine theoretical spectroscopy using sac-ci general r method: Outer- and inner-valence ionization spectra of N_2O and HN_3. Zeitschrift fr Physikalische Chemie/International journal of research in physical chemistry and chemical physics, 217:91–184, Sep 2009.

[140] T. Odagiri, K. Funatsu, T. Tanabe, I. H. Suzuki, M. Kitajima, and N. Kouchi. The generation of a pair of photons from superexcited states of nitric oxide around the double ionization potential. Journal of Physics B: Atomic, Molecular and Optical Physics, 42(22):225101, 2009.

[141] A.P. Hitchcock, C.E. Brion, and M.J. van der Wiel. Absolute oscillator strengths for valence-shell ionic photofragmentations of N_2O and CO_2 (875 eV). Chemical Physics, 45(3):461 – 478, 1980.

[142] S. Taylor, J. H. D. Eland, and M. Hochlaf. Fluorescence and metastability of N_2O^{2+}: Theory and experiment. The Journal of Chemical Physics, 124(20), 2006.

[143] P. Erman, A. Karawajczyk, U. Köble, E. Rachlew, K. Yoshiki Franzén, and L. Veseth. Ultrashort-lived non-rydberg doubly excited resonances observed in molecular photoionization. Phys. Rev. Lett., 76:4136–4139, May 1996.

[144] H. Wang, M. Chini, S. Chen, C.-H. Zhang, F. He, Y. Cheng, Y. Wu, U. Thumm, and Z. Chang. Attosecond time-resolved autoionization of argon. Phys. Rev. Lett., 105:143002, Oct 2010.

[145] C. Miron, M. Simon, N. Leclercq, D. L. Hansen, and P. Morin. Site-selective photochemistry of core excited molecules: Role of the internal energy. Phys. Rev. Lett., 81:4104–4107, Nov 1998.

[146] E. Kinmond, J.H.D. Eland, and L. Karlsson. Dissociation of N_2O^+ ions from the valence states reached by one-photon photoionisation. International Journal of Mass Spectrometry, 185187:437–447, 1999.

[147] T. Masuoka. Observation of anisotropic angular distribution of ionic fragments in the dissociation of CO^{2+}. Phys. Rev. A, 50:2298–2303, Sep 1994.

[148] H. Sann, T. Jahnke, T. Havermeier, K. Kreidi, C. Stuck, M. Meckel, M. S. Schöffler, N. Neumann, R. Wallauer, S. Voss, A. Czasch, O. Jagutzki, Th. Weber, H. Schmidt-Böcking, S. Miyabe, D. J. Haxton, A. E. Orel, T. N. Rescigno, and R. Dörner. Electron diffraction self-imaging of molecular fragmentation in two-step double ionization of water. Phys. Rev. Lett., 106:133001, Mar 2011.

[149] T. YOSHIZAWA and G. WALD. Pre-lumirhodopsin and the bleaching of visual pigments. Nature, 197:1279–1286, Mar 1963.

[150] D. Polli, P. Altoe, O. Weingart, K. M. Spillane, C. Manzoni, D. Brida, G. Tomasello, G. Orlandi, P. Kukura, R. A. Mathies, M. Garavelli, and G. Cerullo. Conical intersection dynamics of the primary photoisomerization event in vision. Nature, 467:440–443, Sep 2010.

[151] M. Garavelli, P. Celani, F. Bernardi, M. A. Robb, and M. Olivucci. The $C_5H_6NH_2^+$ protonated shiff base: An ab initio minimal model for retinal photoisomerization. Journal of the American Chemical Society, 119(29):6891–6901, 1997.

[152] R. González-Luque, M. Garavelli, F. Bernardi, M. Merchán, M. A. Robb, and M. Olivucci. Computational evidence in favor of a two-state, two-mode model of the retinal chromophore photoisomerization. Proceedings of the National Academy of Sciences, 97(17):9379–9384, 2000.

[153] S. Hahn and G. Stock. Quantum-mechanical modeling of the femtosecond isomerization in rhodopsin. The Journal of Physical Chemistry B, 104(6):1146–1149, 2000.

[154] T. K. Allison, H. Tao, W. J. Glover, T. W. Wright, A. M. Stooke, C. Khurmi, J. van Tilborg, Y. Liu, R. W. Falcone, T. J. Martnez, and A. Belkacem. Ultrafast internal conversion in ethylene. ii. mechanisms and pathways for quenching and hydrogen elimination. The Journal of Chemical Physics, 136(12):–, 2012.

[155] A. J. Merer and R. S. Mulliken. Ultraviolet spectra and excited states of ethylene and its alkyl derivatives. Chemical Reviews, 69(5):639–656, 1969.

[156] P. A. Snyder, S. Atanasova, and R. W. C. Hansen. Ethylene. experimental evidence for new assignments of electronic transitions in the $\pi \rightarrow \pi^*$ energy region. absorption and magnetic circular dichroism measurements with synchrotron radiation. The Journal of Physical Chemistry A, 108(19):4194–4201, 2004.

[157] K. Kosma, S. A. Trushin, W. Fuss, and W. E. Schmid. Ultrafast dynamics and coherent oscillations in ethylene and ethylene-d_4 excited at 162 nm. The Journal of Physical Chemistry A, 112(33):7514–7529, 2008. PMID: 18661929.

[158] C. Sannen, G. Raşeev, C. Galloy, G. Fauville, and J. C. Lorquet. Unimolecular decay paths of electronically excited species. ii. the $C_2H_4^+$ ion. The Journal of Chemical Physics, 74(4):2402–2411, 1981.

[159] J. van Tilborg, T. K. Allison, T. W. Wright, M. P. Hertlein, R. W. Falcone, Y. Liu, H. Merdji, and A. Belkacem. Femtosecond isomerization dynamics in the ethylene cation measured in an

EUV-pump NIR-probe configuration. Journal of Physics B: Atomic, Molecular and Optical Physics, 42(8):081002, 2009.

[160] J. J. Lin, D. W. Hwang, Y. T. Lee, and X. Yang. Site and isotope effects on the molecular hydrogen elimination from ethylene at 157 nm excitation. The Journal of Chemical Physics, 109(8):2979–2982, 1998.

[161] J. J. Lin, C. C. Wang, Y. T. Lee, and X. Yang. Site-specific dissociation dynamics of ethylene at 157 nm: Atomic and molecular hydrogen elimination. The Journal of Chemical Physics, 113(21):9668–9677, 2000.

[162] M. C. Beard, G. M. Turner, and C. A. Schmuttenmaer. Measuring intramolecular charge transfer via coherent generation of thz radiation. The Journal of Physical Chemistry A, 106(6):878–883, 2002.

[163] B. Manschwetus, H. Rottke, G. Steinmeyer, L. Foucar, A. Czasch, H. Schmidt-Böcking, and W. Sandner. Mechanisms underlying strong-field double ionization of argon dimers. Phys. Rev. A, 82:013413, Jul 2010.

[164] L. S. Cederbaum, J. Zobeley, and F. Tarantelli. Giant intermolecular decay and fragmentation of clusters. Phys. Rev. Lett., 79:4778–4781, Dec 1997.

[165] T. Jahnke, A. Czasch, M. S. Schöffler, S. Schössler, A. Knapp, M. Käsz, J. Titze, C. Wimmer, K. Kreidi, R. E. Grisenti, A. Staudte, O. Jagutzki, U. Hergenhahn, H. Schmidt-Böcking, and R. Dörner. Experimental observation of interatomic coulombic decay in neon dimers. Phys. Rev. Lett., 93:163401, Oct 2004.

[166] Y. Morishita, X.-J. Liu, N. Saito, T. Lischke, M. Kato, G. Prümper, M. Oura, H. Yamaoka, Y. Tamenori, I. H. Suzuki, and K. Ueda. Experimental evidence of interatomic coulombic decay from the auger final states in argon dimers. Phys. Rev. Lett., 96:243402, Jun 2006.

[167] P. Lablanquie, T. Aoto, Y. Hikosaka, Y. Morioka, F. Penent, and K. Ito. Appearance of interatomic coulombic decay in Ar, Kr, and Xe homonuclear dimers. The Journal of Chemical Physics, 127(15), 2007.

[168] X. Zhou, P. Ranitovic, C. W. Hogle, J. H. D. Eland, H. C. Kapteyn, and M. M. Murnane. Probing and controlling non-born-oppenheimer dynamics in highly excited molecular ions. Nat. Phys., 8:232–237, Mar 2012.

[169] A. De Fanis, M. Oura, N. Saito, M. Machida, M. Nagoshi, A. Knapp, J. Nickles, A. Czasch, R. Dörner, Y. Tamenori, H. Chiba, M. Takahashi, J. H. D. Eland, and K. Ueda. Photoelectronphotoionphotoion coincidence in Ar dimers. Journal of Physics B: Atomic, Molecular and Optical Physics, 37(12):L235, 2004.

[170] P. Slavíček, R. Kalus, P. Paška, I. Odvárková, P. Hobza, and A. Malijevský. State-of-the-art correlated ab initio potential energy curves for heavy rare gas dimers: Ar_2, Kr_2, and Xe_2. The Journal of Chemical Physics, 119(4):2102–2119, 2003.

[171] V. Averbukh, I. B. Müller, and L. S. Cederbaum. Mechanism of interatomic coulombic decay in clusters. Phys. Rev. Lett., 93:263002, Dec 2004.

[172] Q.-B. Lu. Correlation between cosmic rays and ozone depletion. Phys. Rev. Lett., 102:118501, Mar 2009.

[173] A. T. J. de Laat and M. van Weele. The 2010 antarctic ozone hole: Observed reduction in ozone destruction by minor sudden stratospheric warmings. Sci. Rep., 1, July 2011.

[174] R. L. Miller, A. G. Suits, P. L. Houston, R. Toumi, J. A. Mack, and A. M. Wodtke. The "ozone deficit" problem: O_2(x, v 26) + O(^{3}p) from 226-nm ozone photodissociation. Science, 265(5180):1831–1838, 1994.

[175] K. A. Newson and S. D. Price. The formation and dissociation of the ozone dication. International Journal of Mass Spectrometry and Ion Processes, 153(23):151 – 159, 1996.

[176] R. Schinke, G. C. McBane, L. Shen, P. C. Singh, and A. G. Suits. Production of O_2 herzberg states in the deep UV photodissociation of ozone. The Journal of Chemical Physics, 131(1), 2009.